Pre-Charged Collapse-Mode CMUTs
A building block for future ultrasound

Saccher, M.

Important note
To cite this publication, please use the final published version (if applicable).
Please check the document version above.

PRE-CHARGED COLLAPSE-MODE CMUTS

A BUILDING BLOCK FOR FUTURE ULTRASOUND

PRE-CHARGED COLLAPSE-MODE CMUTS

A BUILDING BLOCK FOR FUTURE ULTRASOUND

Dissertation

for the purpose of obtaining the degree of doctor
at Delft University ofTechnology
by the authority of the Rector Magnificus Prof.dr.ir. T.H.J.J. van der Hagen
chair of the Board for Doctorates
to be defended publicly on
Thursday 5 September 2024 at 12:30 o'clock

by

Marta SACCHER

Master of Science in Biomedical Engineering
Delft University of Technology, the Netherlands
born in Trieste, Italy

This dissertation has been approved by the promotors.

Composition of the doctoral committee:

Rector Magnificus	chairperson
Prof. dr. ir. R. Dekker	Delft University of Technology, promotor
Dr. V. Giagka	Delft University of Technology, copromotor

Independent members:

Prof. dr. ir. P. M. Sarro	Delft University of Technology
Prof. dr. P. J. French	Delft University of Technology
Dr. ir. J. G. Bosch	Erasmus MC, The Netherlands
Dr. ir. M. A. P. Pertijs	Delft University of Technology
Dr. ir. S. Vollebregt	Delft University of Technology, reserve member

Other member:

Prof. dr. A. S. Savoia	Roma Tre University, Italy

Keywords:	Capacitive Micromachined Ultrasonic Transducers, pre-charged CMUTs, ultrasound, ultrasonic power transfer, implantable devices, charge trapping, charge retention, simulations, matrix array ultrasound receiver
Printed by:	Ipskamp printing
Cover by:	Marta Saccher with the help of Adobe Generative AI

To my family.

CONTENTS

SUMMARY

Advancements in novel technologies are boosting innovation in healthcare enabling decentralisation and personalised medicines. The convergence of the Pharma, MedTech, and ECS industry has led to the creation of new medical domains among which are bioelectronic medicines and personalised ultrasound. Ultrasound is a key player in both domains. In implantable devices it can be used as a means of neuromodulation, powering and communication; for personalised ultrasound, in emerging markets including point-of-care solutions and patches for continuous monitoring. In the last decades, Micromachined Ultrasonic Transducers (MUTs) have been developed offering high-volume, miniaturisable and cost-effective MEMS transducers. They present an alternative to the most common PZT (lead zirconate titanate) based transducers, which have limitations such as high labour costs, due to manual assembly, and toxic materials (lead), which limit the in-body use. Depending on the actuation mechanism, MUTs are categorised either as CMUTs or PMUTs. CMUTs are the protagonists of this thesis.

Despite numerous advantages compared to their counterparts, one significant disadvantage of CMUTs is the requirement for a DC bias voltage, which limits the miniaturisation of the system and makes them unsuitable for in-body applications. However, special types of CMUTs can be fabricated with a charge trapping layer embedded in their dielectric. By trapping enough charge in this layer, the device can be operated in collapse-mode without a DC bias. These devices are called pre-charged CMUTs. The aim of this thesis is to investigate pre-charged collapse-mode CMUTs and evaluate their performance and their suitability as candidates for replacing standard externally biased CMUTs or other ultrasonic transducers.

A first generation of CMUT devices with an ALD Al_2O_3 charge storage layer embedded in the dielectric was completely electrically and acoustically characterised, achieving good results. Therefore, a second generation of pre-chargeable CMUTs was designed and fabricated. The aim was to compare the performance of ALD Al_2O_3 and PECVD Si_3N_4 as charge storage layers, and the effect of the insulating layer thickness in contact to the bottom electrode of the devices. The results showed an improved performance with respect to the first generation, and a performance comparable to standard

externally biased CMUTs. Accelerated lifetime tests were also performed to assess the static and dynamic lifetime, representing respectively storage and transmit mode conditions, and the relative performance degradation, showing promising results.

In this thesis, the target application of the pre-charged CMUTs was as ultrasonic power receivers for implantable devices. Lateral and angular misalignment can cause significant power losses due to uneven phase distribution across the receiver area. Their impact was assessed by means of simulations and verified with experimental data. The results showed that angular misalignment is the most detrimental, and it worsens as the frequency increases. Three solutions were proposed and discussed. Decreasing the frequency, which is an overall valid solution, yet with challenges related to the design of MUT transducers for lower frequencies. Using a partitioned receiving transducer, which is mainly useful in compensating the effects of angular misalignment, however bringing increased complexity in circuitry and packaging. Using a linear or matrix array transmitting transducer with a beamforming algorithm, such as the phase reversal algorithm, which was demonstrated to be highly effective in compensating for lateral misalignment.

After analysing how the power at the receiver is affected by lateral and angular misalignment, the power conversion efficiency of the pre-charged CMUTs was experimentally evaluated. When connected to an optimally matched load, efficiencies up to 80 % were achieved. The efficiency was also evaluated for a resistive load, reaching values of about 50 %. These values were achieved at 2.5 MHz, which is close to the centre frequency of the device by design, and are in line with the highest performances achieved by other groups using PZT crystals. However, PZT is not biocompatible, showing the great potential of the pre-charged CMUTs in biomedical applications.

Finally, the first ultrasonically powered implantable device using pre-charged CMUTs as power receivers was built and its functionality demonstrated. The objective was to demonstrate battery charging by means of ultrasound of a commercial device used to monitor the healing process of fractured bones. Ultrasonic powering was achieved with a total system efficiency of 21 % for an average ultrasound intensity of approximately 7 % of the FDA safety limit at the surface of the pre-charged CMUT receiver. Even if further improvements in efficiency are possible, this performance is already significantly better than other reported implantable devices employing PMUT or PZT transducers as receivers.

SAMENVATTING

De ontwikkeling van nieuwe technologieën draagt bij aan een versnelling van de innovatie in de gezondheidszorg, waardoor een meer gepersonaliseerde en gedecentraliseerde zorg mogelijk wordt. Door het vervagen van de grenzen tussen de farmaceutische, medische en de elektronische industrie, zijn nieuwe medische gebieden ontstaan zoals "bioelectronic medicines" en gepersonaliseerde ultrasound. Ultrasound speelt in beide gebieden een belangrijke rol. In implantaten kan het gebruikt worden om zenuwen te stimuleren of om met het implantaat te communiceren en die van energie te voorzien, terwijl in ultrasound nieuwe markten aan het ontstaan zijn voor point-of-care diagnostiek en voor continue (thuis) monitoring.

De ontwikkeling van ultrasound transducers die met microfabricage technologie (MUTs) worden gefabriceerd, opent de weg naar massafabricage, miniaturisatie en prijsreductie. Ze vormen een aantrekkelijk alternatief voor de traditionele PZT (loodzirkoniumtitanaat) gebaseerde transducers die veel handwerk vereisen, daarom duur zijn en die bovendien milieuonvriendelijk lood bevatten, waardoor toepassingen in het lichaam beperkt zijn. Er zijn twee soorten MUTs: PMUTs and CMUTs. CMUTs zijn het onderwerp van dit proefschrift.

Een nadeel van CMUTs in vergelijking met PMUTs is dat CMUTs een gelijkstroom voorspanning nodig hebben, wat de mogelijkheden tot miniaturisatie enigszins beperkt en toepassingen in het lichaam bemoeilijkt. Door de CMUTs echter te voorzien van een laagje waarin lading kan worden opgeslagen, kunnen zogenaamde pre-charged CMUTs worden gemaakt die geen voorspanning nodig hebben. In dit promotieonderzoek wordt deze technologie onderzocht en verder ontwikkeld, met als uiteindelijk doel te evalueren of ze standaard CMUTs met een externe voorspanning kunnen vervangen.

Om te beginnen werd een eerste generatie pre-charged CMUTs met een ALD Al_2O_3 ladingsopslag-laag elektrisch en akoestisch gekarakteriseerd. Dit resulteerde in de ontwikkeling en fabricage van de tweede generatie experimentele pre-charged CMUTs. Hierbij werd PECVD Si_3N_4 als ladingsopslag-laag vergeleken met ALD Al_2O_3 en werd het effect van een diktevariatie in het isolatielaagje dat in contact is met de bodem electrode bestudeerd. De tweede

generatie CMUTs vertoonde betere prestaties ten opzichte van de eerste generatie en liet zich goed vergelijken met standaard CMUTs met een externe voorspanning.   Ook versnelde statische en dynamische levensduurtesten, respectievelijk overeenkomend met het gebruik in ontvangst- en zendmodus, zagen er veelbelovend uit.

De belangrijkste toepassing voor de pre-charged CMUTs in dit proefschrift is het gebruik als ultrasone ontvanger in elektronische medische implantaten die van energie worden voorzien door middel van gefocusseerd ultrasound. In deze toepassing kunnen echter laterale- en hoek-uitrichtfouten resulteren in aanzienlijke verliezen, als gevolg van een ongelijk fase distributie over het oppervlak van de CMUT. Het effect hiervan werd bepaald door middel van simulaties en experimenten. Deze lieten zien dat een hoek uitrichtfout het grootste effect heeft, wat ook nog eens verergert bij toenemende frequentie. Drie mogelijke mitigatie strategieën worden voorgesteld en uitgewerkt. Ten eerste kan de ultrasound frequentie worden verlaagd, maar dit stuit op een gegeven moment op praktische CMUT-fabricage bezwaren. Ten tweede werd gedemonstreerd hoe het transduceroppervlak kan worden gepartitioneerd in segmenten. Alhoewel effectief, brengt dit wel weer additionele circuit- en assemblagecomplexiteit met zich mee. Als laatste werd een techniek gedemonstreerd waarbij - als voor de ultrasound zender een zend array wordt gebruikt – door middel van een fase-spiegeling algoritme met name laterale uitrichtfouten gecompenseerd kunnen worden.

Tenslotte werd de conversie efficiency van de pre-charged CMUTs experimenteel bepaald. Met een optimaal aangepaste belasting werd een efficiency van 80 % gehaald. Zelfs met een niet aangepaste, ohmse belasting werd nog een efficiency van 50 % gerealiseerd. Deze resultaten werden gemeten bij een frequentie van 2.5 MHz, welke dicht in de buurt van de resonantiefrequentie van de gebruikte CMUTs lag. De gemeten efficiencies zijn vergelijkbaar met de beste gepubliceerde resultaten die gebruik maken van PZT-transducers. Deze laatste zijn echter niet biocompatibel. Biocompatibel pre-charged CMUTs zullen hierdoor een belangrijke bouwsteen zijn voor toekomstige elektronische medische implantaten.   Als laatste wordt 's werelds eerste implantaat gedemonstreerd welke gebruik maakt van ultrasone energievoorziening met pre-charged CMUTs als transducer. Hierbij wordt uitgegaan van een commercieel verkrijgbaar implantaat dat wordt gebruikt om botheling te monitoren. Vervolgens wordt aangetoond hoe de batterij van het implantaat kan worden opgeladen met ultrasound. De behaalde overall systeem efficiency werd vastgesteld op 21 %, waarbij de akoestische energie ter hoogte van het CMUT-oppervlak kleiner was dan 7 % van de door de FDA gedefinieerde veiligheidsgrens. Alhoewel deze efficiency nog kan

worden verbeterd, zijn deze prestaties significant beter in vergelijking met andere gepubliceerde resultaten waarbij gebruik wordt gemaakt van PMUT of PZT-transducers.

NOMENCLATURE

ALT Accelerated Lifetime Test

ASIC Application Specific Integrated Circuit

BVD Butterworth-Van Dyke model

CMUT Capacitive Micromachined Ultrasonic Transducer

DC Direct current

ECS Electronic Components and Systems

EOT Equivalent Oxide Thickness

FDA Food and Drug Administration

IMD Implantable Medical Device

MEMS Micro-Electro-Mechanical System

MIM Metal Insulator Metal

PCB Printed Circuit Board

PMIC Power Management Integrated Circuit

PMU Power Management Unit

PMUT Piezoelectric Micromachined Ultrasonic Transducer

PZT Lead Zirconate Titanate transducer

RX Receiving transducer

SEM Scanning Electron Microscope

TX Transmitting transducer

US Ultrasound

1

INTRODUCTION

1.1. FUTURE HEALTH: AGEING AND ELECTRONICS INNOVATIONS

Thanks to advancements in healthcare research and innovation, the global population is ageing, leading to a rise in healthcare costs. This poses a significant challenge for the future, as one in three adults suffers one or multiple chronic diseases [1]. In 2022, the costs associated with the treatment of these diseases, constituted approximately 9.2 % of the GDP [2].

However, novel technologies are giving rise to significant opportunities for both industry and society, by improving accessibility and affordability of healthcare. These advancements boosted the development of innovative electronic devices and applications that respond to the healthcare societal demands of decentralisation, and personalization. Decentralisation is aiming to treat individuals at home whenever feasible, to reduce hospitalisation costs and enhance well-being, and personalization aims to provide tailored treatments to individual patients to maximise effectiveness.

The emergence of these novel devices is a result of the diminishing boundaries between the conventional sectors of Pharma, MedTech, and the ECS (Electronic Components and Systems) industry. This convergence has given rise to new medical domains with significant potential for both society and industry [3]. Among these emerging medical domains are bioelectronic medicines and point-of-care and wearable ultrasound. In the next paragraphs, both topics will be introduced as they constitute the primary applications within the scope of this thesis.

1

1.2. BIOELECTRONIC MEDICINES

In recent decades, active implantable devices such as deep brain stimulators, spinal cord stimulators, and cochlear implants have been successfully used to treat chronic conditions with minimal side effects. These devices are categorised as bioelectronic medicines and they employ electrical, magnetic, or other stimulus to modulate the neural activity as an alternative to pharmacological and surgical approaches [7].

Nevertheless, the upcoming generation of neuromodulation devices necessitates several new key features. These include **miniaturisation**, enabling more compact designs; **wireless powering**, for remote charging of the implant, and to eliminate the need for battery replacement surgeries; **specificity**, to minimise potential side effects; and **closed-loop operation**, ensuring the delivery of treatment only when necessary and with the appropriate intensity and pattern [8]. These advancements have already begun implementation in certain devices, as illustrated in Fig. 1.1. However, it is important to emphasise that this marks just the beginning of the transformative journey in this field.

1.2.1. BUILDING BLOCKS OF AN IMPLANTABLE MEDICAL DEVICE

Figure 1.2 illustrates a schematic of an implantable medical device (IMD). Sensors and actuators are used to sense and stimulate the neural tissue to be treated. These components connect to an ASIC (Application Specific Integrated Circuit), responsible for processing the sensed signals and determining the therapeutic intensity and pattern. The ASIC is also connected and powered by

(a)   (b)   (c)

Figure 1.1.: Examples of implantable medical devices available on the market, also showing the trend of miniaturisation of these devices. (a) Spinal cord stimulator from Boston Scientific [4]. (b) One of the world smallest pacemakers from Medtronic, compared to its predecessor [5]. (c) Inductively powered vagus nerve stimulator from SetPoint Medical [6].
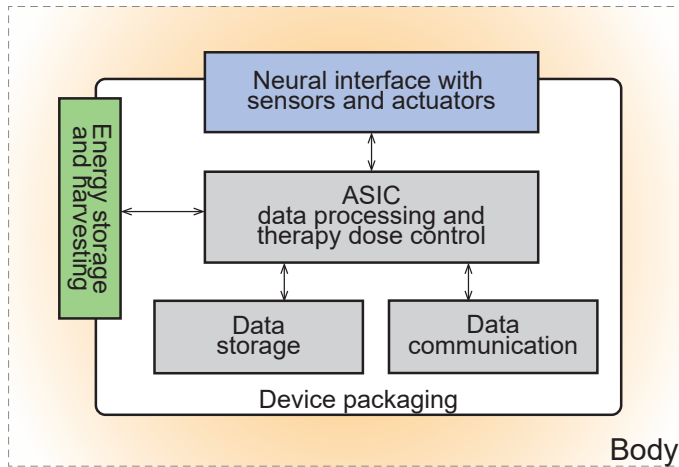
Figure 1.2.: Schematic system diagram of the next generation implantable medical devices. Figure adapted from [8].

the energy storage and harvesting unit, and the sensed and processed data are stored or communicated with other dedicated components blocks. Ultimately, the entire system is packaged to ensure protection for both the implant and the body.

NEUROMODULATION METHODS

The two most common means to modulate - either stimulate or inhibit - the neural activity are electrical and magnetic stimulation. However, they both generally lack spatial specificity and can be highly invasive. As an alternative, ultrasound emerged in the last decades, offering higher specificity, thanks to its focusing ability due to its short wavelength, and its reversible effects [7].

FUNCTIONALITIES INTEGRATION CENTRE

All smart IMDs include an integration centre, represented by the ASIC, which manages power, memory, and communication units, for the transmission and reception of data. Among these three components, the power management block poses the greatest challenge. Batteries are the prevalent energy source, but they have limitations such as a finite lifespan, and the presence of chemicals which requires hermetic encapsulation. Alternative power sources that are being investigated include bio-fuel cells, piezoelectricity, thermoelectricity and electrostatics. However, these alternatives encounter numerous challenges, and frequently the power they can generate is barely sufficient for the operation of an IMD [9].

1

Therefore, research is focusing on developing innovative solutions for efficient wireless energy transfer. Among the wireless powering methods, the three main alternatives are: inductive coupling, radio frequency and ultrasonic power transfer. Ultrasound has gained interest over inductive coupling and radio waves because it can be precisely focused, and it has relatively small propagation losses in the body (around $0.6\,\text{dB/(cm\,MHz)}$) for its typical range of operation frequencies. In addition, the FDA limit for the safe use of ultrasound in the body ($720\,\text{mW/cm}^2$) allows to transfer enough energy to power an IMD.

DATA STORAGE, TRANSMISSION AND RECEPTION

Data transmission and reception is another essential component. Most wireless implants use RF communication. However, this can be inefficient due to RF absorption in biological tissue. One of the promising alternatives is ultrasound. Ultrasound can be used for both active and passive communication, yet with a lower data rate compared to RF [10]. Finally, the on-board memory must store the sensed data, posing challenges related to factors like lifetime and reliability [8].

DEVICE PACKAGING

Additionally, the packaging must be either hermetic or non-hermetic based on the biocompatibility of the IMD components. It should also allow, in case of wireless powering, the transfer of energy to the receiver on the IMD.

1.2.2. ULTRASOUND FOR BIOELECTRONIC MEDICINES

From the previous paragraphs, it likely caught the reader's attention that ultrasound stands as a recurrent element across various components of an IMD. Its applications range from modulating neural activity to serving as a medium for wireless powering and communication. However, despite its versatility, no implantable devices that employ ultrasound for neuromodulation, power transfer or communication are commercially available. The majority of such devices are primarily outcomes of academic research rather than being accessible in the commercial market. Several factors contribute to this gap.

Firstly, even though the effects of ultrasonic neuromodulation were uncovered almost a century ago, the scientific community has not yet reached a consensus on the precise mechanisms responsible for exciting or inhibiting neurons using ultrasound [11]. Ambiguity persists regarding the specific parameters influencing neural stimulation or inhibition, with significant differences between the central and peripheral nervous system. Nevertheless,

the increase in number of studies on ultrasound neuromodulation is significant in the last decade, highlighting the growing interest in this form of neuromodulation (Fig. 1.3).

The second challenge lies in the prevalent use of off-the-shelf transducers based on PZT technology, which lack biocompatibility. Consequently, these transducers require hermetic encapsulation, that obstructs ultrasound from reaching the IMD, hindering wireless power transfer. Despite this concept is well-established, the absence of suitable devices safe for implantation has been an obstacle to its practical application. An analysis of the number of studies investigating ultrasonic powering for implantable devices reveals in fact only a marginal increase in the last decade (Fig. 1.3).

In recent decades, emerging technologies like micromachined Ultrasonic Transducers (MUT) devices have shown promising advancements. These technologies offer biocompatibility and the possibility of miniaturisation, along with seamless integration with integrated circuits (IC). Yet, these technologies still require optimisation before they can be integrated into an implantable device. Furthermore, they are not readily available off-the-shelf, primarily due to limited production by a few companies, and the high costs associated with their fabrication.
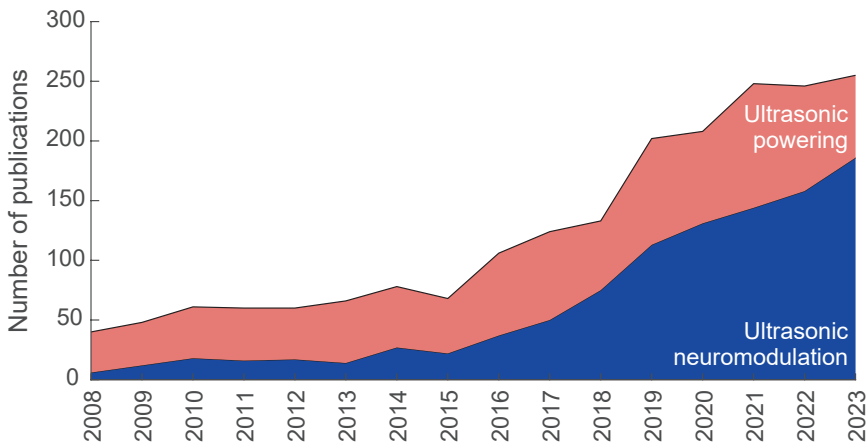
Figure 1.3.: Number of publications per year on ultrasonic powering and neuromodulation, in the last 15 years. Graph obtained from researching the terms "ultraso* power* implant*" and "ultraso* neuromodulation" in the Web of Science database in February 2024.

1

1.3. POINT-OF-CARE AND PERSONALISED ULTRASOUND

Since the first experiments with ultrasound imaging for medical diagnostics by Douglas Howry in 1948, ultrasound imaging has developed into an extremely versatile diagnostic tool that is serving almost all branches of medical care. Despite its versatility, ultrasound diagnostics is mainly used in clinical settings for two reasons: high costs, and the need for a sonographer. At the moment more than 99 % of all ultrasound probes use (poly)crystalline PZT material for the transducer element. These transducers are mainly reserved for professional use and they need to be manually assembled, adding labour cost and variability in the samples.

Nevertheless, the global ultrasound market is expected to grow from around 6 million dollars in 2022 to almost 8 million dollars by 2028, with a Compound Annual Growth Rate (CAGR) of 6 % [12]. This growth can be attributed to the increasing use of ultrasound in diagnostics and the deployment of handheld point-of-care probes for remote healthcare. The main driver of this growth is the development of high-volume, cost-effective MEMS ultrasound transducer technologies. In fact, MUT technologies, constituting only 8 % of the total market in 2022, are expected to account for approximately 26 % by 2028 [12].

MEMS ultrasonic transducers are batch fabricated in cleanroom facilities, therefore they offer flexibility in the design and the possibility for miniaturisation, eliminating the need for manual assembly. These advantages, compared to bulk piezo transducers, allowed them to enter the consumer market. Butterfly Network has already introduced an handled probe which uses Capacitive Micromachined Ultrasonic Transducer (CMUT) as transducers, and the field is expected to grow in the coming years. In addition, using MEMS ultrasonic transducers encourages the development of disposable wearables designed for monitoring, which are expected to become the preferred choice for remotely and continuously monitoring various pathologies.

1.4. MICROMACHINED ULTRASONIC TRANSDUCERS

It is therefore clear that Micromachined Ultrasonic Transducers (MUT) are a significant protagonist in the future landscape of healthcare. Micromachined Ultrasonic Transducers (MUT) consist of a suspended membrane over a vacuum gap. Through the vibration of this membrane, ultrasound can be transmitted into, or received from the medium interfacing the membrane. Due to this thin membrane structure, MUTs have a broader bandwidth compared to conventional PZT transducers. In addition, depending on the actuation mechanism, MUTs can be categorised either as CMUTs or PMUTs. CMUTs are actuated electrostatically with an opposing electrode beneath the vacuum gap,

while PMUTs are actuated with a thin-film piezoelectric material embedded within the top membrane. The most common used materials for PMUTs membrane are thin film piezo materials, (Sc doped)-AlN and polymers.

PMUTs are currently mainly used in consumer applications such as fingerprint sensing, while CMUTs mainly cover the medical market [12]. However, they are both promising technologies for the medical imaging market, and when fabricated with a low temperature process they can be processed on CMOS ASIC, therefore offering the possibility for monolithic integration. PMUTs are better suited for the lower frequency range, and CMUTs for the higher frequency range. In addition, CMUTs at present offer on average higher transmit and receive sensitivity, with higher bandwidth - usually around 100 % - than PMUTs [13].

Nevertheless, one of the disadvantages of CMUTs is the need for an external DC bias voltage, ranging between 50 to 100 V. This is required to bring the top membrane closer (non-collapse-mode), or in contact (collapse-mode) to the bottom dielectric, enhancing the CMUT sensitivity. This requires external circuitry, limiting miniaturisability, and is not desirable for medical applications.

1.4.1. ADVANCING THE STATE OF THE ART

To eliminate the need for an external bias voltage, special types of CMUTs can be fabricated with a charge trapping layer embedded in their dielectric. By trapping enough charge, the device can be operated in collapse-mode without a DC bias. The concept of dielectric charging is not new, however only a
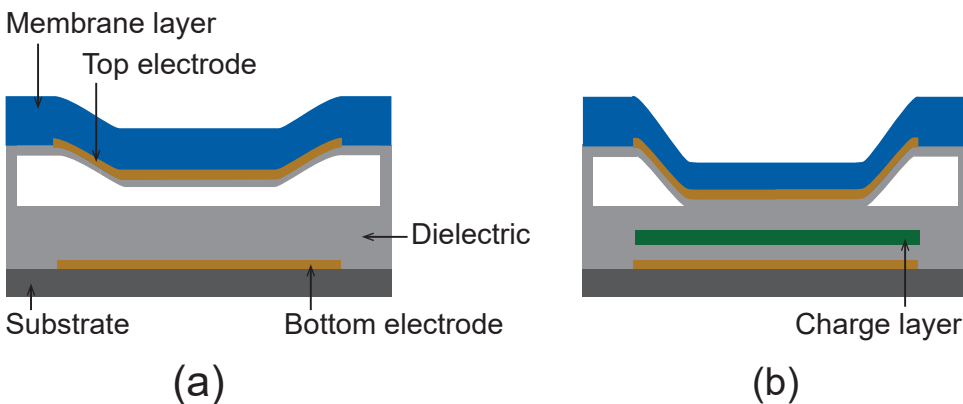
Figure 1.4.: Schematic representation of CMUTs. (a) Standard devices. (b) Pre-chargeable collapse-mode devices, highlighting the position of the charge storage layer in the dielectric.

1

few groups investigated this concept applied to CMUTs [14–19]. Dielectric charging, in fact, is usually seen as a reliability issue in MEMS devices since it causes instability of the device characteristics up to the point at which the device fails [20–23]. The few groups that investigated pre-charged CMUTs used SiO_2 or Si_3N_4 as material for the charging layer. However, most of them produced out of collapse CMUTs, with the exception of Ho et al. who used a low frequency CMUT operating at $140\,kHz$ [15]. Choi et al. [18] compared the performance of Si_3N_4-SiO_2 and SiO_2 as charging layers, concluding that Si_3N_4 maintains its performance for a longer duration due to superior charge retention. What emerged from these studies was the need to store sufficient charge and ensure its stability over time. Leveraging the fundamental concept of dielectric charging from the semiconductor memory industry, materials employed in this domain can be integrated into the CMUT dielectric as a charge storage layer to develop stable pre-charged collapse-mode CMUTs.

1.5. MOTIVATION AND OUTLINE OF THIS THESIS

The primary objective of this research was to investigate pre-charged collapse-mode CMUTs evaluating their performance and their suitability as candidates for replacing standard externally biased CMUTs or other ultrasonic transducers, with a focus on their application for implantable devices. The outcomes of this research, however, can also be used to evaluate their potential use in other applications, such as imaging, for example in patches, or IVUS and ICE catheters, or even for neuromodulation, thanks to the design freedom and modularity of the CMUTs technology platform.

In the context of this thesis, several preliminary experiments using ultrasound for neuromodulation were also performed with the goal to set the ground for using CMUTs also for this purpose. Tests were performed both on neurons from the central and peripheral nervous system, achieving conflicting results. It is important to note that in studies involving biology, tests need to be replicated multiple times in a fixed setup with controlled experimental conditions to derive significant conclusions. Unfortunately, such extensive repetitive experiments were not feasible within the context of this thesis. The outcomes of ultrasonic stimulation of cultured neurons on Microelectrode-Arrays (MEAs) are presented in the publication titled "Focused ultrasound neuromodulation on a multiwell MEA" published in the Bioelectronic Medicine journal [24]. For the sake of clarity, this thesis exclusively presents the results related to pre-charged CMUTs.

This thesis is divided in three parts. In the **first part**, the performance of a first generation of CMUTs with an ALD Al_2O_3 charge storage layer embedded

1

in the dielectric was evaluated, revealing promising results. Therefore, in the context of the Moore4Medical project [25], a second generation of CMUT devices was fabricated. First, several Metal-Insulator-Metal (MIM) capacitors with different layer stack combinations were fabricated aimed at determining the best candidate stacks for the next generation pre-charged CMUT devices. After characterising the MIM capacitors, the second generation of pre-chargeable CMUT devices was fabricated and characterised. In the **second part** of this thesis, ultrasonic power transfer using the newly fabricated CMUTs is investigated. First, the effect of angular and lateral misalignment are assessed by means of simulations, and mitigation strategies are proposed and experimentally tested. The pre-charged CMUTs efficiency in receiving acoustic energy and converting it into usable electrical power is then evaluated for different charging conditions and load types. Ultimately, in the **third part**, the CMUTs are integrated into an existing commercial implantable device from *AO Foundation* used to monitor the progression of bone healing [26]. This device is battery powered and the goal is to demonstrate battery charging by means of ultrasound.

1.5.1. OUTLINE OF THIS THESIS

The remainder of this dissertation is organised as follows:

In Chapter 2, pre-charged collapse-mode CMUTs are introduced. A first generation of CMUTs fabricated with an ALD Al_2O_3 charge storage layer is modelled and characterised in terms of electrical and acoustical performance, and compared to state-of-the-art MUT devices.

In Chapter 3, MIM capacitors with different dielectric layer stack combinations are fabricated and characterised. Their dielectric contains a charge storage layer including PECVD Si_3N_4 or ALD Al_2O_3. The goal is to evaluate charge trapping and discharging providing a starting point for the design of the dielectric stack of the next-generation pre-chargeable CMUTs.

Chapter 4 presents the second generation of fabricated pre-chargeable CMUTs. They are electrically and acoustically characterised, similarly to the devices presented in Chapter 2. In this chapter, the important issue of device lifetime is also addressed by performing accelerated lifetime measurements.

Chapter 5 and 6 form the second part of this thesis. In Chapter 5, the impact of lateral and angular misalignment on ultrasonic power transfer is addressed by using ultrasonic field simulations and experimentally verifying the results.

Chapter 6 presents the power conversion efficiency results, which are

1

obtained through ultrasonic power transfer experiments with different load conditions.

Chapter 7 presents the fracture monitor demonstrator, introducing the components required for ultrasonic powering. Brief details on the device encapsulation and power management circuit are given, and the functionality is demonstrated by powering the device with ultrasound and successfully transmitting the data measured with a strain gauge via Bluetooth.

General conclusions and research recommendations are presented in Chapter 8.

REFERENCES

[1]   C. Hajat and E. Stein. "The global burden of multiple chronic conditions: A narrative review". In: *Prev Med Rep* 12 (2018), pp. 284–293.

[2]   *OECD Health Statistics 2023*. Web Page. URL: https://www.oecd.org/health/health-data.htm.

[3]   *Health.E Lighthouse*. Web Page. URL: https://www.health-lighthouse.eu/.

[4]   *Precision Plus: Spinal Cord Stimulator System*. Web Page. 2024. URL: https://www.bostonscientific.com/en-EU/products/spinal-cord-stimulator-systems/precision_plus.html.

[5]   *Micra AV2 leadless pacemaker*. Web Page. 2023. URL: https://www.medtronic.com/us-en/healthcare-professionals/products/cardiac-rhythm/pacemakers/micra-av2.html.

[6]   *SetPoint Medical*. Web Page. URL: https://setpointmedical.com/bioelectronic-medicine-therapy/.

[7]   O. Naor, S. Krupa, and S. Shoham. "Ultrasonic neuromodulation". In: *J Neural Eng* 13.3 (2016), p. 031003.

[8]   A. Lowe and N. V. Thakor. "The 2020 Roadmap for Bioelectronic Medicine". In: Springer Nature Singapore, 2023, pp. 3407–3445.

[9]   A. Amar, A. Kouki, and H. Cao. "Power Approaches for Implantable Medical Devices". In: *Sensors* 15.11 (2015), pp. 28889–28914.

[10] S. Kawasaki, I. Subramaniam, M. Saccher, and R. Dekker. "A microwatt telemetry protocol for targeting deep implants". In: *2021 IEEE International Ultrasonics Symposium (IUS)*. IEEE.

[11] H. A. S. Kamimura, A. Conti, N. Toschi, and E. E. Konofagou. "Ultrasound Neuromodulation: Mechanisms and the Potential of Multimodal Stimulation for Neuronal Function Assessment". In: *Frontiers in Physics* 8 (2020).

[12] *Ultrasound Sensing 2023*. Web Page. 2023. URL: https://www.yolegroup.com/product/report/ultrasound-sensing-2023/.

[13]   Health.E Lighthouse. *A European MEMS Ultrasound Benchmark [White Paper]*. Tech. rep. Nov. 2021. URL: https://www.s2e2.fr/wp-content/uploads/2022/03/CMUT-PMUT-Benchmark-Technical-Whitepaper.pdf.

[14]   A. Kshirsagar, A. Sampaleanu, R. Chee, W. Moussa, and R. J. Zemp. "Pre-charged CMUTs with efficient low-bias voltage operation for medical applications". In: *2013 IEEE International Ultrasonics Symposium (IUS)*. IEEE, 2013.

[15]   M.-C. Ho, M. Kupnik, K. K. Park, and B. T. Khuri-Yakub. "Long-term measurement results of pre-charged CMUTs with zero external bias operation". In: *2012 IEEE International Ultrasonics Symposium*. IEEE, Oct. 2012.

[16]   K. K. Park, M. Kupnik, H. J. Lee, O. Oralkan, and B. T. Khuri-Yakub. "Zero-bias resonant sensor with an oxide-nitride layer as charge trap". In: *2010 IEEE Sensors*. IEEE, Nov. 2010.

[17]   F.-Y. Lin, W.-C. Tian, and P.-C. Li. "CMOS-based Capacitive Micromachined Ultrasonic Transducers operating without external DC bias". In: *2013 IEEE International Ultrasonics Symposium (IUS)*. IEEE, July 2013.

[18]   W. Y. Choi, C. H. Lee, Y. H. Kim, and K. K. Park. "Comparison of Si_3N_4–SiO_2 and SiO_2 Insulation Layer for Zero-Bias CMUT Operation Using Dielectric Charging Effects". In: *IEEE Transactions on Ultrasonics, Ferroelectrics, and Frequency Control* 67.4 (2020), pp. 879–882.

[19]   M. Annayev, F. Y. Yamaner, and O. Oralkan. "A pre-charged CMUT structure with a built-in charge storage capacitor". In: *2022 IEEE International Ultrasonics Symposium*.

[20]   H. Martinussen, A. Aksnes, and H. E. Engan. "Investigation of charge diffusion in CMUTs using optical interferometry". In: *2008 IEEE Ultrasonics Symposium*. IEEE, Nov. 2008.

[21]   K. Midtbo and A. Ronnekleiv. "Analysis of charge effects in high frequency CMUTs". In: *2008 IEEE Ultrasonics Symposium*. IEEE, Nov. 2008.

[22]   L. L. P. Wong, S. Na, A. I. H. Chen, and J. T. W. Yeow. "A novel method for measuring dielectric charging of CMUT arrays". In: *2014 IEEE International Ultrasonics Symposium*. 2014, pp. 185–188.

[23]   R. Van Schaijk, M. In 'T Zandt, P. Robaeys, M. Slotboom, J. Klootwijk, and P. Bekkers. "Reliability of collapse mode CMUT". In: *2023 IEEE International Ultrasonics Symposium (IUS)*. IEEE, 2023.

[24]   M. Saccher, S. Kawasaki, M. P. Onori, G. M. van Woerden, V. Giagka, and R. Dekker. "Focused ultrasound neuromodulation on a multiwell MEA". In: *Bioelectronic Medicine* 8.1 (2022), p. 2.

[25]   *Moore4Medical*. Web Page. URL: https://moore4medical.eu/.

[26]   *AO Fracture Monitor*. Web Page. 2023. URL: https://www.aofoundation.org/what-we-do/innovation-translation/innovation-funding/portfolio/fracture-monitor.

2

THE FIRST-GEN PRE-CHARGED CMUTS

This chapter is a verbatim copy of the following paper, and only section and figure numbers were changed to comply with the format of this thesis:

- M. Saccher[*], S. Kawasaki[*], J. H. Klootwijk, R. Van Schaijk, and R. Dekker. "Modeling and Characterization of Pre-Charged Collapse-Mode CMUTs". In: *IEEE Open Journal of Ultrasonics, Ferroelectrics, and Frequency Control* 3 (2023), 14–28. *These authors should be ragarded as joint first author.

2.1. INTRODUCTION

Visualizing the inside of the body by using ultrasound has mainly been limited to the hospital environment over the last three to four decades [2]. These hospital environments required high-quality ultrasound systems to make accurate diagnoses, leading to drastically improved performance of the ultrasound equipment [3]. However, in recent years, there has been an emerging low-end ultrasound market that accommodates new customer/patient demands, such as using ultrasound to continuously monitor the status of various visceral organs (i.e., heart, bladder), or as a handheld ultrasound system that can be connected to a smartphone to make on-site visualization in resource-limited settings [4, 5]. Furthermore, ultrasound transducers are expanding their application from a diagnostic tool to wireless

---

The CMUTs modelling, fitting with DHM measurements, and transmit and receive sensitivity measurements were performed by S. Kawasaki.

power receivers that can be used within the human body to power the next generation of implantable devices [6–8]. The requirements for these new applications are different compared to the traditional high-end diagnostic ultrasound market, which solely focused on image quality, and not on challenges such as connectivity to the internet, portability, lower price, biocompatibility, and manufacturing scalability to name a few. However, the current manufacturing processes based on lead zirconate titanate (PZT) ultrasound transducer devices do not meet these requirements. Limitations include the inherent labor cost associated with the manual assembly of PZT transducers or the use of toxic metals (lead), which limits in-body use.

Alternatively, micromachined ultrasonic transducers (MUTs) can be used and made biocompatible. MUTs have a suspended membrane over a vacuum gap, and through the vibration of this membrane, ultrasound can be transmitted into, or received from the medium interfacing the membrane. Due to this thin membrane structure, MUTs have a broader bandwidth compared to conventional PZT transducers. MUTs are fabricated through standard IC-based fabrication processes, making them CMOS compatible, enabling mass production and simple integration with peripheral electronics at a lower cost. Depending on the actuation mechanism, MUTs can be categorized either as CMUTs (Capacitive Micromachined Ultrasound Transducers) or PMUTs (Piezoelectric Micromachined Ultrasound Transducers). CMUTs are actuated electrostatically with an opposing electrode beneath the vacuum gap. Alternatively, PMUTs are actuated with a thin-film piezoelectric material embedded within the top membrane.

Comparing these two technologies, CMUT technology has matured to the level that they are now used in commercially available point of care applications [5]. In addition, a recent benchmark of the performance parameters of CMUTs and PMUTs executed by European companies and institutes showed that CMUTs have the best overall acoustical performance, with higher receive and transmit sensitivity than most of the PMUT devices [9]. Typical values of receive sensitivity for CMUTs range between 2.5 and 10 V/MPa and transmit sensitivity ranges from 4 to 23 kPa/V. The downside of using CMUTs is the (large) DC bias voltage required for their operation. Typically, around 50 V to 100 V is needed to bring the top membrane closer (non-collapse mode) or in contact (collapse-mode) to the bottom membrane to increase the electric field strength, which increases the sensitivity of these devices. This leads to three undesired consequences. In the first place, the high DC voltage source requires additional board space limiting the portability/miniaturizability of these devices. Secondly, the reliability of individual transducers is coupled to other transducers since one shorting

element will inadvertently affect the DC bias voltage connected to the other elements and thirdly, large bias voltages are not desirable for medical applications, where patient safety is of paramount importance.

In this work, we propose a pre-charged collapse-mode CMUT for in-body applications that can operate without an external bias voltage and where there is sufficient built-in charge to keep the CMUT in collapse-mode. To accomplish this, we use the dielectric charging behavior of Al_2O_3. Dielectric charging is usually seen as a reliability issue in MEMS devices since it causes instability of the device characteristics up to the point at which the device fails [10–12]. On the other hand, the concept of dielectric charging is at the base of the semiconductor memory industry [13–15], and other groups have already experimentally applied it to CMUT devices to achieve reduced or zero-bias operation [16–20]. High-k materials such as Si_3N_4 or HfO_2 could be used for this application [21], as investigated by Park et al. [19] and Choi et al. [16], who demonstrated the feasibility of pre-charged CMUTs with Si_3N_4 as dielectric showing good charge retention over time, even at high temperatures. Charge retention over time represents the major challenge for these devices and, depending on the application, the minimum lifetime can vary from hours in the case they are part of a disposable device, or a few months for acute applications, to years. Most of the studies concerning pre-charged CMUTs investigated non-collapse mode operation since the amount of charge stored in the device was not enough to keep the membrane in contact with the bottom membrane. This depends on the material of the dielectric layer, the deposition method and the structure of the device. To the authors knowledge, only one pre-charged collapse-mode device has been published in literature [18], however operating at low frequency (140 kHz) and without reporting the acoustic performance and lifetime.

The aim of this paper is to show that it is possible to obtain pre-charged collapse-mode CMUTs using Al_2O_3 as charge trapping layer, and to present a comprehensive analysis of the device characteristics and performance through modeling and measurements. The remainder of this paper is organized as follows: the first section introduces a model of the pre-charged CMUT which is an extension of the work presented by Koymen et al. [22] where a CMUT was modeled assuming two types of built-in charges: surface charge of the opposite polarity at both sides of the charging layer forming an electret, and spatially fixed volume charge uniformly distributed within the charging layer. In the second section, four CMUT devices, each with a different layer stack are introduced. A description of the methods used to characterize the devices and fit the model are presented, followed by their results in the next section. It is shown that this model well describes the characteristics of the

four CMUTs and that it can be used to estimate the type and amount of built-in charges. In the third section, the performance of the pre-charged devices in terms of transmit and receive sensitivity, and output pressure is evaluated. In addition, the effect of different charging parameters (e.g. charging temperature, charging voltage and polarity, and charging duration) on the amount of charge stored in the CMUTs is studied, resulting in a general relationship. The final part of this section presents the estimated lifetime of these devices obtained from charge retention studies by means of accelerated lifetime tests.

2.2. MODELING THE PRE-CHARGED CMUT

This section introduces a theoretical model of the collapse-mode CMUTs with a built-in charge layer. A schematic representation of the pre-charged collapse-mode CMUT is shown in Fig. 2.1 (a). In this model, the CMUT is modeled as a vibrating axisymmetric clamped membrane. The charging layer is embedded between the top and bottom electrodes, separated by an insulation layer. In Fig. 2.1(a), t_m is the thickness of the top membrane, which includes the SiO_2 dielectric layer, the top electrode and the Si_3N_4 membrane layer. ρ_{tp} is the mass density of the top membrane, t_g is the height of the vacuum gap and $w(r)$ is the displacement of the membrane along the radial direction r. The voltage V is defined with respect to the bottom electrode as in the remainder of this paper. Fig. 2.1(b) denotes the forces acting on the top
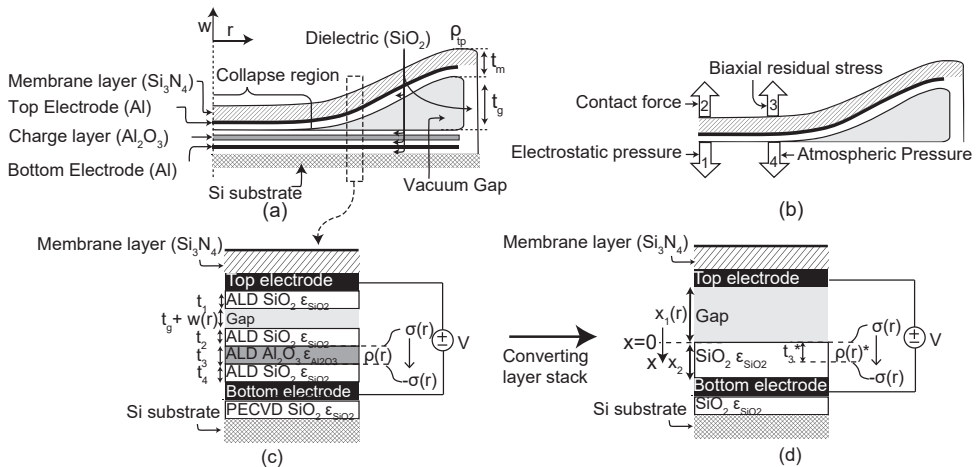
Figure 2.1.: (a) Cross section of the CMUT. (b) Forces acting on the top membrane. (c) Expanded view of the CMUT layer stack. (d) Converted layer stack.

membrane which are 1) the electrostatic pressure resulting from the built-in charge and the external voltage, 2) the contact force which is the reactive force that occurs where the top membrane touches the bottom membrane, 3) the uniform biaxial residual stress and 4) the atmospheric pressure.

According to [23], the governing dynamic equation without the built-in charge is given by:

$$
\rho_{tp} t_m \frac{\partial^2 w(r,t)}{\partial^2 t} + D \nabla_r^4 w(r,t) = - \frac{\varepsilon_0}{2(t_{eff} + w(r,t))^2} V(t)^2
$$
$$
+ \frac{H_{ab}}{2} \text{erfc}\left(\frac{t_g + w(r,t)}{\sigma_m \sqrt{\pi}} \right)
$$
$$
+ \frac{\tau t_m}{r} \frac{\partial}{\partial r}\left(r \frac{\partial w(r)}{\partial r} \right) \tag{2.1}
$$
$$
- P_{atmos}
$$

$$
\nabla_r^4 = \left(\frac{\partial^2}{\partial r^2} + \frac{1}{r} \frac{\partial}{\partial r} \right)^2. \tag{2.2}
$$

The four terms on the right side of (2.1) correspond to the four different forces previously mentioned. Furthermore, D is the flexural rigidity of the top membrane, $V(t)$ is the external voltage applied to the top membrane, σ_m is the standard deviation of the combined surface roughnesses, H_{ab} is the indentation hardness, τ is the uniform biaxial residual stress, erfc is the complementary error function, and t_{eff} is the effective gap height between the top and bottom electrode corrected for the dielectric constants, which is defined as:

$$
t_{eff} = t_g + \sum \frac{t_i}{\varepsilon_i}, \tag{2.3}
$$

where t_i, is the thickness of the dielectric layers between the top and bottom electrodes divided by their corresponding dielectric constants. For further details, readers are referred to [23]. In this work, (2.1) was adapted by adding the electrostatic force from the built-in charge.

Fig. 2.1(c) is a cross-section of the CMUT at an arbitrary radius r. In this figure, the dielectric layer thickness is denoted as t with a subscript from 1 to 4. The charge trapping layer has a dielectric constant of $\varepsilon_{Al_2O_3}$ and is sandwiched between two SiO$_2$ layers. The charge distribution within the charge trapping layer is defined by a homogeneous charge of $\rho(r)$ [C/m^3] inside the charging layer, as well as a downwards polarization induced by a surface charge of $\sigma(r)$ [C/m^2] with opposite polarities on both sides of the charging layer.

Due to the multiple dielectric constants used in this layer stack, there is no simple solution that can be directly used to calculate the electrostatic force. However, for a simpler model as the one shown in Fig. 2.1(d), where there is only one dielectric layer on one side of the electrode, and the other side is a vacuum gap, G.M.Sessler [24] derived the electrostatic pressure on the top electrode for a generalized charge distribution within the dielectric layer. Thus, the electrostatic force on the top membrane can be derived by converting the layer stack and the charge distribution of Fig. 2.1(c) to Fig. 2.1(d). By comparing Fig. 2.1(c) to Fig. 2.1(d) we see that:

$$
\begin{aligned}
x_1(r) &= t_g + w(r) + \frac{t_1 + t_2}{\varepsilon_{SiO_2}} \\
x_2 &= t_4 + t_3 \frac{\varepsilon_{SiO_2}}{\varepsilon_{Al_2O_3}}.
\end{aligned}
\tag{2.4}
$$

In these two equations, t_1, $t_g + w(r)$ and t_2 are converted to $x_1(r)$ which has a relative permittivity of vacuum and t_3, t_4 are converted to x_2 which has a relative permittivity of SiO$_2$. For convenience, we denote $t_3^* = t_3 \frac{\varepsilon_{SiO_2}}{\varepsilon_{Al_2O_3}}$ in the following derivation. Since the total amount of charge should not change, the charge distribution is scaled as $\rho^*(r) = \rho(r) \frac{\varepsilon_{Al_2O_3}}{\varepsilon_{SiO_2}}$ so that $\rho^*(r)t_3^* = \rho(r)t_3$. As a result, the charge distribution for the equivalent layer stack is:

$$
\rho^*(r,x) = \begin{cases} \sigma(r)\delta(x) - \sigma(r)\delta(x - t_3^*) + \rho^*(r), & \text{if } 0 \le x \le t_3^* \\ 0 & \text{otherwise} \end{cases}
\tag{2.5}
$$

where $\delta(x)$ is a dirac delta function used to express the surface charge density. Referring to [24] (eq. 14 and eq. 34), the electrostatic pressure acting on the top membrane for a generalized charge distribution is:

$$
P_e(r) = -\frac{\varepsilon_0}{2s(r)^2}\left(V - V_{eff}(r)\right)^2
\tag{2.6}
$$

where

$$
V_{eff}(r) = \frac{x_2 \sigma_1(r)}{\varepsilon_0 \varepsilon_{SiO_2}}
\tag{2.7}
$$

$$
s(r) = t_{eff} + w(r)
\tag{2.8}
$$

and

$$
\sigma_1(r) = \frac{1}{x_2}\int_0^{x_2}(x_2 - x)\rho^*(r,x)\,dx.
\tag{2.9}
$$

From (2.6), the force from the internal charge acts effectively as if a voltage of $V_{eff}(r)$ is subtracted from the external voltage V. The only unknown value in

this equation is $\sigma_1(r)$, which is the contribution of the surface and the volume charges. By inserting (2.5) into (2.9) and integrating, we find:

$$\sigma_1(r) = t_3 \left(1 - \frac{t_3^*}{2x_2} \right) \rho(r) + \frac{t_3^*}{x_2} \sigma(r). \tag{2.10}$$

From this result, $\sigma_1(r)$ is characterized as the sum of the volume charge (1st term) and the surface charge (2nd term). Finally, we include the modified electrostatic pressure by including the internal charge (2.6) into the membrane dynamics (2.1) as:

$$
\begin{aligned}
\rho_{tp} t_m \frac{\partial^2 w(r,t)}{\partial^2 t} + D\nabla_r^4 w(r,t) = &-\frac{\varepsilon_0}{2(t_{eff} + w(r,t))^2} \left(V(t) - V_{eff}(r) \right)^2 \\
&+ \frac{H_{ab}}{2} \mathrm{erfc}\left(\frac{t_g + w(r,t)}{\sigma_m \sqrt{\pi}} \right) \\
&+ \frac{\tau t_m}{r} \frac{\partial}{\partial r}\left(r \frac{\partial w(r)}{\partial r} \right) \\
&- P_{atmos}.
\end{aligned}
\tag{2.11}
$$

The above equation can be numerically solved by non-dimensionalizing the equation and using the Galerkin Approach with six or more vibrational modes, which was found to be sufficient in prior work [25, 26]. Finally, this equation can be extended to CMUT operation in water if mutual and self-acoustic loading are incorporated. However, for the scope of this work this was not taken into account. All the variables used in this work are summarized in Appendix A, Table A.1.

2.2.1. CHARGE DISTRIBUTION

In this work, charges are injected into the charging layer by applying a bias voltage to bring the CMUT into collapse mode and by tunneling charges through the circular region where the top and bottom membranes are in contact. Consequently, the injected charges will have an axial symmetric distribution. In this work, for simplicity, the charge distribution was defined by a homogeneous distribution immediately beneath the contact area. The following equation mathematically expresses this distribution along the radius of the CMUT for the surface charge $\sigma(r)$ and volumetric charge $\rho(r)$ as:

$$\sigma(r) = \begin{cases} \sigma_0, & \text{for } 0 \le r \le r_{charge} \\ 0 & \text{for } r_{charge} < r \le a \end{cases} \tag{2.12}$$

$$\rho(r) = \begin{cases} \rho_0, & \text{for } 0 \le r \le r_{charge} \\ 0 & \text{for } r_{charge} < r \le a \end{cases} \tag{2.13}$$

where, r_{charge} is the contact radius during the charging process, a is the radius of the CMUT, σ_0 and ρ_0 are constants for the surface charge density and the volumetric charge density beneath the contact region after charging.

2.2.2. QUALITATIVE CHANGES IN THE C-V CURVE

When different types of charges are trapped inside a CMUT, the Capacitance to Voltage (C-V) curve shifts with respect to the 0 V axis. The root cause can be seen in (2.6), where there is a second term $V_{eff}(r)$ that is subtracted from the external voltage V. In the previous section it was defined that charges will be distributed only between $0 < r < r_{charge}$. Thus, for $r_{charge} > 0$, $V_{eff}(r) = 0$ from (2.7, 2.10).

In this section we qualitatively describe in which direction the C-V curve will shift depending on the charge that is distributed between $0 < r < r_{charge}$ of the CMUT. If $V_{eff}(r) > 0$, the internal voltage acts against the external voltage V, thus requiring a larger voltage to bring the CMUT into collapse, which will shift the C-V curve to the right. If $V_{eff}(r) < 0$ the internal voltage acts alongside the external voltage V shifting the C-V curve to the left. Therefore, the sign of $V_{eff}(r)$ indicates in which direction the C-V curve will shift. In this section, the following four cases are considered, and the actual charging can be considered as a combination of these four cases:

Case 1 ($\sigma_0 = 0$, $\rho_0 < 0$): Only electrons.

Case 2 ($\sigma_0 > 0$, $\rho_0 = 0$): Only downward polarization.

Case 3 ($\sigma_0 < 0$, $\rho_0 = 0$): Only upward polarization.

Case 4 ($\sigma_0 = 0$, $\rho_0 > 0$): Only holes.

Case 4 is also included in the list, yet it is unlikely that this situation will arise given that the dielectric stack is sandwiched in between two metal conductors where no injection of holes exist. Thus, we will examine the three other cases in more detail and how they will shift the C-V curve. Fig. 2.2(a) shows a cartoon drawing of how the charges are positioned in the dielectric layer for the three cases. The sign of V_{eff} is equivalent to finding the sign of σ_1 according to (2.7) and the definition of σ_1 can be found in (2.10). Since the coefficients multiplied to the $\rho(r)$ and $\sigma(r)$ are both positive, the sign of V_{eff} can be easily found for each case as, Case 1 and Case 3: $V_{eff} < 0$ (∵ $\sigma_1 < 0$)
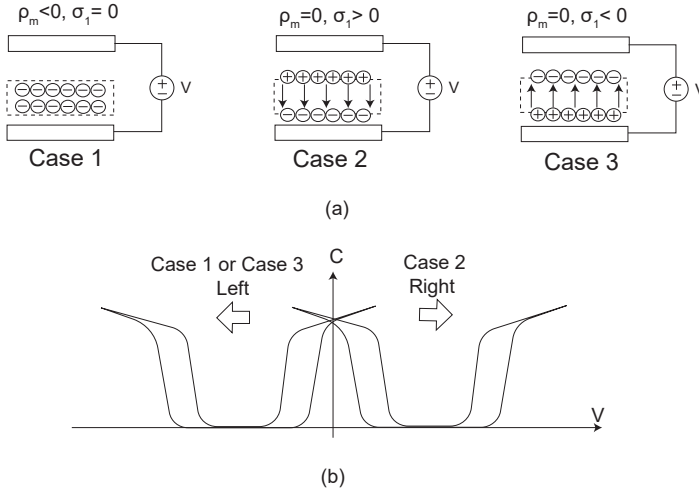
Figure 2.2.: (a) A schematic drawing of where and which polarity of charge is trapped for the three cases. (b) Shift in C-V curve: Case 1 and Case 3 the C-V curve will shift to the left; Case 2 the C-V curve will shift to the right.

and for Case 2: $V_{eff} > 0$ ($\because \sigma_1 > 0$). Thus the C-V curve will shift to the left for Case 1 and 3 and will shift to the right in Case 2 as shown in Fig. 2.2(b).

The magnitude of trapped charge is typically derived through measuring how much the C-V curve is shifted. However, if different types of charges are superimposed, this method does not work. For our work we derive the amount of trapped charge by comparing the measured C-V profile with the modelled C-V profile.

2.3. CHARACTERISATION METHODS

2.3.1. FOUR CMUT DESIGN VARIANTS AND TEST CAPACITORS

The CMUT cells used in this work have been fabricated using a standard sacrificial release processing. The transducer stack consists of a silicon wafer covered with SiO_2 for insulation, a bottom electrode insulated with a stack of ALD deposited $SiO_2/Al_2O_3/SiO_2$, a vacuum cavity created by wet etching a sacrificial layer made of Al, an ALD SiO_2, a top metal electrode covered with SiO_2, and a Si_3N_4 membrane layer on top (Fig. 2.1(c)). More information on the fabrication process of the CMUT can be found in [27].

The diameter of the CMUT membrane is 135 µm and a single CMUT element consists of 56 CMUT cells connected in parallel. Four CMUT layer stack combinations were tested to find the optimal layer stack for

	A	B	C	D	Unit	Description
t_1	0	30	50	75	nm	Insulation thickness see Fig. 2.1(c)
t_2	50	30	50	75	nm	Insulation thickness see Fig. 2.1(c)
t_3	200	240	200	250	nm	Charge layer thickness see Fig. 2.1(c)
t_4	50	10	50	50	nm	Insulation layer thickness see Fig. 2.1(c)
t_{eff}	546	544	558	474	nm	Total effective thickness (2.3)
EOT	190	190	240	300	nm	Effective oxide thickness*
t_m	2500	2500	3000	3100	nm	Total thickness of the top membrane
t_g	500	500	500	400	nm	Gap height
D	$2.4 \cdot 10^{-7}$	$2.4 \cdot 10^{-7}$	$4.1 \cdot 10^{-7}$	$4.5 \cdot 10^{-7}$	Pa·m^3	Flexural rigidity
ρ_{tp}	3290	3290	3290	3290	kg/m^3	Combined mass density of the top plate
a	67.5				μm	Plate Radius
ε_0	$8.85 \cdot 10^{-12}$				F/m	Vacuum Permittivity
ε_{SiO_2}	4.3				-	Relative Permittivity of SiO$_2$
$\varepsilon_{Al_2O_3}$	8.8				-	Relative Permittivity of Al$_2$O$_3$
P_{atmos}	$1.01325 \cdot 10^5$				Pa	Atmospheric pressure
H_{ab}, n = a, b	$2 \cdot 10^9$				Pa	Indentation hardness
σ	4				nm	Combined surface roughness standard deviation
modes	6				-	Number of vibrational modes used

* $EOT = t_1 + t_2 + t_4 + t_3 \cdot \frac{\varepsilon_{SiO_2}}{\varepsilon_{Al_2O_3}}$

Table 2.1.: Simulation parameters.

charge retention, each having slightly different thicknesses for the insulation layer, charge trapping layer, and the vacuum gap. The four variants (A, B, C, and D) used for this work are summarized in Table 2.1. Despite the similarities, a closer look at the layer stack combinations shows that these devices have many differences making a one-to-one comparison impossible. Such parameter variations are not ideal for a comparative study such as this one, however these devices were initially fabricated to understand the use of high-k materials to achieve a higher acoustic output pressure. Yet, upon their operation, these devices showed charging of the dielectric. This phenomenon was not observed for previous devices manufactured with only SiO$_2$ as the dielectric and with the same fabrication process.

In addition, to characterize the charging behavior of the CMUTs, test capacitors with an area of 200 μm × 200 μm were fabricated following the same processing steps as the CMUTs, but without depositing the sacrificial layer (Fig. 2.3(b)).

2.3.2. CHARACTERISATION METHODS FOR THE CMUTS AND TEST CAPACITORS

The test capacitors were characterized by measuring the current-voltage (I-V) curve using a Keithley 237 High Voltage Source Measure Unit. Using this instrument, first a linear voltage sweep was used to determine the breakdown voltage of a pristine test capacitor, where pristine indicates a device that has never been tested or used. The voltage was swept between 0 V and 350 V with

(a)   (b)
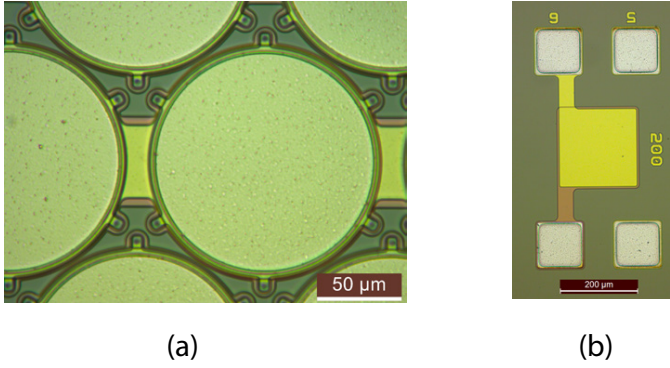
Figure 2.3.: Microscope view of (a) a CMUT cell and (b) a test capacitor.

a hold period of 1 ms at each voltage step and a compliance current of 1 mA. A second linear sweep was then applied to another pristine capacitor with the same layer stack from 0 V to slightly before the breakdown voltage, with a hold period of 1 ms and a voltage step between 0.4 V and 0.6 V, depending on the maximum voltage of the sweep and being limited by the maximum number of measurement points of the instrument.

The CMUT devices were characterized by measuring the membrane profile with a Digital Holographic Microscope (DHM) and Capacitance-Voltage (C-V) curves for charged and uncharged devices. Digital Holographic Microscopy (DHM) is a non-contact method used to characterize 3D topography, providing real-time images of the sample profile. In this work, a DHM system (LynceeTec, Switzerland) was used to characterize the membrane profile of the CMUT elements at different externally applied DC bias voltages. C-V curves were obtained with a fast C-V protocol which allows for the measurement of the pull-in and snap-out voltages of the CMUT, minimizing the alteration of the amount of stored charge. For the C-V measurement, a small AC signal at 125 MHz was superimposed on a 200 Hz triangular wave varying between 0 V and ±120 V. The change in the phase of the impedance when the CMUT goes in and out of collapse is used to draw the C-V curve. Two measurement protocols were used: a DC bipolar sweep between positive and negative voltages, and a DC unipolar sweep for either only positive or negative voltages.

2.3.3. PRE-CHARGING THE CMUTS

Pristine CMUT elements were pre-charged at room temperature using a programmable source meter (Keithley 2450). The same parameters were used for all four devices to compare their charging capabilities. Other groups that investigated pre-charged CMUTs, charged their devices with voltages between

1.5 to 2.5 times the pull-in voltage [16–20], mostly resulting, except for one case [18], in out of collapse pre-charged CMUTs. In this work, the amplitude of the DC charging voltage was chosen to be about three times higher than the analytically calculated pull-in voltage out of the four devices, in order to initiate charge trapping in a deep collapsed state. The pull-in voltage V_{pi} was calculated using the equation derived using the parallel plate theory [28]:

$$V_{pi} \simeq 0.7 \sqrt{\frac{8k \left(t_{eff} + \frac{t_m}{\varepsilon_{Si_3N_4}}\right)^3}{27\varepsilon_0 2\pi a^2}} \tag{2.14}$$

Where k is the spring constant of the device:

$$k = \frac{192\pi D}{a^2} \tag{2.15}$$

From (2.14), device C has the highest pull-in voltage, of about 58 V, therefore, a DC bias voltage of either 170 V or −170 V was chosen to pre-charge the CMUTs. The charging time was set to 300 s.

2.3.4. Fitting process overview

The fitting process was used to derive relevant parameters (i.e., σ, ρ and r_{charge}) by comparing the semi-analytical reduced order model (ROM) introduced in Section 2.2 to the measurement results. However, to avoid overfitting the ROM with all the measurement results, the ROM was sequentially tuned by feeding it with limited information and checking it against the measurement results.

The fitting process of the ROM to the measurement result is as follows. First, the ROM is implemented in MATLAB with the membrane dynamics equation (2.11), layer stack, membrane geometry, and gap height. Secondly, using the membrane profile measured at 0 V, the uniform biaxial residual stress τ is tuned so that the membrane profile matches the measurement result. This serves as the baseline model of the CMUT with no charging. Then, the pull-in and snap-out voltages are predicted with the ROM and compared to the fast C-V curve measurements (2.5). Furthermore, the collapse diameter and C-V curve are compared with the measurement results to determine the surface charge and the volume charge.

2.4. CHARACTERISATION RESULTS

2.4.1. I-V MEASUREMENTS

The result of the I-V measurement on the capacitor variant A is shown in Fig. 2.4(a). For variants B to D, the results can be found in the supplementary Fig. A.1. In addition, the measurement that was made on a reference capacitor with only SiO_2 as the dielectric material (EOT = 200 nm) is shown in Fig. 2.4(b). In both 2.4(a) and (b), a small leakage current of several nA/cm^2, independent of the electric field, is observed up to 4 to 5 MV/cm and, above this value, the current density gradually increases until around 7-8 MV/cm. When the electrical field is further increased above 7 to 8 MV/cm, the dielectric of the capacitor with only SiO_2 breaks down, as shown by the dashed line in Fig. 2.4(b). On the other hand, the current in the capacitors with the Al_2O_3 layer sharply rises (shaded region in Fig. 2.4(a)) before the hard breakdown, which occurs at electric fields in the order of 10-12 MV/cm. The shaded region indicates fast charging and is not present in the capacitor with only SiO_2 as dielectric. In the past, CMUTs with only SiO_2 as dielectric did not show noticeable charging. Therefore, we can infer that in order to trap charge, the material should show a region of fast charging. In addition, comparing the voltage used to charge the different CMUT variants, only for devices A to C the voltage lies in the shaded region. The effect of this difference on the amount of trapped charge will be discussed in Section 2.4.3.
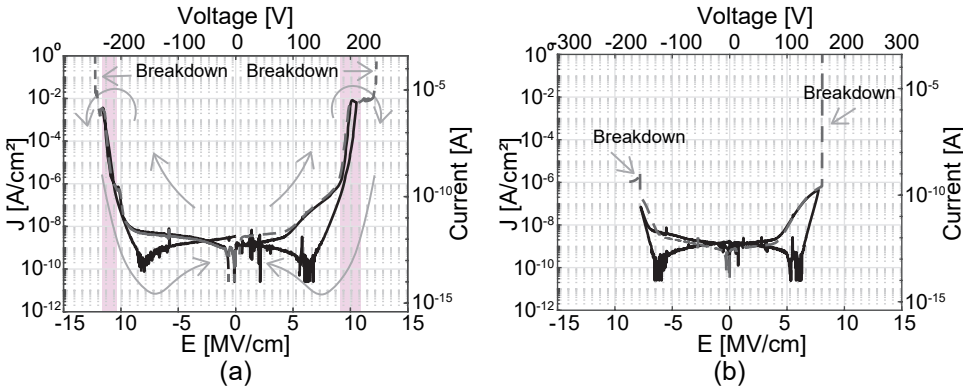
Figure 2.4.: Example of I-V curves measured on the test capacitors. (a) layer stack A and (b) reference capacitor without Al_2O_3 layer. Left and bottom axes indicate the current density at a specific electric field, while the top and right axes indicate the voltage that needs to be applied to obtain the corresponding electric field. Direction arrows in a) indicate the direction of the voltage sweep and dashed lines indicate the measurement done to determine the breakdown voltage. Pink shaded area indicates the region of fast charging.

2.4.2. Fitting the model with DHM measurements

Fig. 2.5(a) shows the membrane profile of variant A when the bias voltage was swept from 0 V to 120 V on a pristine CMUT device. From this figure, it can be seen that variant A has a pull-in voltage between 30 V to 40 V. The DHM measurements for variants B to D can be found in supplementary Fig. A.2. In Fig. 2.5(a), the initial displacement at 0 V is caused by the atmospheric pressure and the uniform biaxial residual stress that was modeled in Section 2.2.

In this section, the measurements and the simulation of the membrane profile at 0 V was compared for each variant to tune uniform biaxial residual stress parameter (τ). In Fig. 2.5(b) the dashed line shows the membrane profile at 0 V for all variants. For devices A and B, the center displacement of the membrane is about 200 nm, while for devices C and D, it is in the order of 100 nm. The τ is tuned such that the simulated membrane profile (solid line) matches the four variants (dashed line) as much as possible. The tuning process resulted in a negative stress in the order of several hundred of MPa
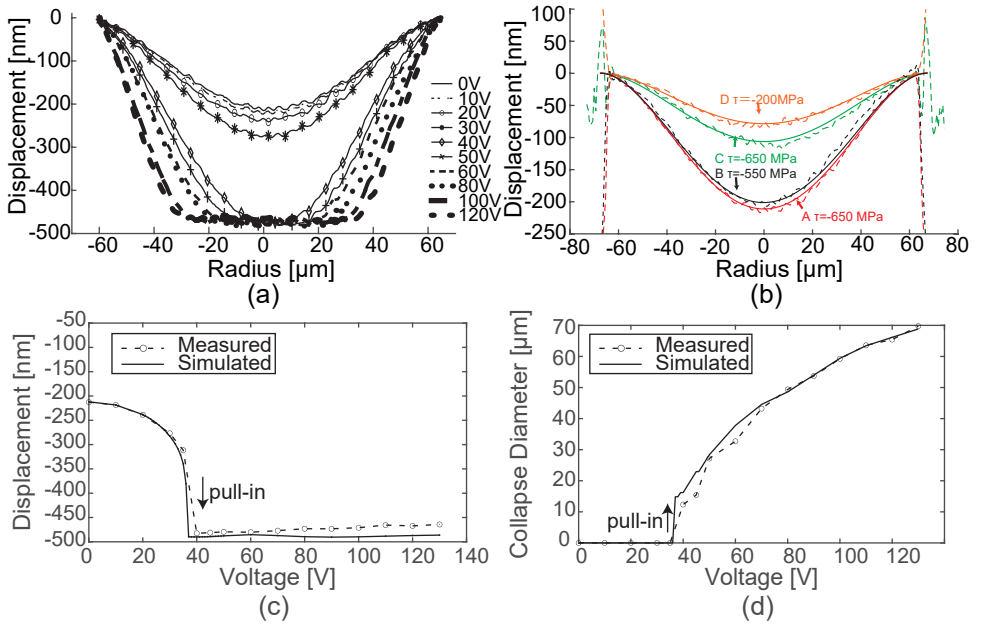
Figure 2.5.: (a) Measurement result of the membrane profile for variant A. (b) Tuning result of the membrane profile after fitting. The dashed line is the simulation result and the measurement result is in the solid line. Comparison of the simulation result and the measurement result for variant A regarding the (c) center displacement and the (d) collapse diameter.

(i.e. A:−650 MPa, B:−550 MPa, C:−650 MPa, D:−200 MPa). These values are large and cannot be fully explained by the stress resulting from the fabrication. Thus, it should be recognized that this stress value is also compensating for the subtle non-idealities within the model. Such non-idealites can arise from the existence of the six plugging areas around the CMUT cell which will have some repercussions on the axisymmetric assumption of the model or the perfectly clamped assumption along the rim of the CMUT membrane.

After the tuning process, it can be seen that the measurement results and the simulation results are in good agreement. Fig. 2.5(c) and (d) is a comparison between the simulation result and the measurement result for variant A regarding the center displacement and the collapse diameter when different external voltages are applied. The comparison of the simulation results and the measurement results for the other CMUT variants can be found in supplementary Fig. A.4 and Fig. A.3.

2.4.3. FAST C-V MEASUREMENT

After being charged, the C-V curve of the CMUTs was measured. A unipolar sweeping protocol was used to keep the same polarity while charging and measuring. In addition, a bipolar sweep was done on a pristine device as a reference. In Fig. 2.6, the fast C-V measurement results are shown for the four variants. The solid blue line is the C-V curve of a pristine element, obtained with a bipolar sweep, which is symmetric with respect to 0 V for all the devices. The solid pink line represents the positive unipolar sweep, while the solid black line represents the negative unipolar sweep for a CMUT element charged with positive and negative polarity, respectively. In Fig. 2.6, devices A and B show the most significant shifts in the C-V curves with respect to the uncharged element. The C-V curves for A and B show that the CMUT elements are in collapse at 0 V bias and that around 40 V must be applied to bring them out of collapse. On the other hand, Fig. 2.6(c-d) shows that the amount of charge stored in devices C and D, which is proportional to the shift in the C-V curve, is not sufficient to keep the device in collapse. Since their thicker membrane and effective dielectric thickness require a larger voltage to bring the membrane into collapse, a higher amount of charge, compared to devices A and B, must be stored to keep the membrane in collapse.

As mentioned earlier, the C-V curve can shift either to the left or to the right with respect to the symmetrical reference curve, depending on the type of charge. However, assuming that no injection of holes can occur in the Al_2O_3 layer, the only possible explanation for the shift of the C-V curve to the right is that there is a downward polarization. Thus, these results indicate the polarization behavior of the Al_2O_3 layer. Ferroelectric-like behavior such as

2

this was reported by Peng et al. [29], who associated this effect with oxygen vacancies that move due to the external electric field. Additionally, the shift of the C-V curve to the left or to the right is nearly the same for all CMUTs. This shows that the polarization behavior of the Al_2O_3 layer is dominant compared to the fixed volume electron charges, which tend to pull the C-V curve only to the left. Thus, in the consecutive process of fitting the C-V curve, only the polarization is taken into account, and the fixed volume charges are ignored by setting $\rho_m = 0\,C/m^2$.

Fig. 2.6 also shows the simulated C-V curve for all variants with a dashed line on top of the corresponding measurement result. The value of the capacitance is simulated from the membrane profile and does not include the membrane's transient movement, which is typically referred to as mechanical capacitance. In addition, the collapse radius at 170V is simulated and used for the charge radius in each variant (i.e., for A and B: $r_{charge} = 40\,\mu m$ and for C and D: $r_{charge} = 32\,\mu m$. Then, the polarizing surface charge σ is tuned either
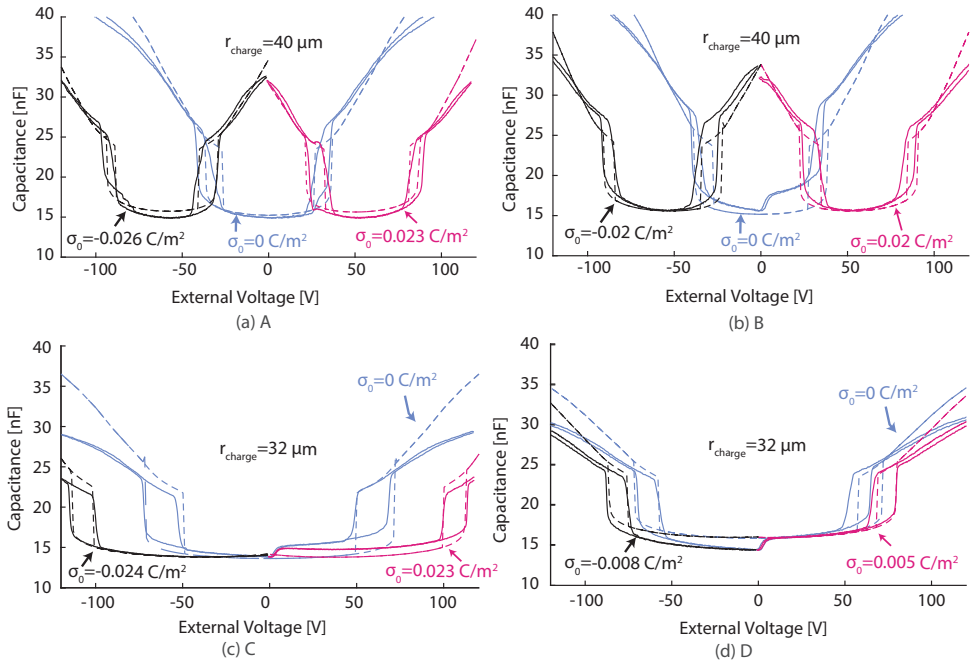
Figure 2.6.: C-V curves of the four CMUT devices. Solid lines represent the measured values, while dashed lines represent the value fitted with the model. The blue line is the bipolar sweep done on a pristine device, the pink line is the positive unipolar sweep for a device positively charged and the black line is the negative unipolar sweep for a device negatively charged. (a) device A, (b) device B, (c) device C, (d) device D.

to the positive or to the negative to fit the measured C-V curve. The required surface charge for each variant is also shown in Fig. 2.6. For A, B, and C, the amount of charge is nearly $0.02 \, C/m^2$, while for D, is significantly lower, approximately $0.0052 \, C/m^2$. This is because, during the charging process of device D, the electrical field across the device was lower due to the thicker insulation layer between the top and bottom electrodes. In addition, the voltage used to charge device D does not lie in the region of fast charging and polarization (Fig. 2.4), while this is the case for the other types of devices. This suggests that, in order to trap enough charge to obtain a collapse-mode device, the charging voltage should be chosen among that region, which, for the devices used in this work, corresponds to electric fields above 7-8 MV/cm. However, care should be taken to not choose a voltage too high to cause breakdown of the dielectric. The amount of trapped charge is similar to the maximum charge density that has been reported in literature [30, 31] $0.016 \, C/m^2$. From this analysis, devices A and B are both good candidates for the pre-charged collapse mode CMUT because they both remained in collapse after the charging process. In addition, because device A charged slightly more than device B, the following experiments focus on device A.

2.5. PERFORMANCE RESULTS

2.5.1. TRANSMIT SENSITIVITY

The bandwidth of the pre-charged collapse-mode CMUT (device A) was measured with an impulse response measurement in water and compared to a pristine CMUT with an external bias voltage. The measurement was conducted with 6 elements in parallel, each consisting of a row of 56 CMUT cells in parallel, accounting for a total width and height of the device of 0.84 mm and 7.56 mm respectively. The CMUT was pre-charged with a positive voltage of 170 V for several minutes. Then the device was immersed in water and an impulse signal with an amplitude of $-25 \, V$ and a pulse width of 25 ns was applied. The acoustic response was measured with a fiber optic hydrophone (Precision Acoustic, UK) at 2.6 mm distance from the CMUT. Then the same experiment was repeated with a CMUT without stored charge. In this case, a bias voltage was externally applied from 60 V to 100 V in 10 V steps and the polarity of the impulse signal was flipped (i.e. positive impulse signal). The range of bias voltages used for this experiment is below the rapid charging state measured in Section 2.4-2.4.1 and thus, the CMUT will not charge significantly, and a fair comparison can be made between a CMUT with and without charge. The result of the impulse response for all bias voltages can be seen in supplementary Fig. A.5.
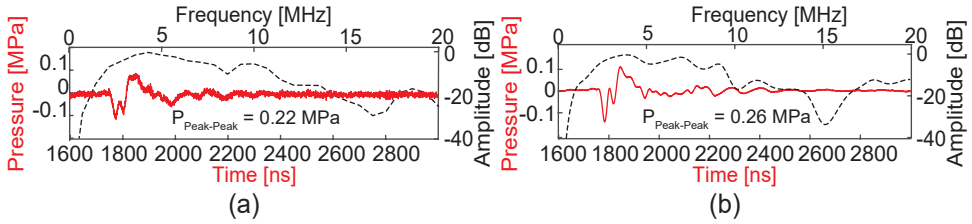
Figure 2.7.: Transient pressure response (red) and frequency response (dashed line) measured with a hydrophone at 2.6 mm distance for (a) a CMUT charged with 170 V for several minutes. Impulse signal had a 25 V amplitude, with negative polarity and pulse width of 25 ns at full width half maximum; (b) a CMUT externally biased with 70 V. Impulse signal had a 25 V amplitude with positive polarity and a pulse width of 25 ns at full width half maximum.

The result of the impulse response for the pre-charged CMUT is shown in Fig. 2.7(a). The peak-to-peak pressure was 0.22 MPa and the −6 dB bandwidth was 113 % with a center frequency of 5.1 MHz. The transmit sensitivity was 8.8 kPa/V. In comparison, the impulse response for the CMUT with an external bias voltage of 70 V is shown in Fig. 2.7(b). The peak-to-peak pressure was 0.26 MPa and the −6 dB bandwidth was 117 % with a center frequency of 5.0 MHz. The transmit sensitivity was 10.4 kPa/V. Thus, the acoustic performance of the pre-charged collapse-mode CMUT is nearly identical to a CMUT biased with 70 V.

2.5.2. RECEIVE SENSITIVITY

The receive sensitivity was measured by sending an ultrasound signal from a source and receiving it with the pre-charged collapse-mode CMUT. The schematic of the experimental setup is shown in Fig. 2.8(a) and a picture of the setup is shown in Fig. 2.8(b). In this experiment, ultrasound was generated by a transmitter (TX) CMUT (5 mm × 12 mm) with a frequency of 2 MHz generating a peak to peak pressure up to 0.6 MPa immediately in front of the receiver (RX) pre-charged CMUT. The RX had 8 CMUT elements in parallel, each consisting of a row of 56 CMUT cells in parallel, which resulted in a surface area of 7.56 mm × 0.95 mm. The distance between the TX and RX was 6 cm which was chosen such that the ultrasound hits the pre-charged collapse-mode CMUT array with a plane wave. This guarantees that all the CMUT cells operate in-phase, with the same voltage. To avoid standing wave formation between the TX and the RX, the ultrasound was sent in 10 cycles at 1 kHz pulse repetition frequency. Prior to the experiment, the electrical capacitance of the CMUT was measured to be 640 pF. The output of RX was connected to an adjustable impedance matching block on the same PCB as
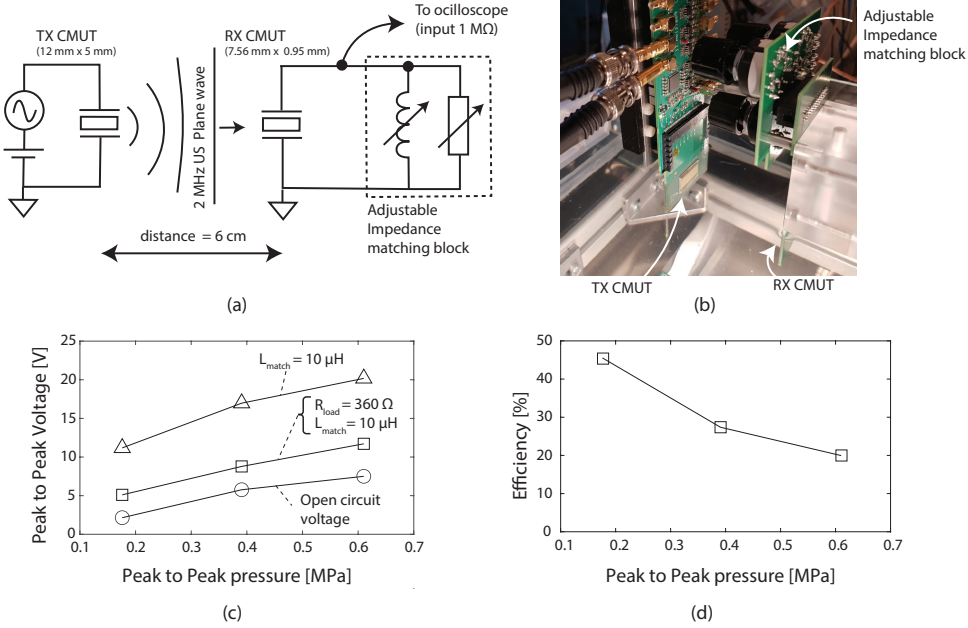
Figure 2.8.: Power transfer experiments. (a) Schematic diagram of the setup (b) Picture of the experimental setup. (c) Output voltage measured at the receiver for varying loading conditions and (d) efficiency measured for matched load condition ($R_{load} = 360\,\Omega$ and $L_{match} = 10\,\mu H$). Both figures are plotted with respect to the incident peak to peak pressure.

shown in Fig. 2.8(a). This block is composed of several inductors and resistors that can be manually connected with mechanical switches to compensate the electrical capacitance of the CMUT. The alignment of RX with respect to TX was adjusted by positioning the RX such that the maximum output voltage was achieved in an open circuit condition.

First, the output voltage was measured at the RX in open circuit condition for three different incident pressure values (Fig. 2.8(c) the line with circle markers). Then the inductive load was tuned to maximize the output voltage in order to compensate the electrical capacitance in the CMUT (Fig. 2.8(c) the line with triangle markers). This matched condition occurred at $10\,\mu H$ which is in good agreement with the analytically calculated value of $L_{match} = 9.89\,\mu H$, according to $L_{match} = \dfrac{1}{(2\pi f_{res})^2 \cdot C_e}$ ($\because C_e = 640$ pF, $f_{res} = 2$ MHz). Finally, the matching resistor load was adjusted to $R_{load} = 360\,\Omega$ to achieve maximum power transfer (Fig. 2.8(c) the line with square markers). In this matched condition, the efficiency of the CMUT, defined from the plane immediately in front of the RX CMUT to the resistive load, was calculated for the three

pressure values as shown in Fig. 2.8(d). From this figure, it can be seen that the efficiency at 0.18 MPa peak to peak is 45 % and decreases to 20 % at 0.6 MPa peak to peak due to non-linear effects. By linearly fitting the points in Fig. 2.8(c) the open circuit receive sensitivity is computed resulting in 13.1 V/MPa. The maximum power instantaneously harvested at the load was 47 mW when 0.6 MPa peak to peak pressure was applied. The coupling coefficient kt^2 of the pre-charged collapse-mode CMUT was also calculated for a few pre-charged samples, resulting in about 0.7. In the supplementary Table A.2, this result is compared to the results achieved by other groups, showing that its performance is comparable to PZT. In addition, the transmit sensitivity of our pre-charged collapse-mode CMUTs is in line with the characteristic values of other micromachined transducer technologies [9], and in terms of receive sensitivity the performance is in the top range or above other technologies.

2.5.3. RELATIONSHIP BETWEEN CHARGING PARAMETERS AND STORED CHARGE

With the objective to charge the CMUT as much as possible, several combinations of charging parameters (i.e., charging time, temperature, voltage, and polarity) have been investigated. The resonance frequency extracted from the air-coupled impedance measurement of a collapse-mode CMUT was used as a representative parameter indicating to what extent the CMUT was charged [25, 32]. Furthermore, the fast C-V curve measurement was not used because it was not sensitive enough to detect the subtle changes caused by the different charging parameters that were tested. The tested charging times were between 60 s and 600 s and the temperature of the sample during charging was varied between 20°C and 150°C. Two charging voltages were tested which were 170 V and 200 V, both with a positive and negative polarity.

Fig. 2.9 shows the results of the experiment. In this figure, a plane was fitted to the experimental results for each voltage and polarity, showing that a higher resonance frequency, therefore more charge, is stored by applying the charging voltage to the CMUT for a longer time and at a higher temperature. The increase in the amount of stored charge at higher temperatures is a known phenomenon in the field of device reliability [33–35]. The charging current is a thermally activated phenomenon, and combined with the decrease of the spring constant at elevated temperature, results in the acceleration of the charging process [36]. In addition, comparing the effect of the charging polarity for the same charging voltage, using a negative polarity results in a higher resonance frequency. This is because the effect of surface charge, which
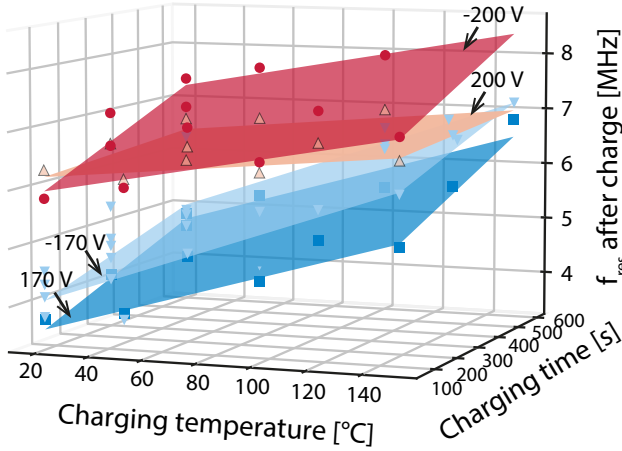
Figure 2.9.: Effect of different charging parameters on the after charging resonance frequency of the CMUT device with layer stack A.

is the dominating mechanism, is combined with the effect of the volume charges, while for the positive polarity, the effect of the surface charges is attenuated by the opposing effect of the volume charges, as qualitatively explained in Section 2.2.2. Furthermore, charging the device for a longer time results in a higher amount of charge stored in the device. To summarize, charging the device for a longer time, at a higher temperature, at a higher voltage, with a negative polarity result in a higher amount of stored charge. These relationships can be used to achieve faster and more efficient charging of the CMUTs.

2.5.4. LIFETIME ESTIMATION

In the prospect of the commercialization of the device, it is important to know how long the trapped charges are retained in the charging layer. To estimate the lifetime of the devices at different operating temperatures, Accelerated Lifetime Tests (ALT) have been performed on devices of type A with temperature as an accelerating factor. The failure time of the CMUTs can be fitted with the Arrhenius relation:

$$\text{lifetime}(T) = A \cdot \exp\left(\frac{E_A}{k_B \cdot T}\right) \tag{2.16}$$

where E_A is the activation energy of the discharge process and k_B is the Boltzmann's constant 8.617×10^{-5} eV/K. A is a constant that depends on the

device geometry, size, test method and other factors, and can be estimated from the test data. Pristine CMUTs were charged with several combinations of parameters and after charging they were brought at the designated test temperature. Most of the devices were charged at room temperature, while a few tests were performed on devices charged at higher temperatures to confirm the result that are shown in Fig. 2.9. The test temperatures were between 100 °C and 150 °C, and the failure time of the devices was evaluated measuring the impedance at constant time intervals. The impedance spectrum of an air-coupled CMUT after charging shows a resonance peak at around 6 MHz (high frequency), which indicates that the CMUT cells are in collapse (Fig. 2.10). When the membrane of some of the CMUTs cells goes out of collapse, the equivalent capacitance of the device decreases (impedance spectrum shifts upwards), and a second resonance peak appears at a much lower frequency, at around 1.5 MHz, which corresponds to the non-collapse mode of operation of the CMUT. When a cell of a pre-charged CMUT goes out of collapse, it is defined as failed because it cannot harvest ultrasound power in this state. The height of the resonance peaks at both high and low frequency changes over time due to the discharging and subsequent going out of collapse of the CMUT cells. During some of the lifetime tests, the shape
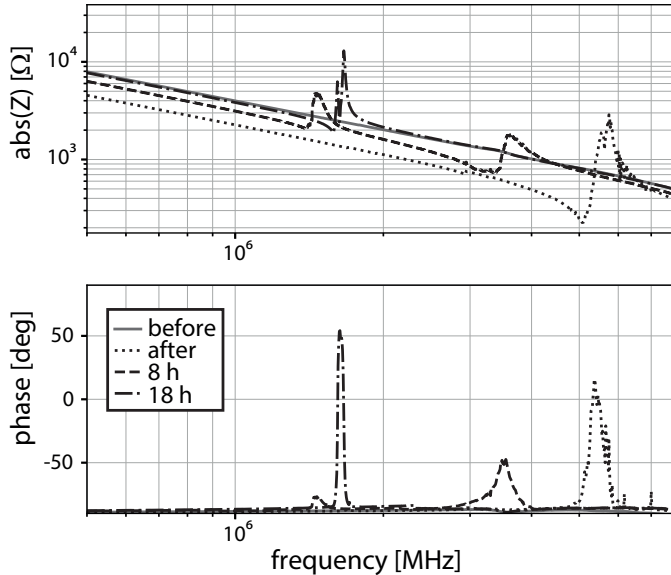
Figure 2.10.: Example of air-coupled impedance spectrum of a CMUT device type A, measured at different points in time during ALT at high temperature. Only a few measured points are reported here for clarity.
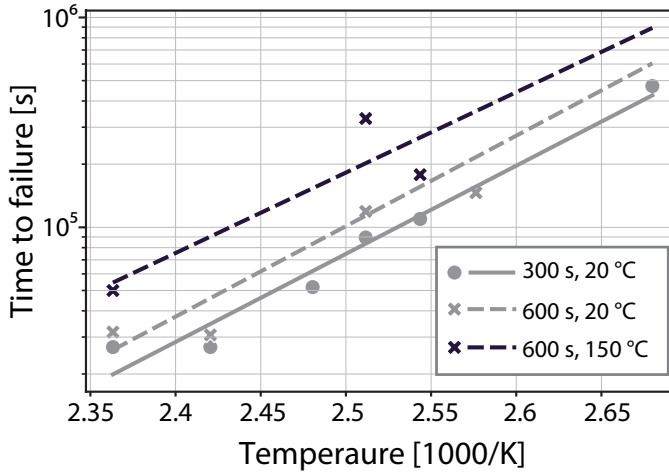
Figure 2.11.: Fitting of the ALT results with the Arrhenius relation to predict lifetime of the devices charged at different temperatures.

of the cells in the element under test was examined with the DHM, and we observed that the height of the two peaks in the phase plot of the impedance spectrum (bottom plot of Fig. 2.10) correlates to the number of CMUT cells in collapse and non-collapse. The point in time at which the height of the peak at the lower frequency is larger than the height of the peak at high frequency is when more than half of the CMUT cells are out of collapse, which is defined as the failure time of the device.

In Fig. 2.11, the failure times obtained from some preliminary ALT tests have been fitted with the Arrhenius relation (2.16). The results show that the lifetime of the devices increases when they are charged for a longer time and, extrapolating the lifetime at lower temperatures, at the minimum they have a lifetime of more than 2.5 years at body temperature (37°C). In addition, the lifetime of a few samples charged at 150°C showed an increase of about 50% compared to devices charged at room temperature. Therefore, these results confirm that charging the CMUTs at higher temperature and for a longer time increases the lifetime. Although the ALT conditions used in this work may have accelerated the failure mechanisms as they occur in actual operation conditions, and more results are necessary to fully assess their lifetime, these results show the potential of these devices for a variety of applications, including in-body ultrasound power transfer and harvesting.

2.6. CONCLUSION

In this paper, pre-charged collapse-mode CMUTs were studied through modeling and characterization of four device variants (A, B, C and D) with an Al_2O_3 layer between the top and bottom electrodes. To study their charging behavior, a semi-analytic reduced order model was developed following the approach of [23]. The model includes the built-in charging layer as an additional force term.

The charging behavior was first characterized in detail using I-V curves of test capacitors, that have the same layer stack as the CMUT, but without the vacuum gap. These I-V curves showed a region of fast charging and polarization before the hard breakdown, that was not present in the reference capacitor that only had SiO_2 as the dielectric material, thus indicating that charges are trapped within the CMUT because of the Al_2O_3 layer. In addition, it was found that to obtain pre-charged collapse-mode CMUTs the charging voltage needs to be in the range of values in the region of fast charging and polarization.

By fitting this model to the fast C-V curve measurement of the pre-charged collapse-mode CMUTs, it was shown that the Al_2O_3 layer has a polarizable behavior that can be controlled by the polarity of the charging voltage. Moreover, the amount of charge stored in each of the CMUT variant can be calculated from the model, resulting in a maximum surface charge density of $\sigma_0 = 0.026 \, C/m^2$ for variant A.

This device was then characterized with transmit and receive sensitivity measurements in water, showing a performance in line with biased CMUTs, with bandwidth and efficiency of the power harvesting were in line with values obtained by other groups. Finally, the amount of stored charge was maximized for variant A by testing additional charging parameters. It was found that charging the CMUTs at a higher temperature, for a longer time and with a higher voltage resulted in a larger amount of trapped charge. These CMUTs also showed a charge retention of 2.5 years at body temperature, making these devices promising candidates for applications requiring, among others, biocompatibility and manufacturing scalability.

REFERENCES

[1] M. Saccher[*], S. Kawasaki[*], J. H. Klootwijk, R. Van Schaijk, and R. Dekker. "Modeling and Characterization of Pre-Charged Collapse-Mode CMUTs". In: *IEEE Open Journal of Ultrasonics, Ferroelectrics, and Frequency Control* 3 (2023), 14–28. *These authors should be ragarded as joint first author.

[2] T. L. Szabo. *Diagnostic ultrasound imaging : inside out*. Elsevier Academic Press, 2004.

[3]   J. Joseph, B. Ma, and B. T. Khuri-Yakub. "Applications of Capacitive Micromachined Ultrasonic Transducers: A Comprehensive Review". In: *IEEE Transactions on Ultrasonics, Ferroelectrics, and Frequency Control* 69.2 (2022), pp. 456–467.

[4]   D. M. Becker, C. A. Tafoya, S. L. Becker, G. H. Kruger, M. J. Tafoya, and T. K. Becker. "The use of portable ultrasound devices in low- and middle-income countries: a systematic review of the literature". In: *Tropical Medicine & International Health* 21.3 (Jan. 2016), pp. 294–311.

[5]   Y. Baribeau, A. Sharkey, O. Chaudhary, S. Krumm, H. Fatima, F. Mahmood, and R. Matyal. "Handheld Point-of-Care Ultrasound Probes: The New Generation of POCUS". In: *Journal of Cardiothoracic and Vascular Anesthesia* 34.11 (Nov. 2020), pp. 3139–3145.

[6]   D. K. Piech *et al.* "A wireless millimetre-scale implantable neural stimulator with ultrasonically powered bidirectional communication". In: *Nature Biomedical Engineering* 4.2 (2020), pp. 207–222.

[7]   G. L. Barbruni, P. M. Ros, D. Demarchi, S. Carrara, and D. Ghezzi. "Miniaturised Wireless Power Transfer Systems for Neurostimulation: A Review". In: *IEEE Transactions on Biomedical Circuits and Systems* 14.6 (Dec. 2020), pp. 1160–1178.

[8]   S. Kawasaki, Y. Westhoek, I. Subramaniam, M. Saccher, and R. Dekker. "Pre-charged collapse-mode capacitive micromachined ultrasonic transducer (CMUT) for broadband ultrasound power transfer". In: *2021 IEEE Wireless Power Transfer Conference (WPTC)*. IEEE.

[9]   Health.E Lighthouse. *A European MEMS Ultrasound Benchmark [White Paper]*. Tech. rep. Nov. 2021. URL: https://www.s2e2.fr/wp-content/uploads/2022/03/CMUT-PMUT-Benchmark-Technical-Whitepaper.pdf.

[10]   H. Martinussen, A. Aksnes, and H. E. Engan. "Investigation of charge diffusion in CMUTs using optical interferometry". In: *2008 IEEE Ultrasonics Symposium*. IEEE, Nov. 2008.

[11]   K. Midtbo and A. Ronnekleiv. "Analysis of charge effects in high frequency CMUTs". In: *2008 IEEE Ultrasonics Symposium*. IEEE, Nov. 2008.

[12]   L. L. P. Wong, S. Na, A. I. H. Chen, and J. T. W. Yeow. "A novel method for measuring dielectric charging of CMUT arrays". In: *2014 IEEE International Ultrasonics Symposium*. 2014, pp. 185–188.

[13]   J. A. Kittl *et al.* "High-k dielectrics for future generation memory devices (Invited Paper)". In: *Microelectronic Engineering* 86.7 (2009), pp. 1789–1795.

[14]   W. Xu and Y. Ni. "Memory characteristics and mechanisms in transistor-based memories". In: Elsevier, 2020, pp. 53–73.

[15]   C. Zhao, C. Zhao, S. Taylor, and P. Chalker. "Review on Non-Volatile Memory with High-k Dielectrics: Flash for Generation Beyond 32 nm". In: *Materials* 7.7 (2014), pp. 5117–5145.

[16]   W. Y. Choi, C. H. Lee, Y. H. Kim, and K. K. Park. "Comparison of Si_3N_4–SiO_2 and SiO_2 Insulation Layer for Zero-Bias CMUT Operation Using Dielectric Charging Effects". In: *IEEE Transactions on Ultrasonics, Ferroelectrics, and Frequency Control* 67.4 (2020), pp. 879–882.

[17] F.-Y. Lin, W.-C. Tian, and P.-C. Li. "CMOS-based Capacitive Micromachined Ultrasonic Transducers operating without external DC bias". In: *2013 IEEE International Ultrasonics Symposium (IUS)*. IEEE, July 2013.

[18] M.-C. Ho, M. Kupnik, K. K. Park, and B. T. Khuri-Yakub. "Long-term measurement results of pre-charged CMUTs with zero external bias operation". In: *2012 IEEE International Ultrasonics Symposium*. IEEE, Oct. 2012.

[19] K. K. Park, M. Kupnik, H. J. Lee, O. Oralkan, and B. T. Khuri-Yakub. "Zero-bias resonant sensor with an oxide-nitride layer as charge trap". In: *2010 IEEE Sensors*. IEEE, Nov. 2010.

[20] A. Kshirsagar, A. Sampaleanu, R. Chee, W. Moussa, and R. J. Zemp. "Pre-charged CMUTs with efficient low-bias voltage operation for medical applications". In: *2013 IEEE International Ultrasonics Symposium (IUS)*. IEEE, 2013.

[21] G. D. Wilk, R. M. Wallace, and J. M. Anthony. "High-k gate dielectrics: Current status and materials properties considerations". In: *Journal of Applied Physics* 89.10 (2001), pp. 5243–5275.

[22] H. Koymen, A. Atalar, S. Guler, I. Koymen, A. S. Tasdelen, and A. Unlugedik. "Unbiased Charged Circular CMUT Microphone: Lumped-Element Modeling and Performance". In: *IEEE Transactions on Ultrasonics, Ferroelectrics, and Frequency Control* 65.1 (2018), pp. 60–71.

[23] M. Pekař, S. H. M. Van Nispen, R. H. B. Fey, S. Shulepov, N. Mihajlović, and H. Nijmeijer. "A fluid-coupled transmitting CMUT operated in collapse mode: Semi-analytic modeling and experiments". In: *Sensors and Actuators A: Physical* 267 (2017), pp. 474–484.

[24] G. M. Sessler. "Spatial depth and density of charge in electrets". In: *Journal of Applied Physics* 43.2 (1972), pp. 408–411.

[25] M. Pekař, W. U. Dittmer, N. Mihajlović, G. Van Soest, and N. De Jong. "Frequency Tuning of Collapse-Mode Capacitive Micromachined Ultrasonic Transducer". In: *Ultrasonics* 74 (2017), pp. 144–152.

[26] G. W. Vogl and A. H. Nayfeh. "A reduced-order model for electrically actuated clamped circular plates". In: *Journal of Micromechanics and Microengineering* 15.4 (2005), pp. 684–690.

[27] J. H. Klootwijk, P. Dirksen, M. Mulder, and E. M. L. Moonen. "Capacitive micromachine ultrasound transducer". Patent US9132693B2. 2015.

[28] S. Olcum, M. N. Senlik, and A. Atalar. "Optimization of the gain-bandwidth product of capacitive micromachined ultrasonic transducers". In: *IEEE Transactions on Ultrasonics, Ferroelectrics and Frequency Control* 52.12 (2005), pp. 2211–2219.

[29] Y. Peng *et al.* "Ferroelectric-like Behavior Originating from Oxygen Vacancy Dipoles in Amorphous Film for Non-volatile Memory". In: *Nanoscale Research Letters* 15.1 (2020).

[30] J. J. H. Gielis, B. Hoex, M. C. M. Van De Sanden, and W. M. M. Kessels. "Negative charge and charging dynamics in Al_2O_3 films on Si characterized by second-harmonic generation". In: *Journal of Applied Physics* 104.7 (2008), p. 073701.

[31] X. Zhang, B.-W. Liu, Y. Zhao, C.-B. Li, and Y. Xia. "Influence of annealing temperature on passivation performance of thermal atomic layer deposition Al_2O_3 films". In: *Chinese Physics B* 22.12 (2013), p. 127303.

[32]   O. Oralkan, B. Bayram, G. G. Yaralioglu, A. S. Ergun, M. Kupnik, D. T. Yeh, I. O. Wygant, and B. T. Khuri-Yakub. "Experimental characterization of collapse-mode CMUT operation". In: *IEEE Transactions on Ultrasonics, Ferroelectrics and Frequency Control* 53.8 (2006), pp. 1513–1523.

[33]   N. Tavassolian, M. Koutsoureli, E. Papandreou, G. Papaioannou, B. Lacroix, Z. Liu, and J. Papapolymerou. "The Effect of Silicon Nitride Stoichiometry on Charging Mechanisms in RF-MEMS Capacitive Switches". In: *IEEE Transactions on Microwave Theory and Techniques* 57.12 (2009), pp. 3518–3524.

[34]   R. Daigler, G. Papaioannou, E. Papandreou, and J. Papapolymerou. "Effect of dielectric film thickness on dielectric charging of RF MEMS capacitive switches". In: *2008 IEEE MTT-S International Microwave Symposium Digest*. IEEE, 2008.

[35]   R. Daigler, E. Papandre, N. Tavassolian, M. Koutsoureli, G. Papaioannou, and I. Papapolymerou. "Dependence of dielectric charging on film thickness and deposition conditions". In: *2008 Asia-Pacific Microwave Conference*. IEEE, 2008.

[36]   X. Yuan, Z. Peng, J. C. M. Hwang, D. Forehand, and C. L. Goldsmith. "Acceleration of Dielectric Charging in RF MEMS Capacitive Switches". In: *IEEE Transactions on Device and Materials Reliability* 6.4 (2006), pp. 556–563.

2

3

MIM CAPACITORS FOR NEXT-GEN CMUTS DIELECTRIC

3.1. INTRODUCTION

In the previous chapter, pre-charged collapse-mode CMUTs with a charge storage layer were modelled and characterised, showing a good performance. In the context of the European project Moore4Medical [1], a new batch of pre-chargeable collapse-mode CMUT devices was planned for fabrication. The design of the dielectric stack of the second generation devices had to include a charge storage layer and have a similar EOT as the standard CMUTs devices normally fabricated at Philips. In this way, the other design parameters did not need to be changed, therefore not requiring a redesign.

Two main requirements were considered for the charge storage layer: it should store as much charge as possible, and the charge retention should be as long as possible. In addition, the material had to be available for deposition in the Philips cleanroom. Therefore, two materials were chosen: ALD Al_2O_3, already used in the devices presented in Chapter 2, and PECVD Si_3N_4. Both are high-k materials, known to have a high density of trap states due to their stoichiometry [2]. Other possible alternatives would have been HfO_2 or Ta_2O_5. Depending on the material, different charging mechanisms due to different numbers of ionic bonds, dipoles, and space charges influence the charging process, resulting in different amount of stored charge [3].

To evaluate the dielectric charging and discharging in CMUTs devices, Metal Insulator Metal (MIM) capacitors were used by other groups [4]. They are easy to fabricate and resemble the pull-in state of CMUT devices. Although the results obtained from these structures cannot be directly used for the collapse-mode CMUTs, they can highlight differences between materials or structures. An important difference between MIM and collapse-mode CMUTs

is that in MIM structures there is a perfect contact between the different dielectric layers, while in the collapsed area of CMUTs, air gaps are present due to the roughness of the surfaces introduced in the fabrication process.

The goal of this chapter is to investigate the charging and discharging of MIM capacitors with an ALD Al_2O_3 or PECVD Si_3N_4 charge storage layer embedded in the dielectric to highlight the differences between the two materials and between dielectric stack combinations. The aim is to use the results from these experiments as a starting point for the design of the dielectric stack for the second generation pre-chargeable CMUT devices planned for fabrication.

3.2. MIM CAPACITORS FABRICATION

MIM capacitors were fabricated with the same process flow as the CMUTs, such that their dielectric is as similar as possible to the future CMUT devices. The only difference was the sacrificial metal layer, which was not deposited and etched, therefore the vacuum gap is not present. The MIM capacitors dielectric stack is composed of a layer of SiO_2, in contact with the bottom electrode, followed by the charge storage layer (Si_3N_4 or Al_2O_3), and by another layer of SiO_2, in contact with the top electrode. The Si_3N_4 and SiO_2 were PECVD deposited, while Al_2O_3 was ALD deposited. The MIM capacitors process flow can be found in Appendix B.

Symmetrical and asymmetrical stacks were designed and fabricated with different thicknesses of the top and bottom SiO_2 layer, to understand its role in the charging and discharging process. In addition, in two designs, the thickness of the charge storage layer was varied to investigate its effect, however still maintaining an EOT of 400 nm, which is used in the standard

Wafer	h2 material	h1 [nm]	h2 [nm]	h3 [nm]
185	SiO_2		400	
170	Si_3N_4	150	200	150
171	Al_2O_3	150	200	150
172	Si_3N_4	50	200	250
101	Al_2O_3	50	200	250
181	Si_3N_4	250	200	50
182	Al_2O_3	250	200	50
180	Si_3N_4	75	400	125
183	Si_3N_4	100	400	100

Table 3.1.: Dielectric characteristics of the fabricated MIM capacitors.

CMUTs devices. A reference MIM capacitor was also fabricated in which the dielectric consist only of SiO$_2$, as in the standard CMUTs. The size of the capacitors was $300 \times 300 \mu m^2$. The details of the dielectric stack of the fabricated capacitors are summarised in Table 3.1.

3.3. I-V curves

The fabricated MIM capacitors were first characterised by measuring their current-voltage (I-V) curves using a Keithley 237 High Voltage Source Measure Unit. A linear sweep with a voltage step of 1 V and a compliance current of 10 mA was used for the measurements. The results are presented in Fig. 3.1, where the I-V curves of three of the fabricated devices are expressed in terms of current density (J) and electric field across the dielectric (E). For clarity, only three curves are displayed. However, the curves exhibited similar trends for devices with the same material and thickness of the charge storage layer, as the EOT is the same.

The current in the capacitors with Si$_3$N$_4$ and SiO$_2$ exhibits a gradual increase for electric fields above 5 MV/cm until breakdown. Similarly, capacitors with Al$_2$O$_3$ exhibit a gradual rise in current above 5 MV/cm, but followed by a sharp increase before breakdown. The observed I-V trend for Al$_2$O$_3$ aligns with findings from Chapter 2 and [5]. Additionally, the breakdown field for Al$_2$O$_3$ is
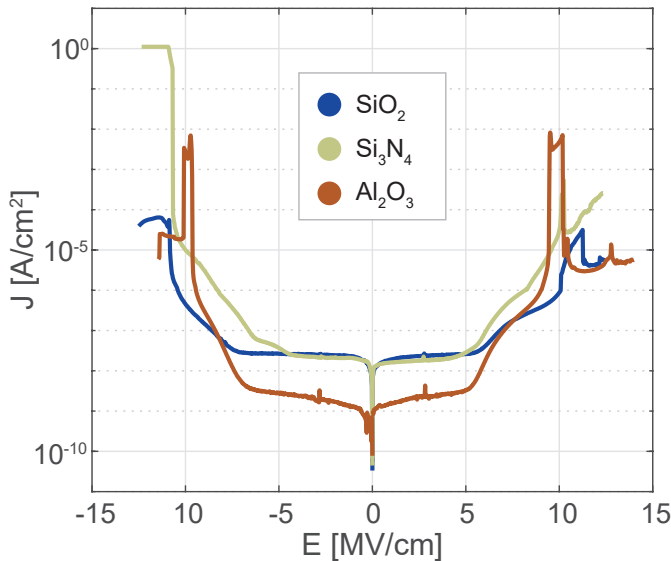
Figure 3.1.: E-J curves to breakdown of MIM capacitors with SiO$_2$ and 200 nm ALD Al$_2$O$_3$ and PECVD Si$_3$N$_4$ charge trapping layer.

lower as compared to Si_3N_4. This, together with the narrow region of steep current increase before breakdown, particularly at electric field magnitudes relevant for charging CMUT devices, points toward the choice of Si_3N_4 as dielectric material.

The I-V curves were also plotted in the corresponding Fowler-Nordheim and Poole-Frenkel plots to identify the conduction mechanism. However, no clear trend could be identified in the plots indicating the presence of any of the two mechanisms. Ultimately, the leakage current of Al_2O_3 at electric fields below 6 MV/cm is one order of magnitude lower compared to the other two materials. This could be due to the different deposition method, namely ALD and PECVD.

3.4. CHARGING PROCESS

To investigate the charging process of the fabricated MIM capacitors, a voltage clamp experiment was performed. A DC voltage of 320 V, corresponding to an electric field of 8 MV/cm, was applied to the top electrode of the MIM structures with a High Voltage Source Meter Unit (Keithley 237) for 120 seconds. The transient current was recorded for the entire duration of the charging process, and is presented in Fig. 3.2. Three distinct groups can be identified in the figure depending on the material of the charge trapping layer and its thickness. The devices with Si_3N_4 show a transient current at least one order of magnitude higher compared to Al_2O_3 and SiO_2 for the entire duration of the charging process. This is in line with the J-E curves in Fig. 3.1, where
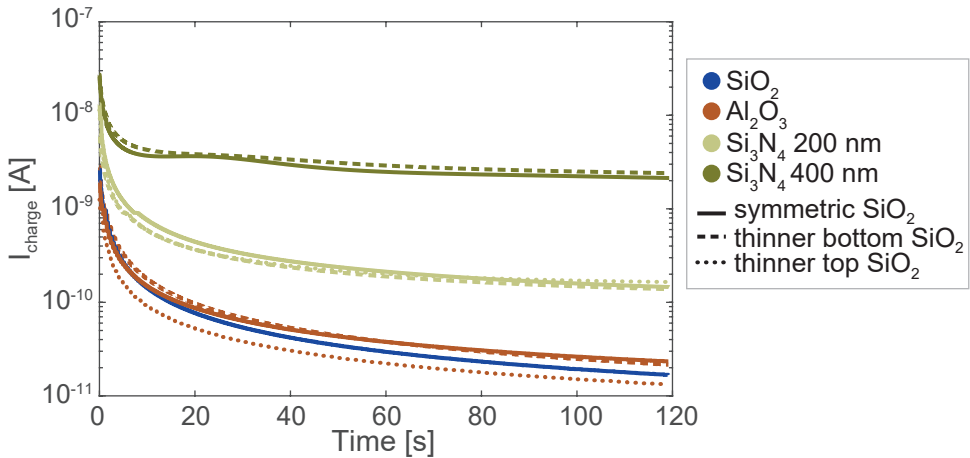
Figure 3.2.: Transient charging current recorded for the different MIM capacitors versions.

the current at 8 MV/cm for the Si_3N_4 sample is about one order of magnitude higher than for Al_2O_3 and SiO_2, while the current for the latter two is similar. As mentioned earlier, this could be due to the different deposition method of the materials, other than the material itself.

Moreover, the thickness of the top and bottom SiO_2 layers in the devices with Al_2O_3 and Si_3N_4 does not significantly impact the charging process, given their equivalent EOT. On the other hand, a thicker Si_3N_4 charge storage layer, specifically the one with twice the thickness, showed a charging current one order of magnitude higher.

The total charge injected into the device is calculated by integrating the measured current transient over the duration of the charging process. The total injected charge is the sum of the charge necessary to charge the electrical capacitance (Q_{ele}) and the charge stored in the dielectric (Q_{stored}):

$$Q_{total} = Q_{ele} + Q_{stored},\tag{3.1}$$

with

$$Q_{ele} = C_{meas} \cdot V_{charge},\tag{3.2}$$

where C_{meas} is the capacitance of the MIM capacitor, which was previously measured, and V_{charge} is the voltage used during the charging process, in this case 320 V. It was verified that the leakage current of the setup was less than 100 fA, therefore negligible with respect to the transient charging current in Fig. 3.2. The results for each MIM variant are summarised in Table 3.2.

Wafer	C_{ele}[pF]	Q_{ele}[nC]	Q_{tot}[nC]	Q_{stored}[nC]
185	8.3	2.7	8.5	5.8
170	7.6	2.4	43.1	40.7
171	8.4	2.7	9.9	7.2
172	7.7	2.5	42.7	40.2
101	8.3	2.6	9.8	7.2
181	7.7	2.5	46.8	44.4
182	8.3	2.7	9.2	6.6
180	7.5	2.4	443.8	441.3
183	7.2	2.3	355.6	353.3

Table 3.2.: Summary of measured and calculated values of capacitance and charge for the tested MIM capacitors.

The values of the measured electrical capacitance (C_{ele}) are consistent across samples with the same dielectric materials, with a slight variation for the Si_3N_4 samples. In addition, there is a seven-fold difference in the charge stored in the dielectric between the 200 nm Al_2O_3 and Si_3N_4 samples, which becomes ten times larger between the 200 nm and 400 nm Si_3N_4 samples. This trend, where a thicker charge storage layer corresponds to a larger amount of trapped charge, aligns with findings in other studies, such as [3, 6]. Nevertheless, comparing these values with typical bulk or surface trap density, they are at lest one order of magnitude higher for all three materials [7–11]. Therefore, this indicates that the charge calculated by integrating the current flowing through the dielectric is not all trapped, and the actual Q_{stored} is lower than the calculated value presented here. Despite it is expected that Si_3N_4 traps more charge than Al_2O_3, as its average trap density is one order of magnitude higher than Al_2O_3 ($\approx 10^{-3}C/m^2$ vs $10^{-4}C/m^2$)[10–12], we can conclude that this method does not allow to correctly estimate the charge stored in the MIM dielectric.

3.5. DISCHARGING PROCESS

At the end of the charging process, a short circuit was applied between the top and bottom electrodes of the MIM capacitors, and the discharge current recorded until the threshold of 200 fA was reached. It should be pointed out that this measurement does not resemble the actual discharge process as, in this case, the discharge current is primarily caused by the charge accumulated at the electrodes. In addition, the trapped charges do not travel across the dielectric stack, therefore the discharge is much faster. Nevertheless, despite not resembling the actual discharge process, the results from this experiment can be used to compare the properties of the different materials [4].

Figure 3.3 presents the discharge current for the different MIM structures. Here, the discharge current through the capacitors with 400 nm Si_3N_4 is not shown for better clarity of the figure. The figure shows that MIM capacitors with the charge storage layer in between two symmetric SiO_2 layers have the highest peak current, with Al_2O_3 showing the highest peak value. Devices with a thinner SiO_2 layer either in contact to the top or the bottom electrode show a smaller peak current and no significant difference appears to exist between the two combinations (thinner at the top or at the bottom), or the two materials.

To gain more insight into the measurements, and quantify the differences between MIM dielectric stack versions, the discharge current can be fitted with a stretched exponential equation in the form:
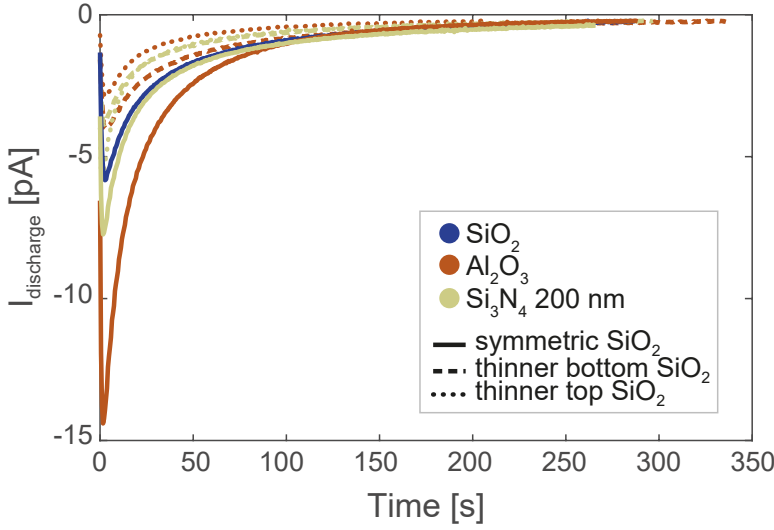
Figure 3.3.: Transient discharging current recorded for the different MIM capacitors versions.

$$I_{discharge} = I_0 \exp\left[-\left(\frac{t}{\tau}\right)^{\beta} \right], \tag{3.3}$$

where τ is the time constant of the discharge process, and β represents the grade of disorder of the system [4]. The values of I_0, τ, and β obtained by fitting the discharge current curves for each MIM variant, averaged across three measurements, are summarised in Table 3.3.

I_0 is the highest for MIM versions with symmetric SiO_2 layers at the top and bottom of the charge storage layer. However, this value reflects the initial charge on the capacitor electrodes, and no significant insights can be gained that can be related to the discharge process of pre-charged CMUTs.

With respect to the time constant, τ, samples with Al_2O_3 show the highest values, followed by the sample with only SiO_2, and Si_3N_4. The time constant models the discharge time, therefore the higher it is, the slower the discharge. However, as just mentioned, the discharge current is mainly caused by the charge on the electrodes, which dominates with respect to the current generated by charge de-trapping in the dielectric. In addition, for the symmetric MIM versions, τ is similar for Al_2O_3 and Si_3N_4, but for the asymmetric versions, the difference in time constant between the two materials becomes more significant, with Al_2O_3 having the highest values, particularly in device versions where the SiO_2 layer in contact with the bottom electrode is thicker. This suggests that having a thicker insulating layer

wafer	I_0 [pA]	τ [s]	β
185	8.96	18.47	0.54
170	14.82	9.80	0.43
171	19.27	13.82	0.59
172	5.83	16.16	0.52
101	5.55	23.60	0.56
181	5.70	9.13	0.46
182	2.88	21.80	0.62
180	8.85	7.68	0.48
183	26.89	8.41	0.44

Table 3.3.: Summary of parameters extracted by fitting the transient discharge current of the tested MIM capacitors with (3.3).

towards ground helps in slowing down the discharge, and that the discharge mechanism of the two materials is different.

Ultimately, the values of β are similar for devices of the same material. This parameter indicates the degree of anisotropy of a material, and the lower the value, therefore the further from the ideal condition of $\beta = 1$, the more complex is the charging process [4, 6]. From these results, Si_3N_4 shows the lowest values of β, therefore indicating a more complex (charging and) discharging process with less uniform charge distribution compared to the other two materials. A possible contributor to these results is the deposition method. If fact, Al_2O_3 which was ALD deposited, show the highest β value, as ALD deposition produces a more organised structure compared to the PECVD-deposited Si_3N_4 and SiO_2.

3.6. CONCLUSION

In this chapter, MIM capacitors fabricated to understand the performance of ALD Al_2O_3 and PECVD Si_3N_4 as charge storage layers, and the influence of the top and bottom SiO_2 layers thickness, were characterised. Both the charging and the discharging processes were analysed by recording the current transients. The results of the charging processes showed that devices with Si_3N_4 can trap a larger amount of charge compared to Al_2O_3, therefore suggesting the choice of Si_3N_4 as material for the charge storage layer. In addition, the results suggest that a thicker layer would be beneficial in trapping a larger amount of charge. However, this could be challenging in case of ALD deposited layers, due to the time required to deposit such thick

layers. Nevertheless, as the calculated values of charge stored in the dielectric were at least one order of magnitude higher than the average trap density reported in literature, the results of these measurement can only be taken as an indication.

The results from the discharging process showed that Al_2O_3 has a slower time constant, therefore a slower discharge, indicating that Al_2O_3 could perform better than Si_3N_4 as dielectric material. The peak current, I_0, had similar values for Al_2O_3 and Si_3N_4, suggesting the presence of a similar amount of charge on the electrodes at the onset of the discharge process. In addition, the stretched exponential coefficient, β, was the lowest for Si_3N_4 samples. This implies a less uniform charge distribution in this material layer compared to Al_2O_3. However, it is important to consider that this non-uniformity could be attributed to the deposition method rather than the material itself.

Ultimately, a MIM capacitor with only SiO_2 as dielectric material was fabricated to compare its charging and discharging behaviour to that of the other MIM capacitors with a charge storage layer. Significant differences between devices with SiO_2, and Si_3N_4 or Al_2O_3 were expected in the results, but were not found.

Eventually, analysing the discharge process of a MIM capacitor by short-circuiting its terminals does not resemble the actual discharge process, which happens with charges moving through the entire dielectric stack, and it is much faster than for a CMUT device. A better approach would be to use the Kelvin Probe method to monitor the decrease of the surface potential over time. However, this measurement tool was not available. Lastly, another drawback of using MIM structures is the difference in contact conditions between insulating layers. In MIM structures, the perfect contact between layers makes the electric field in the dielectric uniform, while in collapse-mode CMUTs, air gaps caused by the roughness of the two surfaces in contact with each other at pull-in will always be present, making the charging and discharging processes different from the one here investigated in the MIM structures.

In summary, the characterisation of the MIM capacitors presented in this chapter did not give a clear indication of which material or which dielectric layer stack combination might have the best performance. The measurements suggest that both ALD Al_2O_3 and PECVD Si_3N_4 consistently trap charge, with Al_2O_3 exhibiting a slower discharge. Furthermore, for the same EOT, an increase in the thickness of the SiO_2 layer at the top and bottom of the charge storage layer correlates with a slower discharge. Nevertheless, a better method to evaluate the charging and discharging characteristics of potential dielectric

stacks should be used in the future. This might be using different devices than MIM capacitors or different measurements methods.

REFERENCES

[1] *Moore4Medical*. Web Page. URL: https://moore4medical.eu/.

[2] G. He and Z. Sun. *High-k gate dielectrics for CMOS technology*. Weinheim: Wiley, 2012.

[3] N. Tavassolian. "Dielectric charging in capacitive RF MEMS switches with silicon nitride and silicon dioxide". PhD Thesis. 2011.

[4] L. Michalas, M. Koutsoureli, E. Papandreou, A. Gantis, and G. Papaioannou. "Assessment of dielectric charging in RF MEMS capacitive switches with the aid of MIM capacitors". In: *2014 29th International Conference on Microelectronics Proceedings - MIEL 2014*, pp. 125–128.

[5] J. T. Gaskins *et al.* "Review—Investigation and Review of the Thermal, Mechanical, Electrical, Optical, and Structural Properties of Atomic Layer Deposited High-kDielectrics: Beryllium Oxide, Aluminum Oxide, Hafnium Oxide, and Aluminum Nitride". In: *ECS Journal of Solid State Science and Technology* 6.10 (2017), N189–N208.

[6] U. Zaghloul, G. J. Papaioannou, H. Wang, B. Bhushan, F. Coccetti, P. Pons, and R. Plana. "Nanoscale characterization of the dielectric charging phenomenon in PECVD silicon nitride thin films with various interfacial structures based on Kelvin probe force microscopy". In: *Nanotechnology* 22.20 (2011), p. 205708.

[7] S. W. Hsieh, C. Y. Chang, and S. C. Hsu. "Characteristics of low-temperature and low-energy plasma-enhanced chemical vapor deposited SiO2". In: *Journal of Applied Physics* 74.4 (1993), pp. 2638–2648.

[8] C. H. Ling and C. Y. Kwok. "Plasma-enhanced chemical vapour deposited SiN films: bulk charge, interface trapping and polarization". In: *Vacuum* 38.8 (1988), pp. 865–868.

[9] Y. C. Park, W. B. Jackson, N. M. Johnson, and S. B. Hagstrom. "Spatial profiling of electron traps in silicon nitride thin films". In: *Journal of Applied Physics* 68.10 (1990), pp. 5212–5221.

[10] J. J. H. Gielis, B. Hoex, M. C. M. Van De Sanden, and W. M. M. Kessels. "Negative charge and charging dynamics in Al_2O_3 films on Si characterized by second-harmonic generation". In: *Journal of Applied Physics* 104.7 (2008), p. 073701.

[11] Y.-S. Lee, Y.-H. Lee, H.-j. Ju, W.-J. Lee, H. S. Lee, and S.-K. Rha. "Characteristics of SiO2/Si3N4/SiO2 stacked-gate dielectrics obtained via atomic-layer deposition". In: *Journal of nanoscience and nanotechnology* 11.7 (2011), pp. 5795–9.

[12] X. Zhang, B.-W. Liu, Y. Zhao, C.-B. Li, and Y. Xia. "Influence of annealing temperature on passivation performance of thermal atomic layer deposition Al_2O_3 films". In: *Chinese Physics B* 22.12 (2013), p. 127303.

4

THE SECOND-GEN PRE-CHARGED CMUTs

This chapter is based on:

- M. Saccher, R. Van Schaijk, S. Kawasaki, J. H. Klootwijk, A. Rashidi, V. Giagka, A. S. Savoia, and R. Dekker. "A Comparative Study of Si_3N_4 and Al_2O_3 as Dielectric Materials for Pre-Charged Collapse-Mode CMUTs". In: *2023 IEEE International Ultrasonics Symposium (IUS)*. 2023, pp. 1–4

4.1. INTRODUCTION

In recent years, new ultrasound market have emerged to meet new customer demands, including continuous organ monitoring and handheld systems connectable to smartphones. Ultrasound transducers are now also used as wireless power receivers for implantable devices. However, traditional manufacturing processes, especially those using lead zirconate titanate (PZT) ultrasound transducers, have high manual labour costs and use toxic metals, limiting their suitability for certain applications. Micromachined ultrasonic transducers (MUTs) offer a (biocompatible) alternative to traditional PZT transducers.

In this chapter, a second generation pre-chargeable CMUT design is fabricated and characterised, and four CMUT variants, each with a different layer stack, are compared. The CMUTs here presented are designed to operate in collapse mode, which occurs when the top membrane makes partial contact with the dielectric layer above the bottom electrode. Collapse-mode operation allows to achieve enhanced transmit and receive sensitivity, and an

output pressure up to three times higher compared to non-collapse-mode [2, 3]. This increase is due to the higher electric field in the vacuum cavity caused by the high bias voltage and smaller effective gap height. To obtain bias-free pre-charged collapse-mode CMUTs, a charge storage layer is incorporated in the dielectric stack, as for the previous devices generation. Previous studies have utilised pre-charged CMUTs with Si_3N_4 or SiO_2 in the dielectric [3–6]. Park et al. [6] and Choi et al. [4] have demonstrated the feasibility of pre-charged CMUTs with Si_3N_4 as the dielectric, exhibiting good charge retention over time, even at high temperatures. However, the reported pre-charged CMUTs are mostly used in non-collapse-mode operation, with the exception of Ho et al. [5]. It is evident from these studies that trapping sufficient charge to achieve a pre-charged collapse-mode CMUT is challenging, and the choice of material for the charge-trapping layer is crucial.

The objective of this chapter is to compare the performance of PECVD Si_3N_4 and ALD Al_2O_3 as charge storage layers in the dielectric of the pre-charged collapse-mode CMUTs. The performance is evaluated in terms of charge trapping, charge retention, and acoustic performance.

4.2. CMUTS FABRICATION

In the context of the Moore4Medical project [7], collapse-mode CMUTs were fabricated by Philips with the aim to be used as ultrasonic power receiver. The CMUT processing was based on a sacrificial release process, and at low temperatures (< 400°C), making them CMOS compatible.

The newly developed CMUTs are designed with a lower centre frequency, around 3 MHz, and therefore have a larger membrane diameter of 355 μm compared to the devices presented in Chapter 2. The dielectric of the standard CMUT devices, which consists of SiO_2 only, was replaced by a stack which includes a charge storage layer. A schematic cross-section of the fabricated devices is shown in Fig. 4.1(b).

Four layer stack variants were designed and fabricated. In all of them, the thickness of the charge storage layer is 200 nm and two variants were fabricated with ALD-deposited Al_2O_3, while for the other two PECVD-deposited Si_3N_4 was used to get a better understanding of the performance of the two materials in real CMUT devices other than MIM capacitors. Furthermore, for each material type, two thicknesses were employed for the PECVD SiO_2 layer in contact with the bottom electrode. One variant utilises 120 nm SiO_2 PECVD TEOS, while the other variant has 200 nm SiO_2 TEOS. The choice of fabricating devices with two different SiO_2 thicknesses was to experimentally validate the hypothesis introduced in Chapter 3, suggesting that a thicker SiO_2
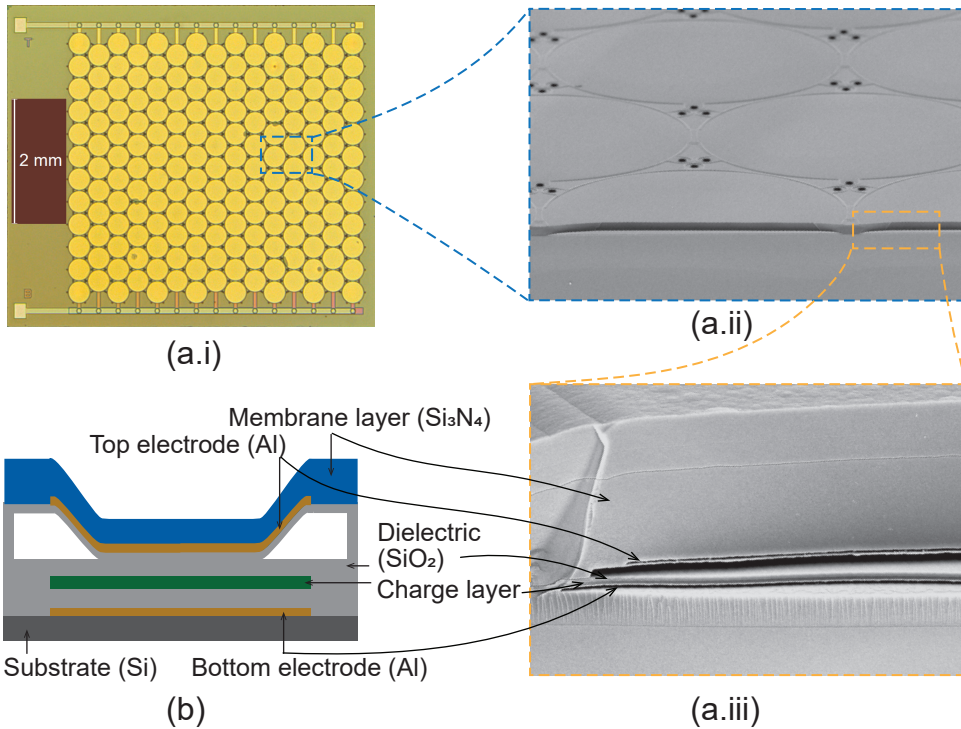
Figure 4.1.: (a.i) Microscope photograph of fabricated CMUT die composed of 173 cells connected in parallel. (a.ii) Scanning Electron Micrograph (SEM) photograph of the CMUT cross-section. (a.iii) Magnification of SEM photograph showing the different layers of a CMUT cell. (b) Schematic structure of the fabricated CMUT with charge storage layer, highlighting the corresponding structures in the SEM image.

layer in contact with the bottom electrode may improve charge retention.

Two arrays of different sizes were fabricated: a $5 \times 5\,mm^2$ single-element transducer, consisting of 173 CMUT cells electrically connected in parallel, and a $20 \times 20\,mm^2$ array composed of 16 $5 \times 5\,mm^2$ partitions, arranged in a 4×4 configuration. Figure 4.1(a) shows the $5 \times 5\,mm^2$ fabricated array, together with SEM pictures of the membrane showing the different layers in the device.

4.3. MIM TEST CAPACITORS

MIM capacitors of size $300 \times 300\,\mu m^2$ were also included in the mask design of the CMUTs. They have the same dielectric stack of the CMUTs as they are exposed to the same processing steps, and they are used to test the properties of the CMUTs dielectric. The capacitance of the entire dielectric stack, between the the top and bottom electrode was measured for the four
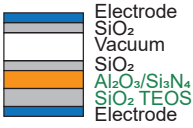
	TEOS 120 nm		TEOS 200 nm	
	Si_3N_4 (w223)	Al_2O_3 (w225)	Si_3N_4 (w218)	Al_2O_3 (w221)
Capacitance [pF]	9.6	10.5	8.0	8.5
EOT [nm]	340	311	406	383

Table 4.1.: Summary of dielectric characteristics of the fabricated MIM capacitors.

variants. The EOT was then estimated considering a SiO_2 permittivity $\epsilon_r = 4.1$. The results are reported in Table 4.1.

The capacitors were then used to determine the breakdown voltage of the dielectric stack. This was done by measuring their I-V curves. The voltage was linearly swept from $0\,V$ until breakdown, with $1\,V$ increments using a Keithley 237 High Voltage Source Meter Unit with a compliance current of $5\,mA$. Figure 4.2 presents the results in the form of J-E curves, where the electric field was calculated using the EOT values from Table 4.1.

Comparing the curves of the Si_3N_4 samples to the ones of Al_2O_3, it can be observed that the current density (J) of Si_3N_4 samples is slightly higher than for Al_2O_3 ones. Moreover, Si_3N_4 exhibits a higher breakdown field than Al_2O_3. Specifically, the Al_2O_3 samples have a breakdown field around 8 to $8.5\,MV/cm$, while the breakdown of Si_3N_4 samples is between 8.5 and $9.5\,MV/cm$. In addition, the two dielectric materials show different J-E curves shapes, with Al_2O_3 showing a narrow region of fast charging above $7.5 - 8\,MV/cm$, while Si_3N_4 shows a more gradual increase in current before breakdown. These findings align with the trends observed in Chapters 2 and 3.
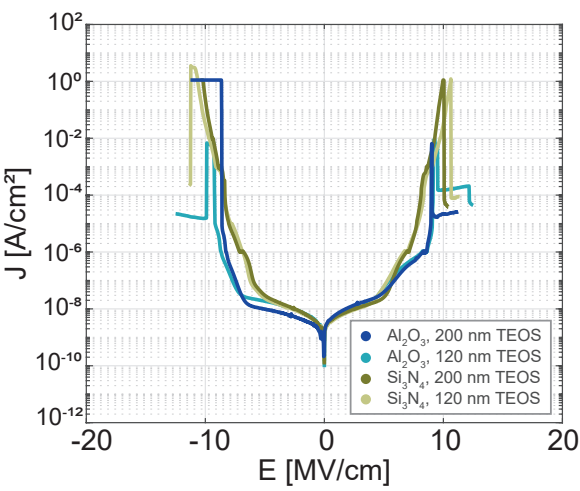
Figure 4.2.: I-V curve of test capacitors with Al_2O_3 and Si_3N_4.

4.4. CMUTs PRE-CHARGING AND CHARACTERISATION

The fabricated CMUTs were then pre-charged with electric fields ranging from 7.5 to 9 MV/cm, both with positive and negative polarity with respect to the bottom electrode. Each charging voltage was applied to a pristine device for 5 minutes. To evaluate the effect of the charge stored in the dielectric on the CMUT's collapse voltage, Capacitance-Voltage (C-V) curves were measured.

4.4.1. C-V MEASUREMENTS

To minimise any alteration of the stored charge in the device, a fast C-V protocol was employed, with a voltage sweep rate of 80 V/ms. A small AC signal of 125 MHz was superimposed on a 200 Hz triangular wave varying between 0 V and ± 200 V. The change in the phase of the impedance when the CMUT goes in and out of collapse is used to draw the C-V curve. Two measurement protocols were used: a DC bipolar sweep between positive and negative voltages for uncharged devices, and a DC unipolar sweep of either only positive or negative voltages, for devices charged with positive and negative polarity, respectively.

In Fig. 4.3(a) and (d), the C-V curves of the four CMUT variants charged with an electric field of ± 8 MV/cm are compared to those of corresponding pristine devices. The C-V curve of the pristine devices exhibits symmetry around 0 V, indicating that the CMUT is not in a collapsed state and has no charge stored in the dielectric. On the other hand, the pre-charged devices show a shift in the point of minimum capacitance of 60 to 100 V, indicating that they are in a collapsed state even at 0 V bias, and the presence of charge in the dielectric.

Figures 4.3(b) and (e) depict the impact of different charging electric fields on the shift in the C-V curves for the Si_3N_4 variants, and (c) and (f) for the Al_2O_3 variants. As expected, the shift is larger for higher charging electric fields due to increased current tunnelling through the CMUT dielectric. In addition, charging the 120 nm TEOS Al_2O_3 devices with an electric field exceeding 8 MV/cm was only feasible with negative polarity, as devices charged with positive polarity experienced dielectric breakdown. An analogous behaviour can be observed for the 200 nm TEOS Si_3N_4 and Al_2O_3 devices, as charging with an electric field of 9 MV/cm could only be achieved with a negative polarity electric field. Different charging mechanisms and characteristics of the two dielectric materials could explain these differences and are a topic for further investigation.

The shift in collapse voltage due to the charge trapped in the Si_3N_4 and Al_2O_3 layers is summarised in Table 4.2. Both the Si_3N_4 variants exhibit a
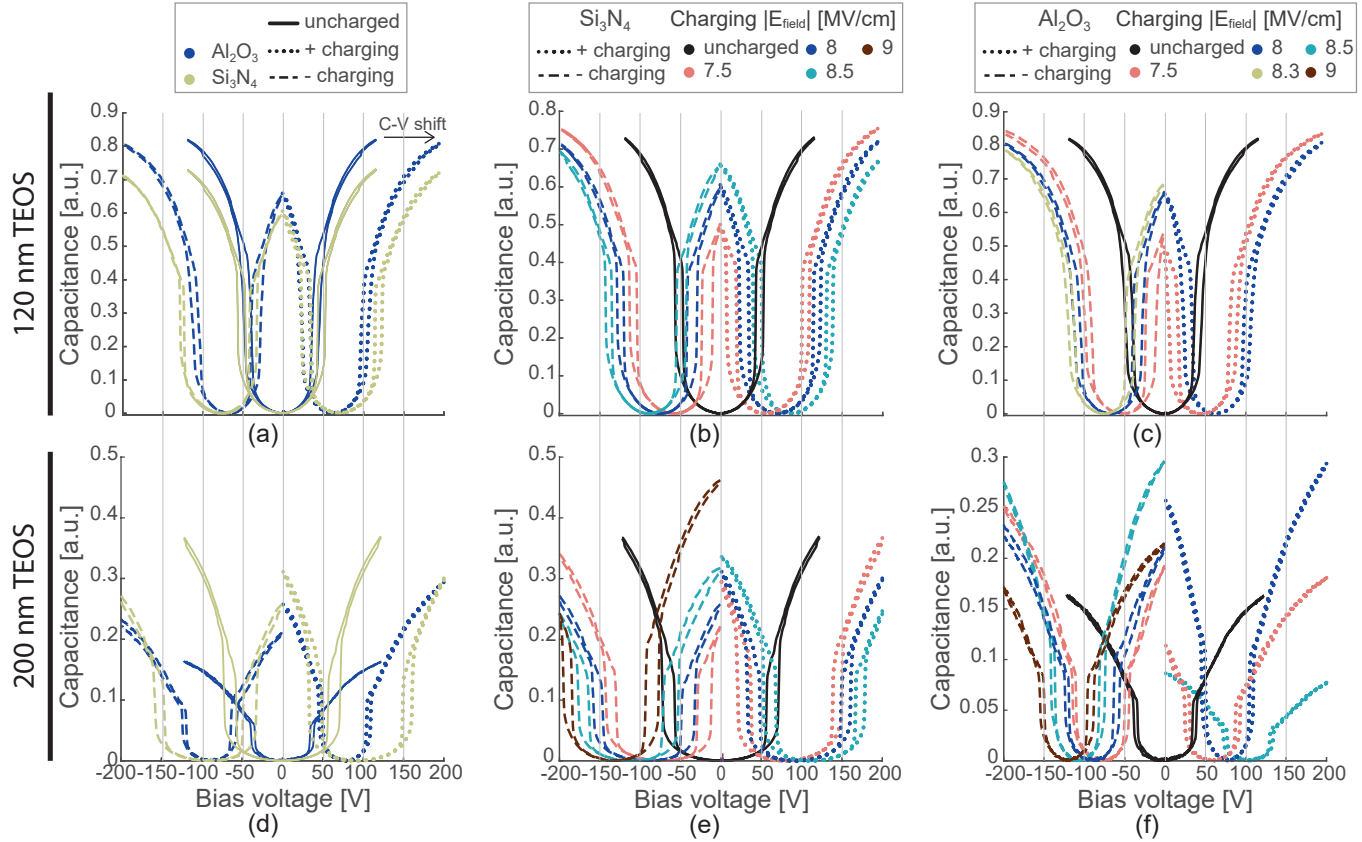
Figure 4.3.: (top row) 120 nm SiO_2 TEOS bottom dielectric. (bottom row) 200 nm SiO_2 TEOS bottom dielectric. (a) and (d) Comparison of C-V curve shift between Si_3N_4 and Al_2O_3 samples when charged with ± 8 MV/cm electric field. (b) and (e) Comparison of C-V curve shift for Si_3N_4 samples when charged with different electric fields and polarity. (c) and (f) Same as (b) but for Al_2O_3.

larger shift in the C-V curve compared to the Al_2O_3 ones for both polarities. This aligns with the findings presented in Chapter 3, where the charging process results for Si_3N_4 MIM capacitors indicated a higher charge trapping capability compared to those with Al_2O_3. As mentioned in the previous chapter, this can be due to the different deposition method (PECVD vs ALD) and not only the different dielectric material of the two devices.

Additionally, charging the device with a negative polarity causes a larger shift in the C-V curve, except for the 200 nm TEOS Si_3N_4 variant which shows, although minimal, an opposite trend. However, this could be due to some imprecision in the measurement or inherent variations between samples, and the magnitude of the difference remains small. Comparing the C-V shift for the two thicknesses of bottom SiO_2, the 200 nm variants show a larger shift compared to the thinner TEOS, indicating that more charge is stored. A larger amount of stored charge implies a higher equivalent built-in bias voltage, with two main consequences: a shift in the device's resonant frequency towards higher values [8] which in turn affects the device sensitivity, and a longer lifetime, which will be discussed in Section 4.6.

		Charging Efield [MV/cm]					
		−8.5	**−8**	**−7.5**	**7.5**	**8**	**8.5**
120 nm TEOS	**Si₃N₄**	-91.7	-77.1	-59.9	59.8	74.7	90.7
	Al₂O₃		-68.7	-53.4	48.6	66.7	
200 nm TEOS	**Si₃N₄**	-114.8	-94.8	-76.6	85.2	97.1	116.1
	Al₂O₃	-106.7	-90.2	-79.8	58.5	78.2	91.4

Table 4.2.: Summary of the shift in minimum capacitance voltage extracted from the C-V measurements of the four pre-charged CMUTs variants.

4.4.2. DHM measurements

To further evaluate and verify the differences in stored charge between samples, the membrane profile of the CMUTs was characterised using a Digital Holographic Microscopy (DHM) (LynceeTec, Switzerland). DHM is a non-contact method used to characterise 3D topography. It uses two coherent laser beams, capable of forming interference. The beams are focused on the sample to analyse, and the reflection from the sample is recorded by a camera. The reflected beam encodes the phase difference due to the different surface heights of the analysed sample as variations in intensity that are then processed to give real-time images of the sample's profile.
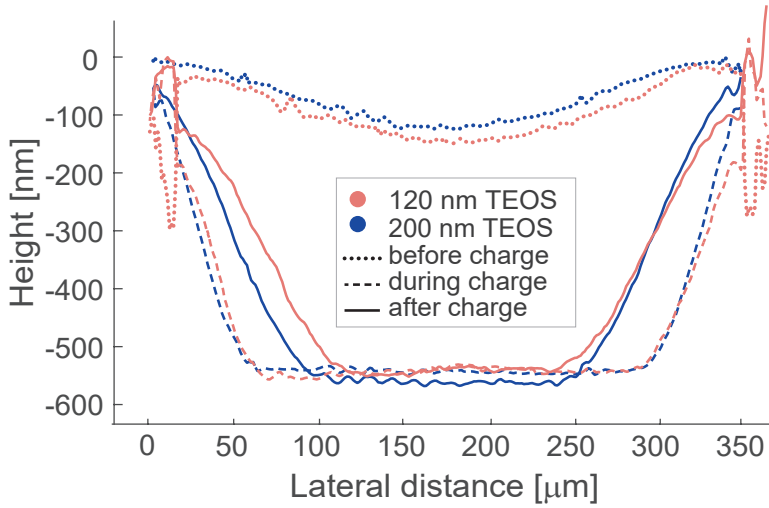
Figure 4.4.: CMUT membrane profile measured with DHM before, during and after charging for the Si₃N₄ variants.

The two Si_3N_4 variants were compared, and the membrane profile was measured before, during, and after charging. The samples were both charged with $-8\,MV/cm$. Figure 4.4 illustrates a similar bending before charge, and an equivalent collapsed area during charging. When comparing the profile after charge, the 200 nm TEOS version shows a larger collapsed area than the 120 nm version, suggesting that more charge is stored in the device. These findings align with the results obtained from the C-V curve measurements, providing further confirmation that the 200 nm TEOS version stores more charge compared to the thinner oxide under the same charging parameters.

Furthermore, it is important to note that the stored charge occupies a larger area compared to the collapsed region after charging. This has potential implications for the performance of CMUTs, specifically in terms of sensitivity and power reception, which should be investigated in the future.

4.5. ACOUSTIC PERFORMANCE

Next, the acoustic performance of the pre-charged CMUTs was evaluated by measuring the transmit and receive sensitivity. For these measurements, the $5 \times 5\,mm^2$ CMUTs arrays were used. They were mounted on a PCB and coated with a thin layer of PBR (Polybutadiene rubber).

4.5.1. RECEIVE SENSITIVITY

The receive sensitivity is the ability of the ultrasonic transducer to convert incoming acoustic pressure into output voltage, and it is influenced by the CMUT (built-in) bias voltage. Therefore, for each of the CMUT variants, four samples charged with electric fields from -7.5 to -9 MV/cm were prepared. The receive sensitivity was measured in a water tank at 1 and 2.5 MHz by using a commercial single element piston PZT transducer as transmitting transducer (TX). The pre-charged CMUTs were used as receiving transducers (RX) and centred at a distance of 110 mm and 210 mm for the 1 and 2.5 MHz experiment respectively. The pressure field generated by the TX at this distance was previously measured by a needle hydrophone. More details on the TX characterisation can be found in Chapter 6. The input pressure at the RX surface was swept from 0 to 0.35 MPa, and from 0 to 0.2 MPa at 1 and 2.5 MHz respectively. In this range, the relationship between input voltage and output pressure of the TX is linear. The open circuit voltage at the CMUT terminals was measured with an oscilloscope for each input pressure value. The values were fitted with a linear relationship, and the receive sensitivity calculated for each of the samples.

Figure 4.5 presents the results of the measured receive sensitivity showing that the highest values are achieved at 1 MHz, and that there is a dependency on the charging electric field, therefore on the equivalent built-in bias. At 1 MHz, devices charged with an electric field of -7.5 MV/cm show the best performance, while at 2.5 MHz, the highest receive sensitivity is achieved for devices charged with -8.5 MV/cm. This can be explained by looking at the phase of the impedance of an exemplary CMUT sample, measured in water after charging (Fig. 4.5(c)). In this example, charging the device at -7.5 MV/cm results in a resonant frequency closer to 1 MHz than for the other charging electric fields. On the other hand, charging the device with -8.5 MV/cm results in a resonant frequency closer to 2.5 MHz than for the other electric fields.

Ultimately, the measured receive sensitivity values of the pre-charged CMUTs are comparable to the typical values of the standard devices without charge trapping layer, and externally biased. Typical sensitivity values for standard CMUTs range between 20 and 25 V/MPa at the tested frequencies when externally biased with 120 V (data obtained from Philips internal source). Therefore, the receive sensitivity results are in line with those of standard CMUT devices.

4
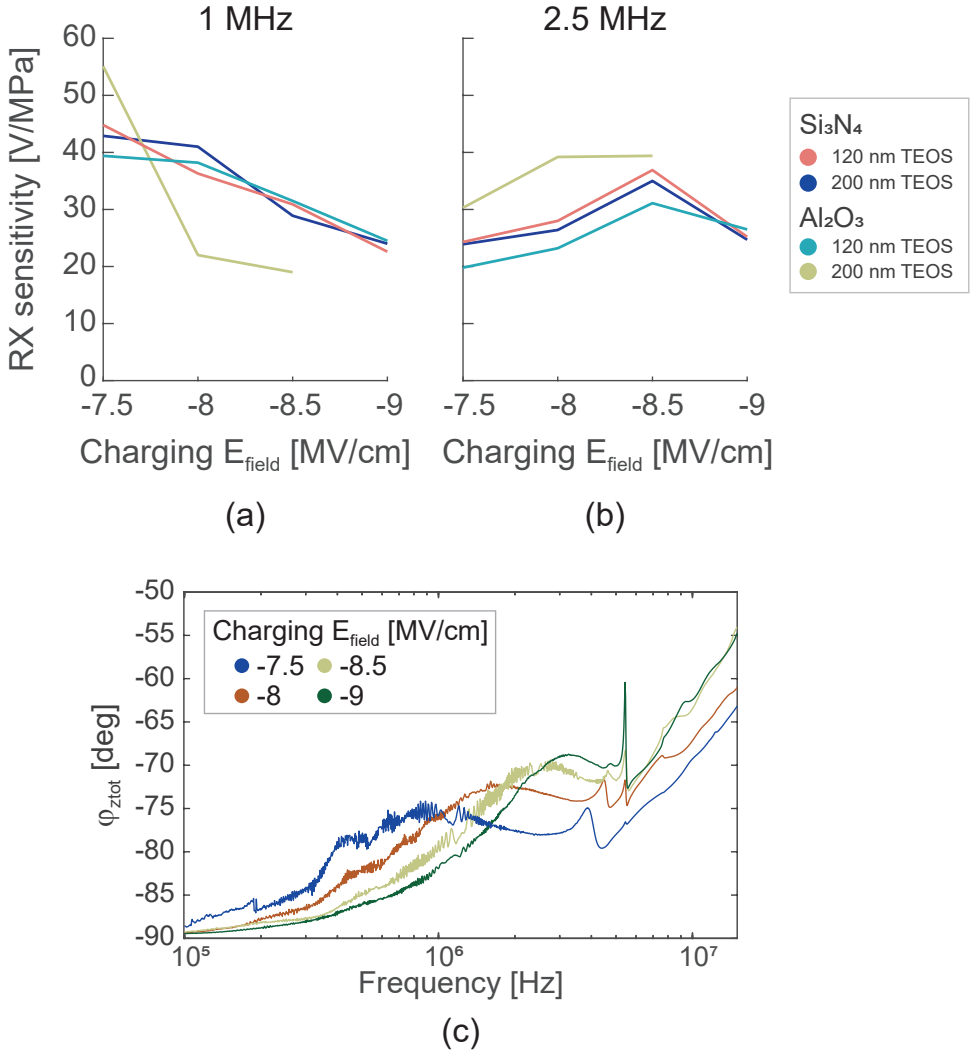
Figure 4.5.: Receive sensitivity measurements at (a) 1 MHz and (b) 2.5 MHz. (c) Example of impedance phase measured in water for CMUTs charged with electric fields between −7.5 to −9 MV/cm.

4.5.2. TRANSMIT SENSITIVITY

Transmit sensitivity refers to the ability of the ultrasonic transducer to convert an electrical input signal into a corresponding acoustic signal. For this experiment, new samples were used and pre-charged with an electric field of −8 MV/cm. They were immersed in a water tank, and a needle hydrophone (Precision Acoustic, UK) was used to measure the output pressure at 3 mm
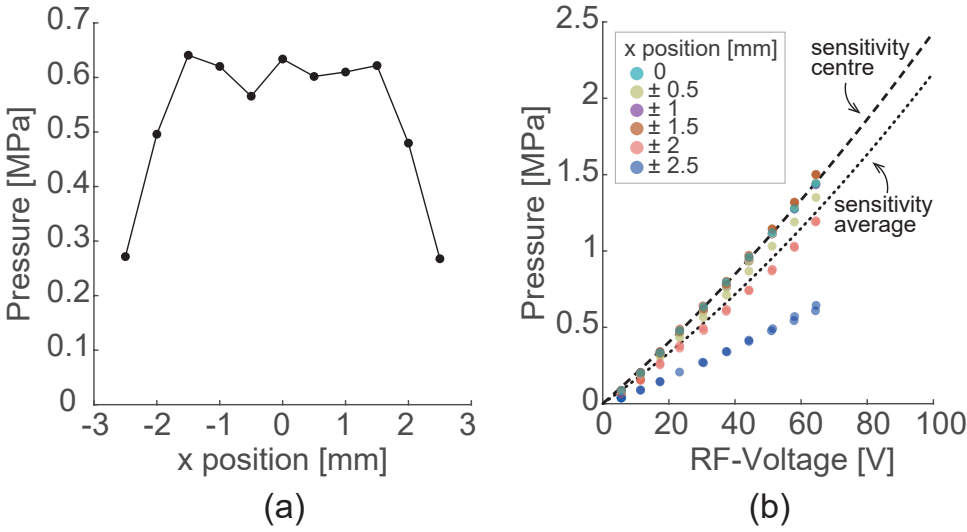
Figure 4.6.: Transmit sensitivity measurements. (a) Example of measured pressure across sample width. (b) Example of measurements results showing the relationship between input RF voltage and output pressure across the sample surface.

distance from the surface of the CMUT. The hydrophone was scanned across a plane parallel to the CMUT surface from -2.5 to $2.5\,\text{mm}$ in $0.5\,\text{mm}$ steps with respect to the centre of the CMUT. The driving signal was a 2-cycles unipolar squared wave at $2.6\,\text{MHz}$ and $50\,\%$ duty cycle with amplitude swept from 6 to $60\,\text{V}$ in $6\,\text{V}$ steps.

Figure 4.6(a) shows an example of pressure profile measured while scanning the hydrophone along the CMUT width. Looking at the pressure over the sample width, it can be observed that it is not constant, having at the centre and around $\pm1.5\,\text{mm}$ the highest amplitude. Therefore, two values were calculated for the transmit sensitivity: centre sensitivity, calculated as the ratio between measured pressure and input RF voltage at the centre of the CMUT sample (at $\text{x} = 0$), and average sensitivity, calculated as the ratio of pressure over input voltage across the entire sample width. Figure 4.6(b) illustrates the

	TEOS 120 nm		**TEOS** 200 nm	
	Si$_3$N$_4$ (w223)	**Al$_2$O$_3$ (w225)**	**Si$_3$N$_4$ (w218)**	**Al$_2$O$_3$ (w221)**
Sensitivity centre [kPa/V]	17.4	14.7	19.3	19.1
Sensitivity average [kPa/V]	13	11.7	15.6	15.4
Pout max [MPa]	1.46	1.38	1.42	1.5

Table 4.3.: Summary of results from transmit sensitivity measurements.
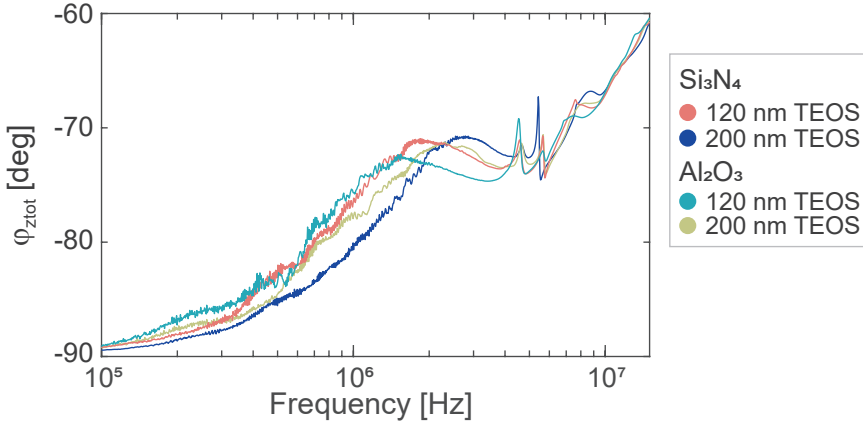
Figure 4.7.: Impedance phase measured in water for the tested CMUT variants charged with an electric field of $-8\,MV/cm$.

measurements data from one of the samples, showing the fitting of the two sensitivities. The results for the four samples are summarised in Table 4.3.

Comparing the values in Table 4.3, the samples showing the highest transmit sensitivity, both at the centre and the average, are the ones with the thickest TEOS layer, with the Si_3N_4 sample having the best performance. Table 4.3 also lists the maximum output pressure achieved with the tested samples, which follows the same performance trend as the transmit sensitivity. This can again be explained by looking at the phase of the impedance of the tested CMUTs after charging (Fig. 4.7). In fact, the samples with the highest sensitivity are the ones with their resonant frequency closer to the test frequency (2.6 MHz). Furthermore, the transmit sensitivity is comparable to the transmit sensitivity of standard CMUT devices biased at 120 V without the charge storage layer, which typically ranges around 20 kPa/V.

Finally, it should be pointed out that the transmit sensitivity was measured only at 2.6 MHz, which is around the centre frequency for which the devices are designed for. Therefore, it should be evaluated at the intended frequency of operation for a more precise assessment of the performance.

4.6. LIFETIME

Lifetime is one of the most important parameters of a device as it determines, among other things, the range of applications in which it can be used. Depending on the application, the minimum required lifetime can vary from hours, in the case of a disposable device, or a few months, for acute applications, to years.

Charge retention over time represents the major challenge for the pre-charged collapse-mode CMUTs, and it depends on the material of the dielectric layer, the deposition method and the structure of the device. Given that pre-charged CMUTs are not (yet) a commercial product, there are no established reliability standards to adhere to. Consequently, the lifetime requirement for "point-of-care" applications was considered, which is $7 \cdot 10^9$ cycles [9]. This criterion is also employed to evaluate the lifespan of standard CMUTs. However, the tested parameters for standard devices differ from those examined here, as the objective for standard devices is to minimise charge trapping and, if present, facilitate its rapid release [9–12].

Three types of measurements were performed to estimate the lifetime of the pre-charged CMUTs. A static lifetime test in which CMUT samples underwent Accelerated Lifetime Tests (ALTs) with temperature as an accelerating factor. In the other two tests, the CMUTs were operated in transmit mode. For one test, their impedance was monitored over time, and for the other, their output pressure.

4.6.1. STATIC LIFETIME

To get a first indication of the speed at which the stored charge gets de-trapped, Accelerated Lifetime Tests (ALT) were performed with temperature as an accelerating factor. By performing multiple tests at different temperatures, the lifetime of the devices can be estimated for the desired temperature (e.g. the body temperature of 37 °C). However, in these tests, the devices are not operated either in transmit or receive mode, therefore only their "static" lifetime can be estimated, representing conditions such as storage or periods of non-operation. In addition, at high temperature, the devices mechanical characteristics can vary significantly, and failure mechanisms other than charge de-trapping may also be accelerated compared to as they occur in actual operation conditions. Yet, these measurements can still provide a useful general estimation of the lifetime associated with the use of Si_3N_4 or Al_2O_3.

For these reasons, only two device variants were tested. CMUTs with a TEOS thickness of 120 nm were chosen, and the effect of PECVD Si_3N_4 and ALD Al_2O_3 compared. CMUTs on a bare die were pre-charged with an electric field of -8 MV/cm for 300 seconds, and placed on a hotplate set at temperatures ranging from 140 °C to 160 °C. An impedance analyser (Keysight E4990A, 20 Hz - 30 MHz) was programmed to measure the CMUT impedance at regular intervals of time until the device failure. The time to failure at different test temperatures was defined as when more than half of the CMUT membranes are out of collapse-mode, and it was determined using the method described in Chapter 2. The test was repeated at least two times for each experimental
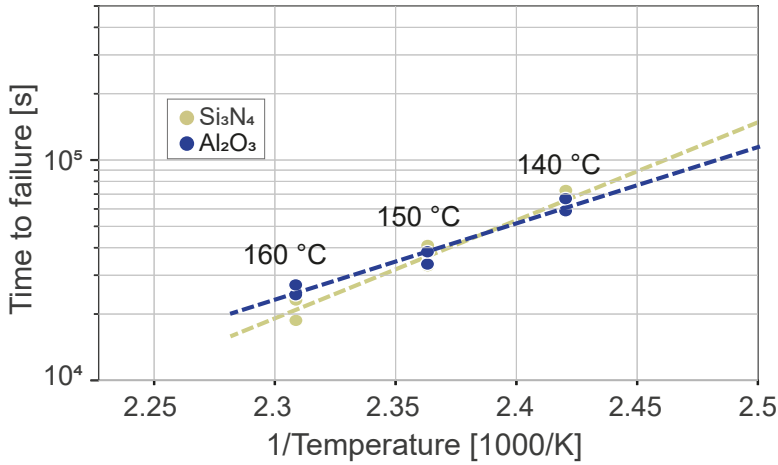
Figure 4.8.: Fitting of the results from the static ALT measurements for the 120 nm Al_2O_3 and Si_3N_4 tested samples.

condition.

Figure 4.8 presents the experimental results, fitted to extrapolate the devices lifetime at lower temperatures. The predicted lifetime of the Si_3N_4 variant is longer than for the Al_2O_3 variant. In addition, comparing Fig. 4.8 to Fig. 2.11 from Chapter 2, the lifetime, estimated at the same experimental conditions, appears to be longer for the newly fabricated devices. It should be noted that this lifetime prediction is based on the fitting of an exponential relationship, therefore small variations in time to failure at high test temperatures result in large variations in estimated lifetime at lower temperatures such as body or ambient temperature. Yet, the predicted static lifetime showed promising results at 37 °C, with about 7.8 years for the Si_3N_4 variant, and 1.2 years for the Al_2O_3 variant.

4.6.2. Dynamic lifetime

Dynamic lifetime measurements were performed next. In these measurements, the CMUTs were actively driven with a 2-cycles squared wave at 2.6 MHz and 50 % duty cycle with a pulse repetition frequency of 90 or 100 kHz. This pulse repetition is almost 100 times faster than what is typically used in most imaging applications, and can potentially accelerate the failure of the devices. However, choosing a lower pulse repetition frequency would require a much longer measurement time, making the total test duration unfeasible in the context of this work.

Monitoring the devices impedance

For this experiment, CMUTs on a bare die were pre-charged with an electric field of -8 MV/cm for 300 s. They were immersed in Fluorinert and their impedance was monitored over time by using an impedance analyser. The setup used for this experiment is shown in Fig. 4.9. To determine the number of cycles to failure, the value of the CMUT equivalent electrical capacitance, extrapolated from the measured impedance, was compared to the value of the electrical capacitance at pull-in, which is around 80 pF for all the CMUT variants. This value was used as threshold to determine the lifetime of the devices.

Figure 4.10(a) shows the results of the experiments for samples stressed with voltage amplitudes of 60 V unipolar. This amplitude is the maximum amplitude used in standard CMUTs in transmit mode. It can be seen that the two samples with 120 nm TEOS have a similar lifetime, while for the samples with 200 nm TEOS, the Al_2O_3 variant seems to have a better performance compared to Si_3N_4. In Fig. 4.10(b), 120 nm Si_3N_4 samples were stressed with different unipolar pulse amplitudes to evaluate the effect on the lifetime. As expected, lowering the pulse amplitude significantly increases the lifetime. These results can be used to define the range of applications for which these pre-charged CMUTs can be used, keeping in mind that the decrease in electrical capacitance over time corresponds to a performance degradation as the CMUTs cells gradually snap back to the uncollapsed state.

Furthermore, in Section 4.4 it was shown that by charging the CMUTs with an higher electric field, more charge is stored in the device. The lifetime of 200 nm Si_3N_4 samples when charged with -8 and -8.5 MV/cm was then compared to test if the additional charge stored for high charging electric
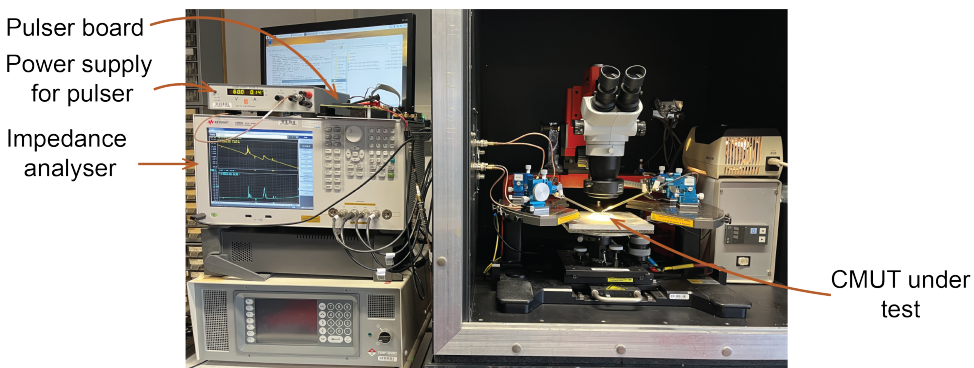
Figure 4.9.: Experimental setup used for the static and impedance monitoring dynamic lifetime tests.
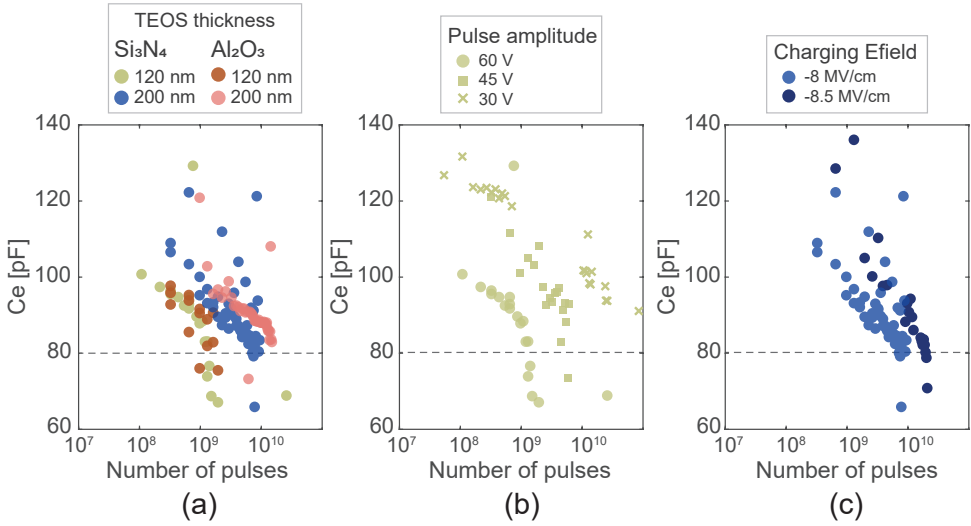
Figure 4.10.: Dynamic lifetime results from impedance monitoring tests. (a) Comparison of electrical capacitance (C_e) over the number of stimulus pulses for the four tested variants. Results for unipolar stimulus with 60 V amplitude. (b) Effect of unipolar stimulus on the lifetime of 120 nm TEOS Si_3N_4 samples. (c) Effect of charging electric field on 200 nm TEOS Si_3N_4 samples when stimulated with unipolar pulses with 60 V amplitude.

fields also translates into a longer lifetime. Figure 4.10(c) confirms that charging the device with a higher electric field results in a longer lifetime. However, it should be noted that the decrease in electrical capacitance over time follows the same trend, therefore the longer lifetime is mainly due to the higher amount of charge stored rather than a slower discharge mechanism.

Ultimately, considering a threshold of 10^9 cycles for the lifetime, the data in Fig. 4.10(a) indicates that only the samples with 200 nm TEOS maintain an electrical capacitance above 80 pF. However, as shown in Fig. 4.10(b), their lifetime can be significantly improved by reducing the stimulus amplitude.

MONITORING THE DEVICES OUTPUT PRESSURE

A second series of experiments was then performed to monitor the devices output pressure over time in a water tank while stressed with pulses. For this experiment, the CMUTs were not pristine and they were re-charged with an electric field of -7.5 MV/cm for 300 s. A needle hydrophone (Precision Acoustic, UK) was centred at 3 mm distance with respect to the CMUT surface. A 2-cycles bipolar squared wave with a pulse repetition frequency of 100 kHz and a peak-to-peak amplitude of 45 V was used.

In Fig. 4.11 the results from these tests are presented. The samples with a

200 nm TEOS Al_2O_3 layer show the best performance with only a 6.6 % drop at the threshold of 10^9 cycles. These results are in line with the results in the previous section. The 200 nm TEOS Si_3N_4 version showed a decrease in output pressure of 10 %, followed by the devices with the thinner SiO_2 layer with Al_2O_3 and Si_3N_4 having a 13.2 % and 22.7 % drop, respectively. The significant decrease in output pressure for the 120 nm TEOS Si_3N_4 sample could be due to an already degraded sample, as the pressure drop is expected to be similar to the Al_2O_3 version, in line with the results presented in the previous section.

However, a direct comparison between these results and those obtained by monitoring the change in impedance is not straightforward. The samples used for these experiments were charged with a lower electric field, and they were not pristine due to a limited availability of wirebonded and encapsulated samples. Additionally, the stimulus in these experiments was bipolar, whereas the other series of experiments utilised a unipolar stimulus. Consequently, it is not possible to definitively conclude that a specific drop in capacitance after a certain number of cycles corresponds to a certain reduction in output pressure. Nevertheless, the key takeaway from these two measurements is that they exhibit a similar trend. To better assess the performance degradation in terms of reduced output pressure, additional tests should be conducted.
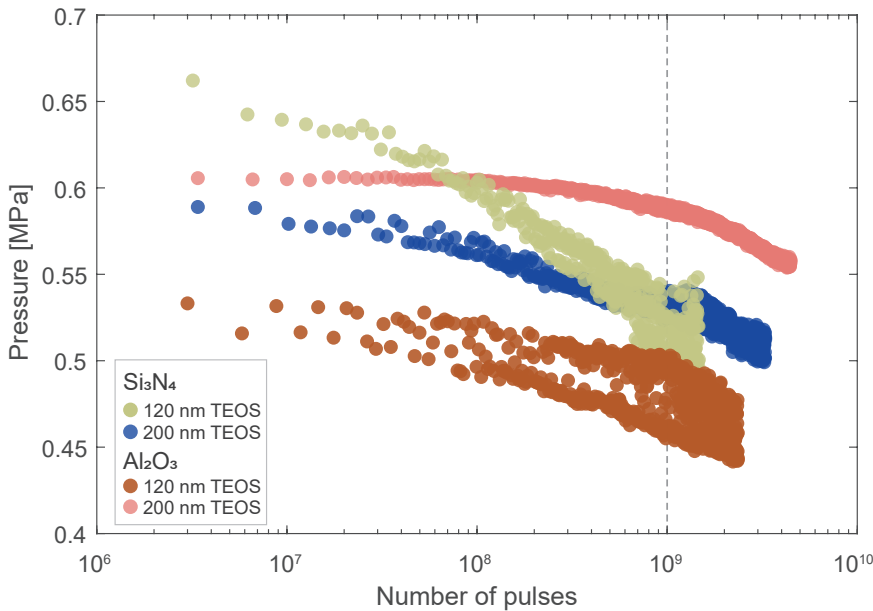
Figure 4.11.: Dynamic lifetime results from output pressure monitoring tests for the four CMUTs variants.

4.7. CONCLUSION

In this chapter, the second generation of pre-charged CMUTs was characterised in terms of charge trapping and retention, and acoustic performance. It was shown that Si_3N_4 samples trap more charge compared to their Al_2O_3 counterpart, and that a thicker SiO_2 TEOS layer also contributes to a larger amount of stored charge. This also translates into a longer lifetime. On the other hand, using a thicker dielectric requires a higher charging voltage to obtain the same electric field in the stack which could require specialised equipment for its generation.

In addition, the lifetime of these devices was tested in transmit mode, using driving conditions normally employed to assess the lifetime of standard CMUT devices for imaging applications. Given that pre-charged CMUTs are not yet commercialised and lack a specified target lifetime, evaluating their performance can be challenging, especially considering their gradual degradation over time. This gradual degradation is advantageous compared to standard devices, where a short-circuit in one cell can abruptly impact the DC bias to other cells, leading to sudden failure. In the case of pre-charged CMUTs, adjustments to the driving parameters could potentially compensate for their degradation. Furthermore, charging the devices with a higher electric field did not seem to induce dielectric degradation, as their performance degradation followed a similar trend to that observed when charged with a lower electric field. It is important to note that the CMUTs were exclusively tested in transmit mode, and future tests in receive mode should be performed to assess their lifetime for other applications such as power receivers.

Moreover, the results from the static lifetime are contradictory to the ones of the dynamic lifetime as in the former, Si_3N_4 samples showed longer lifetime prediction compared to Al_2O_3. However, as mentioned earlier, the static lifetime measurements are based on the fitting of an exponential relationship. Therefore, some small measurement errors at the high test temperatures, could have affected the estimated lifetime at a much lower temperature. Additionally, high temperature could have elicited different discharge mechanisms in the two different materials.

Overall, it is important to emphasise that reliability is a statistical process. Obtaining an accurate estimation of lifetime would require testing a more extensive number of samples. The reported results serve as a preliminary exploration, offering some initial insights.

Finally, both transmit and receive sensitivities are crucial parameters in various applications of ultrasonic technology, such as medical imaging, or industrial testing. The reported sensitivity values align with those of standard CMUT devices and surpass those reported in Chapter 2. This suggests that

pre-charged CMUTs have the potential to replace standard externally biased devices, especially in applications with medium-short lifetime requirements. Further improvements to the dielectric stack could enhance their stability and extend their lifetime, broadening their potential applications.

REFERENCES

[1]   M.   Saccher, R.   Van Schaijk, S.   Kawasaki, J. H.   Klootwijk, A.   Rashidi, V.   Giagka, A. S.   Savoia, and R.   Dekker. "A Comparative Study of Si_3N_4 and Al_2O_3 as Dielectric Materials for Pre-Charged Collapse-Mode CMUTs". In: *2023 IEEE International Ultrasonics Symposium (IUS)*. 2023, pp. 1–4.

[2]   K. K.   Park, O.   Oralkan, and B. T.   Khuri-Yakub. "A comparison between conventional and collapse-mode capacitive micromachined ultrasonic transducers in 10-MHz 1-D arrays". In: *IEEE Transactions on Ultrasonics, Ferroelectrics, and Frequency Control* 60.6 (2013), pp. 1245–1255.

[3]   A.   Kshirsagar, A.   Sampaleanu, R.   Chee, W.   Moussa, and R. J.   Zemp. "Pre-charged CMUTs with efficient low-bias voltage operation for medical applications". In: *2013 IEEE International Ultrasonics Symposium (IUS)*. IEEE, 2013.

[4]   W. Y.   Choi, C. H.   Lee, Y. H.   Kim, and K. K.   Park. "Comparison of Si_3N_4–SiO_2 and SiO_2 Insulation Layer for Zero-Bias CMUT Operation Using Dielectric Charging Effects". In: *IEEE Transactions on Ultrasonics, Ferroelectrics, and Frequency Control* 67.4 (2020), pp. 879–882.

[5]   M.-C.   Ho, M.   Kupnik, K. K.   Park, and B. T.   Khuri-Yakub. "Long-term measurement results of pre-charged CMUTs with zero external bias operation". In: *2012 IEEE International Ultrasonics Symposium*. IEEE, Oct. 2012.

[6]   K. K.   Park, M.   Kupnik, H. J.   Lee, O.   Oralkan, and B. T.   Khuri-Yakub. "Zero-bias resonant sensor with an oxide-nitride layer as charge trap". In: *2010 IEEE Sensors*. IEEE, Nov. 2010.

[7]   *Moore4Medical*. Web Page. URL: https://moore4medical.eu/.

[8]   M.   Pekař, W. U.   Dittmer, N.   Mihajlović, G.   Van Soest, and N.   De Jong. "Frequency Tuning of Collapse-Mode Capacitive Micromachined Ultrasonic Transducer". In: *Ultrasonics* 74 (2017), pp. 144–152.

[9]   R.   Van Schaijk, M.   In 'T Zandt, P.   Robaeys, M.   Slotboom, J.   Klootwijk, and P.   Bekkers. "Reliability of collapse mode CMUT". In: *2023 IEEE International Ultrasonics Symposium (IUS)*. IEEE, 2023.

[10]   U.   Zaghloul, G. J.   Papaioannou, B.   Bhushan, F.   Coccetti, P.   Pons, and R.   Plana. "New insights into reliability of electrostatic capacitive RF MEMS switches". In: *International Journal of Microwave and Wireless Technologies* 3.5 (2011), pp. 571–586. URL: https://dx.doi.org/10.1017/S1759078711000766.

[11]   R. W.   Herfst. "Degradation of RF capacitive switches". PhD Thesis. 2008.

[12]   X.   Rottenberg, B.   Nauwelaers, W. D.   Raedt, and H. A. C.   Tilmans. "Distributed dielectric charging and its impact on RF MEMS devices". In: *34th European Microwave Conference, 2004*. Vol. 1. 2004, pp. 77–80.

5

ULTRASOUND AS A POWER SOURCE: FEASIBILITY AND MITIGATION STRATEGIES

This Chapter is based on:

- M. Saccher, A. Rashidi, A. S. Savoia, V. Giagka, and R. Dekker. "Phase Distribution Efficiency of cm-Scale Ultrasonically Powered Receivers". In: *2023 IEEE International Ultrasonics Symposium (IUS)*. 2023, pp. 1–4

- M. Saccher, S. S. Lolla, S. Kawasaki, and R. Dekker. "Time-efficient low power time/phase-reversal beamforming for the tracking of ultrasound implantable devices". In: *2022 IEEE International Ultrasonics Symposium (IUS)*. IEEE

5.1. INTRODUCTION

Implantable bioelectronics have revolutionised patient lives by delivering localised and on-demand therapies. Pacemakers, cochlear implants, and deep brain stimulators are some of the successfully commercialised examples. Depending on the application, these implants have different power requirements ranging from a few microwatts for sensing applications [3], to tens of milliwatts for high-density stimulation backends [4].

Among the different powering methods for wireless implants, ultrasonic power links have demonstrated superior scalability when using micromachined transducers [3, 5–7], and low energy losses in soft tissue (around $0.6\,\text{dB}/(\text{cm}\,\text{MHz})$). In addition, the ultrasound beam can be precisely focused

on the target receiver by using transmitting (TX) phased arrays, minimising the power losses in the areas surrounding the receiver [8].

Although most of the reported ultrasonically powered implants have a micro- or millimetre-scale receiving aperture [3, 5, 6, 9], in some cases, the high power demands of the application require cm-scale receivers. For instance, Wong et al. [10] demonstrated the first monolithic integration of power-receiving PMUTs on an ASIC, at the cost of a low aperture efficiency. To compensate for the low efficiency, they use an aperture area of $30\,\mathrm{mm}^2$. Another example is from Zhang et al. [11], where an array of 36 parallel single-element piezoelectric crystals with a total aperture area of $1.3\,\mathrm{cm}^2$ is used to deliver $280\,\mathrm{mW}$ to power a deep brain stimulator. Nonetheless, previous research predominantly employed a single element transducer as the receiver (RX). This can cause a significant decrease in harvestable power when the phase distribution across the RX area becomes uneven.

In this chapter, we investigate the impact of lateral and angular misalignment on the phase distribution of the acoustic field across the RX surface. We evaluate its effect on the harvestable power as a function of RX areas ranging from mm^2 to cm^2. Several strategies to mitigate the misalignment effect are proposed and analysed both through simulations and experiments.

5.2. BASIC CONCEPT

In Fig. 5.1(a) the phase of the ultrasound field produced by a single element TX transducer with a 39 mm diameter and 2.5 MHz centre frequency is shown at different planes parallel to the surface of the TX. The planes are located at 10 mm, 50 mm, and 100 mm, to represent the location of a RX transducer in the body. The figure shows that, for diameters smaller than the TX transducer and in the near field, the phase distribution is rather uniform. However, in a realistic scenario, where the TX is placed outside of the body, and the RX is in the body, perfect alignment between the two will rarely occur, and lateral and angular misalignment will be present. This scenario is depicted in Fig. 5.1(b), where the RX plane is tilted by 15° with respect to the TX surface. It can be observed that the phase distribution of the ultrasound field is uneven across the entire surface. In this condition, each point on the RX surface is at a different distance from the TX surface. Therefore, the ultrasound wave hits the different points on the surface of the RX at a different time, causing a phase difference compared to the parallel configuration. In Fig. 5.1(c), the pressure waves at different points on the RX surface are shown for the perfectly aligned case (top plot), and for a tilt of 5° (bottom plot). When using a single-element RX transducer, the usable harvested power originates from
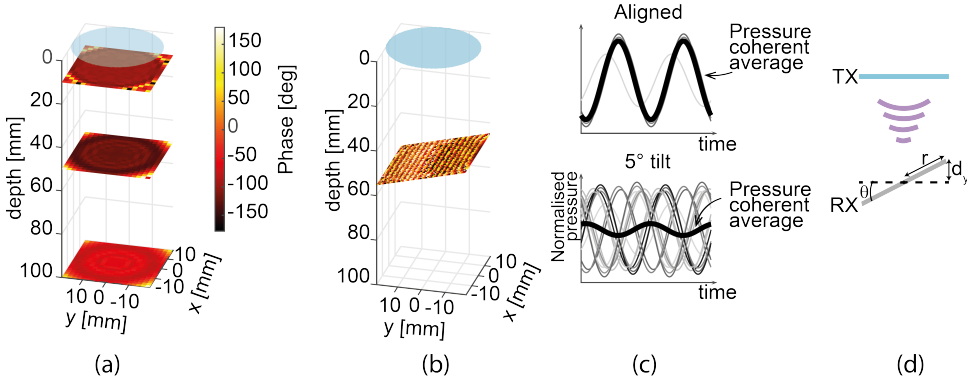
Figure 5.1.: (a) Simulation of phase distribution on planes parallel to the TX, located at 10 mm, 50 mm, and 100 mm. The blue circle indicates the TX transducer. (b) Simulation of the phase distribution on a plane tilted by 15°, and located at 50 mm from TX. (c) Simulations of pressure waves at locations on a square RX transducer at 50 mm from the TX. (top) perfectly aligned case, (bottom) tilt of 5° with respect to the TX surface. The thick black line indicates the coherently averaged pressure across the RX surface. Driving conditions are the same for the aligned and tilted case. Data in (a to c) is obtained from ultrasound field simulations using FOCUS [12]. (d) Schematic representation of the effect of an angular misalignment between TX and RX.

the coherent average of the pressure integrated across the RX surface (shown as a thicker trace in Fig. 5.1(c)). Comparing the top and bottom plots of Fig. 5.1(c), it can be observed that, due to the angular tilt, the pressure waves are shifted in time, causing a significantly lower pressure average, therefore lower usable power. Assuming that the acoustic wave impinging on the RX surface is planar, the difference in phase compared to the parallel case can be calculated with the following equation, which refers to Fig. 5.1(d):

$$d_y = r \cdot \sin(\theta)$$
$$\Delta_{\mathrm{phase}} = \frac{\mathbf{d_y}}{c} \cdot f \cdot 360°,$$

(5.1)

where r is the distance from the centre of the RX transducer, θ is the tilt angle, c is the speed of sound in the medium, and f is the frequency. In addition, (5.1) shows that the larger the receiver, the greater the phase difference across its surface, which significantly reduces the benefit of using cm-scale receivers to harvest a higher amount of power.

5.2.1. SIMULATION OF THE ULTRASOUND FIELD AT THE RECEIVER

To understand the impact of lateral and angular misalignment on the phase distribution of the acoustic field across the RX surface, the ultrasound field

generated by the TX transducer was simulated using FOCUS [12]. The TX
transducer is a circular, single-element piston transducer. Squared receivers
with sizes ranging from $4 \times 4 \, mm^2$ to $20 \times 20 \, mm^2$ were simulated, and the
harvestable power for various misalignment scenarios was computed at
different depths. Water was used as the medium for the simulations.

5.3. Lateral misalignment

Figure 5.2 shows the effect of lateral misalignment between TX and RX on
the amount of harvestable power at the RX, assuming that TX and RX are
on parallel planes. In each of the plots of Fig. 5.2, the power at the RX is
normalised with respect to the maximum harvestable power in the simulated
area. The figure shows that a bigger receiver is less sensitive to lateral
misalignments (Figs. 5.2(a) vs (c), and (d) vs (f)). Fig. 5.2 also illustrates
that the diameter of the TX transducer influences the impact of the lateral
misalignment. For a large diameter TX transducer, such as 39 mm, and a
receiver size from $4 \times 4 \, mm^2$ to $20 \times 20 \, mm^2$, lateral misalignment up to 10 mm
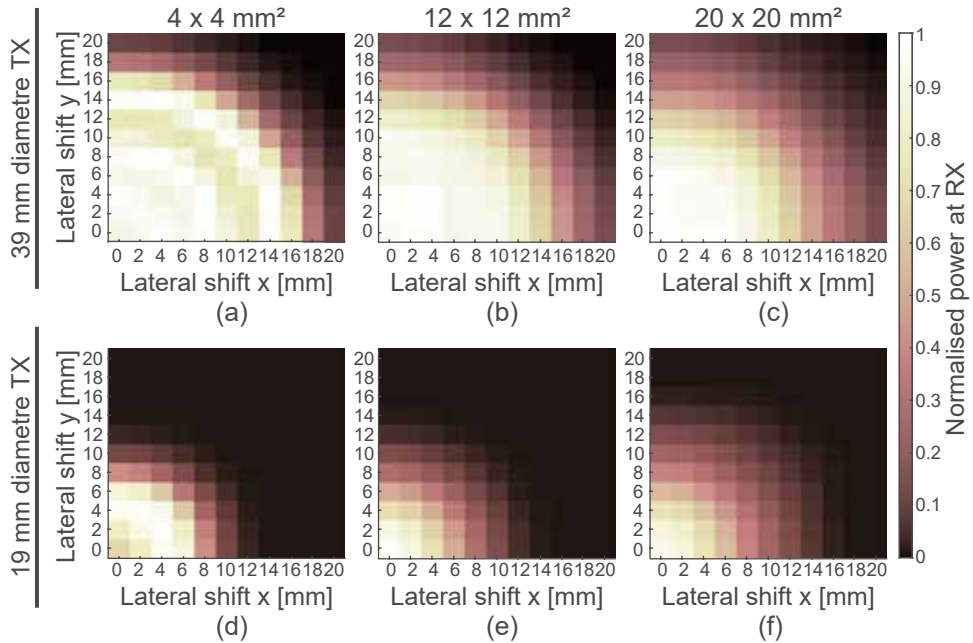
Figure 5.2.: Simulated normalised power at the RX with respect to a lateral shift between
TX and RX at a distance of 50 mm between TX and RX transducer, and at a frequency of
2.5 MHz. Top row is for a 39 mm TX diameter, and the bottom row is for a 19 mm TX
diameter. (a & d) $4 \times 4 mm^2$ RX. (b & e) $12 \times 12 mm^2$ RX. (c & f) $20 \times 20 mm^2$ RX.

results in a power loss of less than 30 % (Fig. 5.2 top row). By using a TX with about half the diameter (19 mm), the maximum lateral misalignment to achieve the same power loss is about 5 mm (Fig. 5.2 bottom row). This is explained by the linear relationship between the TX and beam diameter at the focus point, where most of the energy is concentrated. The −6 dB beam diameter (BD) for a flat transducer at the focus point can be calculated with the following equation:

$$BD(-6\,\text{dB}) = 0.2568D, \tag{5.2}$$

where D is the TX diameter [13].

The results shown in Fig. 5.2, are for a distance between TX and RX of 50 mm. While these outcomes remain comparable for distances of 10 and 100 mm, they are influenced by the geometry and centre frequency of the TX transducer; factors that define the far-field distance. Therefore, the lateral misalignment at which a specific power loss occurs will vary. Nevertheless, the position of the RX is usually approximately known, and larger lateral misalignments, especially of more than 20 mm, are unlikely in realistic scenarios. Therefore, if a suitable TX transducer is chosen, the impact of lateral misalignment on harvestable power is not significantly detrimental.

5.4. ANGULAR MISALIGNMENT

Figure 5.3 shows the effect of angular misalignment on the harvestable power at the RX. The power at the RX is normalised with respect to the maximum power among the simulated conditions, which is for the perfectly aligned case. The power loss is very significant for RX with larger areas, where an angular misalignment of 1° already causes a drop of 25 % in the harvestable power for a $20 \times 20\,\text{mm}^2$ receiver. This is because the larger the area, the greater the phase difference across the RX, therefore the higher the power loss (see (5.1)). In addition, the comparison of Fig. 5.3(a) and (b) shows that different TX diameters have a similar impact on the effect of the angular misalignment, and that the latter is comparable at different distances between TX and RX.

5.5. MITIGATION STRATEGIES

As mentioned earlier in this chapter, in a realistic scenario, where the TX is placed outside of the body, and the RX is in the body, lateral and angular misalignment will be present. However, mitigation strategies can be put in place to minimise these effects. Below, three of them are listed and they will be discussed in the next paragraphs:
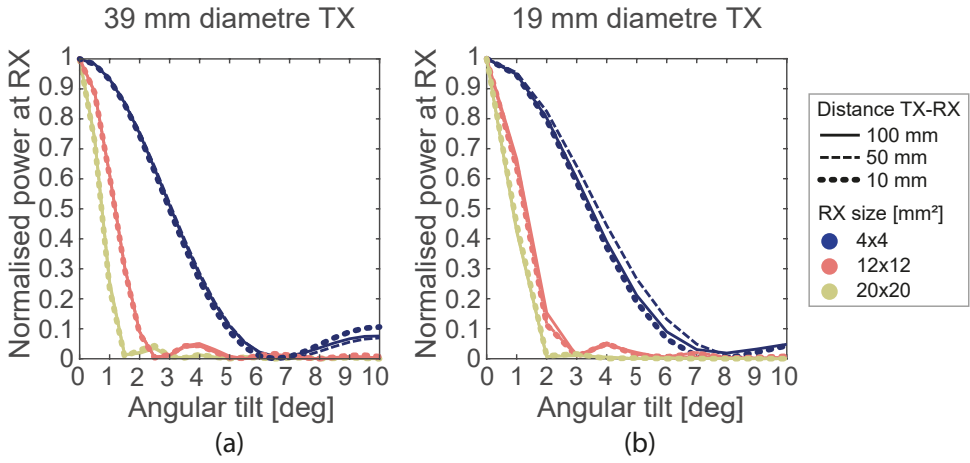
Figure 5.3.: Simulated effect of angular tilt of the RX on the harvestable power depending on the receiver size and the distance. (a) for a TX diameter of 39 mm; (b) for a TX diameter of 19 mm.

- Decreasing the frequency;

- Using a linear or matrix array RX transducer;

- Using a linear or matrix array TX transducer with a tracking algorithm.

5.5.1. Decreasing the frequency

The ultrasonic wavelength, λ, is inversely proportional to the frequency ($\lambda = c/f$). Therefore, at a lower frequency, the effects of both lateral and angular misalignment can be reduced since the phase difference between two points separated by a certain distance decreases as the wave period becomes larger. Figure 5.4(a) and (b) show the effect of angular misalignment at different frequencies and for two RX transducers of sizes $5 \times 5 \, \text{mm}^2$ and $20 \times 20 \, \text{mm}^2$, respectively. We compared the results of the simulations with experimental data obtained using two different pre-charged collapse-mode CMUT devices as RX transducers with the same area as the simulations (Fig. 5.4(c & d)). These devices are the same CMUTs as the ones presented in Chapter 4. The experimental data were acquired using the setup in Fig. 5.5. The setup allows the movement of the RX transducer in 3D by operating 3 linear micromanipulators for adjustment in *x-y-z* direction, and a rotational micromanipulator for angular adjustment with respect to the frontal plane (parallel to the TX). The CMUT was connected to a resistive load, and the voltage across its terminals measured with an oscilloscope to compute the
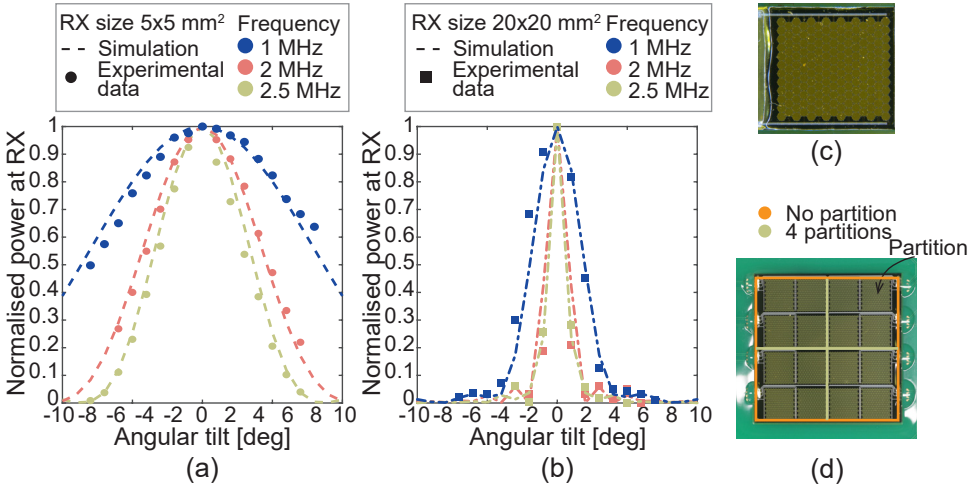
Figure 5.4.: (a) Comparison of simulation and experimental data in case of angular misalignment at different frequencies for a $5 \times 5\,mm^2$ RX. (b) Same as (a), but for a $20 \times 20\,mm^2$ RX. (c) Photograph of the $5 \times 5\,mm^2$ CMUT RX. (d) Photograph of the $20 \times 20\,mm^2$ CMUT RX. This receiver is composed of 16 partitions with the same size as (c). The orange square indicates the area of the RX when all the partitions are connected together in parallel, forming a single element. The 4 yellow squares indicate the subdivision in 4 partitions, achieved by connecting the 4 partitions in each yellow square in parallel, forming a single element.

dissipated power. The results were normalised with respect to the maximum power among the simulated and measured values. The figure shows that the experimental results are in agreement with the simulations.

5.5.2. USING A LINEAR OR MATRIX ARRAY RX TRANSDUCER

Using a linear or matrix array RX transducer is another possible solution to mitigate the power loss, especially due to angular misalignment [14]. In fact, for the same RX area, by increasing the number of partitions (elements), their area will be smaller, therefore the phase variation across each of them decreases, reducing the power loss. The effects of partitioning the RX transducer on the harvestable power at the load are shown in Figure 5.6. The presented results are for a $20 \times 20\,mm^2$ RX transducer, as this was the most critical scenario presented in the previous section. The TX was a circular single-element transducer with $39\,mm$ diameter. The larger the angular misalignment, the higher the number of partitions necessary to recover a defined amount of power. However, as discussed in the previous section, by using a lower frequency, this can be reduced. In fact, comparing the effect of
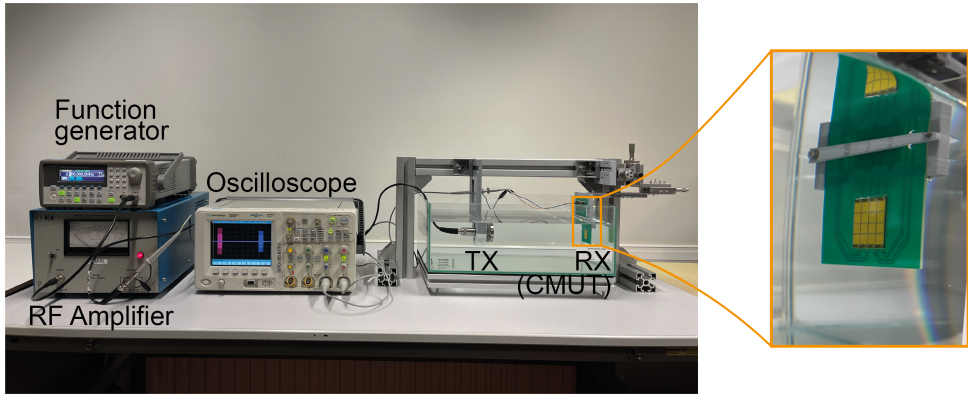
Figure 5.5.: Experimental setup used to validate the simulation results.

5

partitioning the RX for different frequencies presented in Fig. 5.6, it can be inferred that the determining dimension is the size of the partition in terms of number of wavelengths λ. In addition, for a factor 2 increase in the frequency, the number of squared partitions to compensate for the same power loss at a certain angle is a factor 4 (×2 on each side of a partition). This undoubtedly increases the complexity in device packaging and circuitry. In fact, for this solution to work, each partition requires at least an individual rectifier such that the power harvested by each partition, and more specifically, the current generated by each partition, can be added together in the DC domain. These aspects will be further discussed in Chapter 6. It must be pointed out that these simulations analyse only a few combinations of TX-RX shape, dimensions, size of RX partitions, and frequency, and results may be different for other combinations.

The simulation results in Fig. 5.6(a) have been validated with experimental data. To acquire the data, we used the setup shown in Fig. 5.5, and the RX was a pre-charged collapse-mode CMUT of size $20 \times 20\,\mathrm{mm}^2$ subdivided in 16 partitions, shown in Fig. 5.4(d). Each partition was connected to a separate full bridge wave rectifier with their outputs connected in parallel to each other, and to a single purely resistive load. To obtain the results for 4 partitions, the 16 partitions of the RX were connected in parallel groups of 4, forming 4 quadrants, and each of them was connected to a full bridge wave rectifier and to a resistive load. Also in this case, the experimental results are in agreement with the simulations.
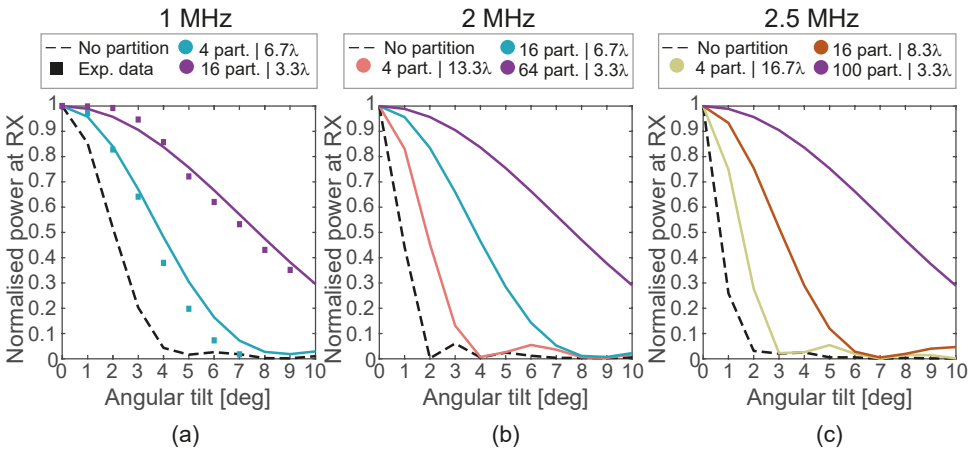
Figure 5.6.: Effect of partitioning on the harvestable power for a $20 \times 20\,mm^2$ RX, for different angular misalignment, and for different frequencies, namely $1\,MHz$, $2\,MHz$, and $2.5\,MHz$. The solid and dashed lines represent the results of the simulations, while the squared markers denote the experimental data. The distance between TX and RX was adjusted such that the RX was in the position where maximum power could be received, respectively (a) $221\,mm$, (b) $161\,mm$, (c) $215\,mm$.

5.5.3. USING A LINEAR OR MATRIX ARRAY TX TRANSDUCER WITH A TRACKING ALGORITHM

In a real case scenario, the position of the RX with respect to the external transmitting transducer is not known a priori, and changes over time due to motions of the body or the small movements of the hand - for a hand-held US transducer - which, depending on the location, can reach values up to $3\,mm/s$ [15]. Therefore, if the RX is moving, the TX focus should mirror its movements to avoid power losses.

The results presented until this point have been obtained by using a single element TX transducer, which generates an ultrasound field of fixed shape and at a fixed position. Therefore, to follow the movements of the RX, it should be physically moved accordingly. This operation would be very complex, if not impossible, in a real application. On the other hand, by using a linear or matrix array, the ultrasound beam can be focused to a desired location without moving the transducer itself. This is known as beamforming, and it is at the base of ultrasound imaging. Many beamforming algorithms are available and can also be used for power transfer applications to focus the beam onto the RX location.

However, the RX should be first located in the body. This can be done in two ways: active tracking or passive tracking [16]. Active tracking requires

the active driving of the US RX element, while passive tracking uses an US wave sent by an external TX that is backscattered by the RX element. Active tracking offers a greater penetration depth since US travels only in one direction through the media, but it requires considerably more power than passive tracking. Here, the passive tracking method was chosen and the use of a beamforming algorithm was investigated. The chosen algorithm relies on the phase difference of the US signal backscattered by the RX transducer to precisely focus the US beam on the RX and create a tight ultrasound link robust against small movements. This algorithm is called time/phase reversal beamforming.

Time/phase reversal telemetry protocol

To focus an US beam using a linear array to a point in space, time delays are provided to each element of the array. Reversing this principle, when a phased array of ultrasound transducers receives ultrasound waves from a point source, each element of the array senses these signals at different moments in time [17]. Using this principle, the location of the source can be estimated from the delays of the signal scattered back from that source. The time reversal beamforming algorithm consists of three main steps:

1. **First US transmit**. A plane wave or focused beam is transmitted in the medium containing the RX. (Figure 5.7(a) shows the case of a plane wave).

2. **Backscattered signal acquisition**. The transmitted US wave reflects on the surface of the RX, which (usually) has a higher reflection coefficient than the surrounding medium. The backscattered signal is then acquired by each of the elements of the TX array. Time reversal would simply involve inverting the measured time delays and applying them to each TX element. With phase reversal, the maximum of the cross-correlation between the signals received by each of the TX elements is computed, to calculate the relative time delays between each element (Fig. 5.7(b)). The results presented in the following paragraphs are obtained with this second approach.

3. **Second US transmit**. The time delays calculated at the previous point are applied to the corresponding element of the TX array, and an US beam is transmitted that will be focused to the RX location (Fig. 5.7(c)).
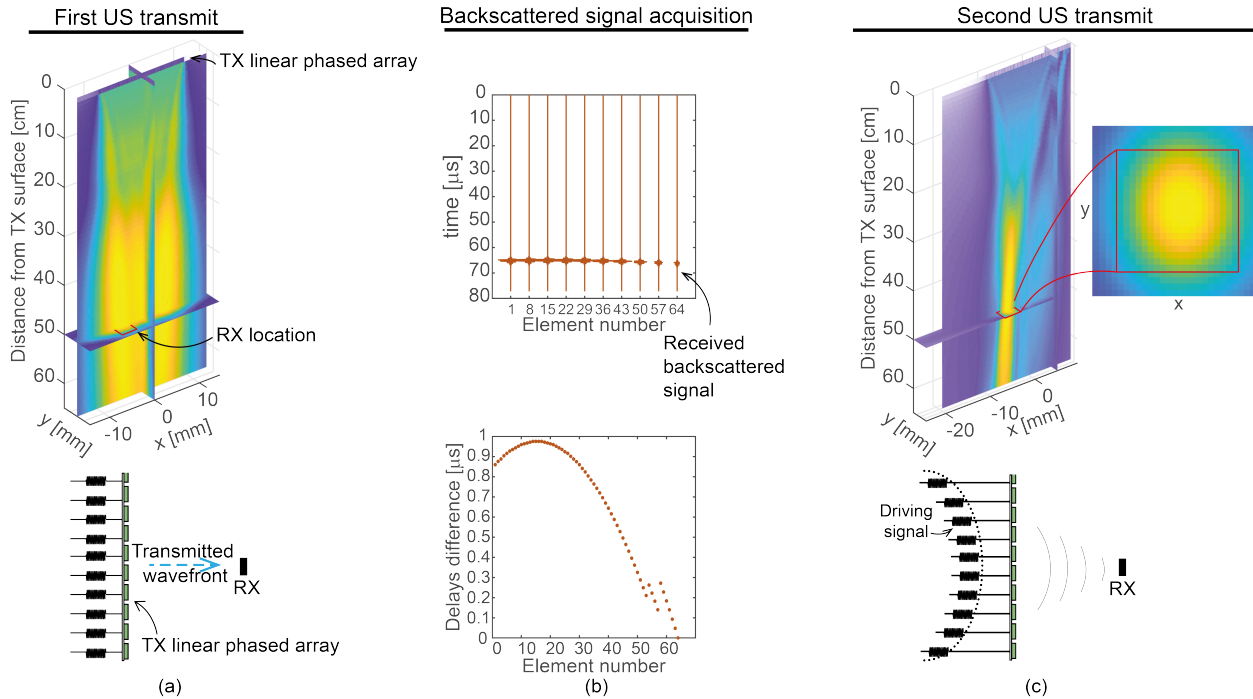
Figure 5.7.: Schematic representation and simulation example of the time reversal beamforming algorithm. (a) top plot shows the ultrasound field generated by a linear phased array TX transducer (Verasonics, P4-2v) when no time delay is applied to any of its elements, therefore generating a plane wave; at the bottom, the schematic representation of this step. (b) Top plot represents the ultrasound RF signals scattered back from the RX in the medium, and recorded by the TX elements. The RX has a lateral misalignment of 5 mm in the x direction with respect to the centre of the field, also visible in (a). Bottom plot shows the difference in arrival time of the backscattered signal for each of the TX elements obtained from the cross-correlation between the signals. (c) The top plot is the US field generated by the TX transducer when the delays in (b) are fed to the corresponding element. The beam precisely focuses to the RX location, as shown in the figure expansion on the right. The bottom plot is the schematic representation of this step.

Strengths and Limitations of the method

To understand its capabilities and limitations, we simulated the time reversal method using MUST, a Matlab ultrasound toolbox [18]. A 64-element linear phased array already implemented in the toolbox was used as TX, as its characteristics in terms of centre frequency and size are in line with the ones used to obtain the results in the previous sections [19, 20]. Specifically, the Verasonics probe P4-2v, with 2.7 MHz centre frequency, and $50 - 70$ mm elevation focus [21]. The dimensions of the TX elements are 0.25 mm $\times 14$ mm, and 50μm kerf. Squared receivers, with sizes ranging from 1×1 mm^2 to 10×10 mm^2 were simulated, and the harvestable power computed for various misalignment scenarios. Water was used as the medium for the simulations.

The results of the simulations are presented in Fig. 5.8, where the performance of phase reversal beamforming and traditional beamforming is compared in terms of harvestable power at the RX with respect to lateral misalignment. Here phase reversal begins with a plane wave and assumes no prior knowledge of the RX position. Traditional beamforming is performed by applying the correct delays to each of the TX elements assuming the position of the RX is known. In each of the subplots in Fig. 5.8, the performance is compared for different frequencies and RX size, also expressed in terms of RX lateral size to TX total width (the largest of the two TX dimensions) ratio. As seen in Section 5.5.2, the effect of partitioning the RX on the harvestable power depends on the dimension of the partition in terms of number of wavelengths, as frequency is the determining variable. Therefore, here the ratio RX/TX size, which is dimensionless, was expressed in terms of number of wavelengths to capture the effect of the frequency (RX/(TX$\cdot \lambda$)). The ratio would otherwise be the same for any tested frequency.

The figure shows that, for RX/TX size ratios smaller than 100λ, the performance of phase reversal beamforming and traditional focusing is comparable at different frequencies, allowing to achieve approximately the same amount of power between the two methods in the range of simulated conditions. On the other hand, for RX/TX size ratios larger than 100λ, the harvestable power at the RX computed with the two beamforming methods starts to deviate from each other, with larger discrepancies for larger RX/TX size ratios.

In addition, the harvestable power achievable with the traditional focusing is not proportional to the RX size. Specifically, the harvestable power for a RX/TX size ratio larger than 300λ is generally lower than for smaller ones. This is expected since the diameter of the beam at the RX, which is the focus location, is a few mm wide, defined by the frequency and the TX dimensions, and therefore fixed. Thus, when the size of the RX exceeds
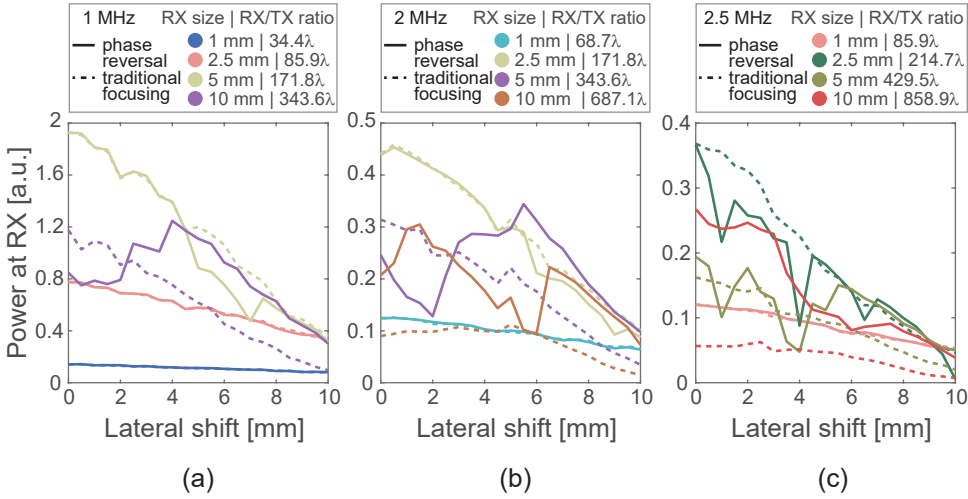
Figure 5.8.: Comparison of time reversal beamforming and traditional beamforming (e.g. delay-and-sum beamforming) simulations with respect to harvestable power at the RX, in case of lateral misalignment. Results are computed for several RX sizes, which are also expresses in terms of RX lateral size to TX width ratio in wavelengths λ. TX width is constant across the plots, and measures 18.9 mm. Each plot presents the data for the tested frequencies, respectively (a) 1 MHz, (b) 2 MHz, and (c) 2.5 MHz.

the diameter of the beam, the available power will be only slightly higher, however averaged across a larger area. Also the harvestable power achievable with phase reversal beamforming for a RX/TX size ratio larger than 300λ does not follow a regular trend, and it irregularly fluctuates above and below the values obtained with the traditional focusing. These results suggests that phase reversal beamforming is less suitable for larger RX size. However, for a small RX, the two methods have equivalent and consistent performance at various frequencies, proving that phase reversal beamforming can be used as an alternative to the other beamforming methods, having the advantage of not relying on the knowledge of the RX location, compared to the other ones.

5.5.4. PHASE REVERSAL BEAMFORMING IN ACTION

The phase reversal algorithm was implemented as part of a passive tracking algorithm that uses the backscattered signal from a pre-charged CMUT array that makes use of load modulation to provide feedback on the RX location. The telemetry circuit used here is shown in Fig. 5.9 and is based on prior work [22].
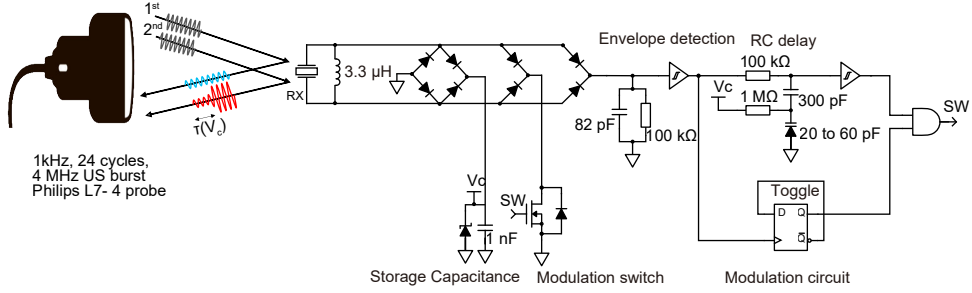
Figure 5.9.: Telemetry circuit used to track the RX. The voltage on the storage capacitance is encoded in the pulse width of the backscattered signal.

Experimental setup

The experimental setup (Fig. 5.10) used to validate the protocol consists of a linear phased array TX (Philips, L7-4 linear probe), the pre-charged CMUT (RX), a load modulation circuit, and a gel phantom (Rayher Hobby GmbH). The TX consist of 128 elements of size 7 mm × 0.28 mm and a 25 µm kerf. It is connected to a Verasonics ultrasound research platform, which allows programming the ultrasound parameters and access to raw ultrasound data using Matlab. The RX is a pre-charged collapse-mode CMUT array of size 0.84 mm × 7.4 mm. A gel phantom made of 95 % paraffin oil and 5 % organic constituents is used as medium between the TX and RX to mimic the ultrasound propagation in human tissue [23]. The RX is connected to a load modulation circuit which modulates the signal backscattered by the RX every other incoming ultrasound burst with a time delay proportional to the voltage on a storage capacitor. This, in turn, is proportional to the amount of energy received by the CMUT. More details on the implementation of the load modulation circuit can be found in [22].

Tracking algorithm

A region of interest (ROI), which contains the target (RX), and a coordinate system are defined. Two consecutive ultrasound bursts of 24 cycles with a frequency of 4 MHz and a pulse repetition frequency of 500 Hz are sent by the TX and focused onto a point of the coordinate system. These bursts are subsequently scattered back by the RX and the surrounding area, and their pulse width modulation is evaluated by computing the envelope of the differential signal. Figure 5.11(a) shows an example of two consecutive backscattered signals received by the TX. These signals often exhibit distortion due to reflections and scattering within the phantom, making modulation
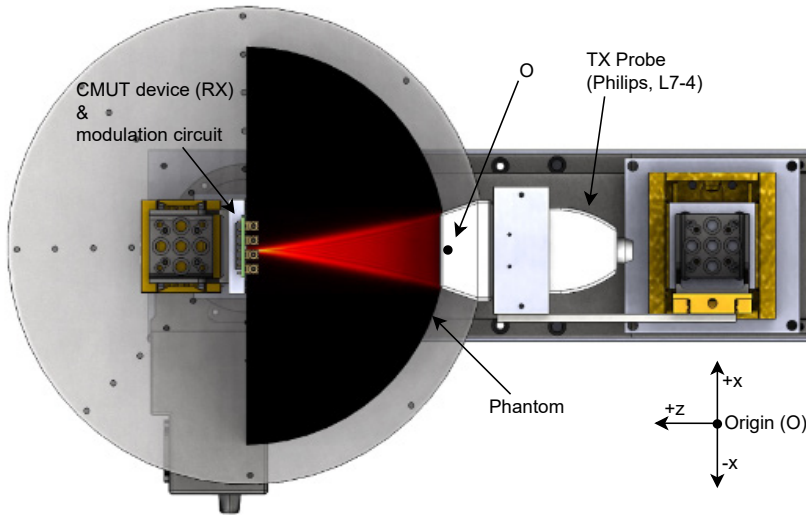
Figure 5.10.: Schematic of the experimental setup.

detection challenging, as the signals tend to overlap significantly. However, computing the differential signal and its envelope allows to determine if the signal has been modulated and, most importantly, it rejects common-mode interference and low-frequency artefacts, making this method robust.

In the event of no observed modulation, the focal point is shifted to the next location within the coordinate system. If modulation is detected, the delays associated with the modulated bursts received by each TX channel are identified by calculating the cross-correlation in relation to a reference TX channel. This step corresponds to the implementation of the phase reversal technique, which is particularly effective due to the sharp rising edge of the differential signal. To focus on a single point, the delays associated with each TX channel must follow a 2nd order relationship, therefore they are fitted with a parabolic curve (Fig. 5.7(b)).

Subsequently, the residuals of this fitting are calculated, and, if the deviation between the fitting and the measured delays is less than 8 % (empirically determined), the curve is inverted, and the time delays are applied to each TX channel (as shown in Fig. 5.7(c)). This ensures that the ultrasound is accurately focused on the active RX region. In case the deviation exceeds 8 %, the fitting is discarded, and the TX focus is moved to the next coordinate point.
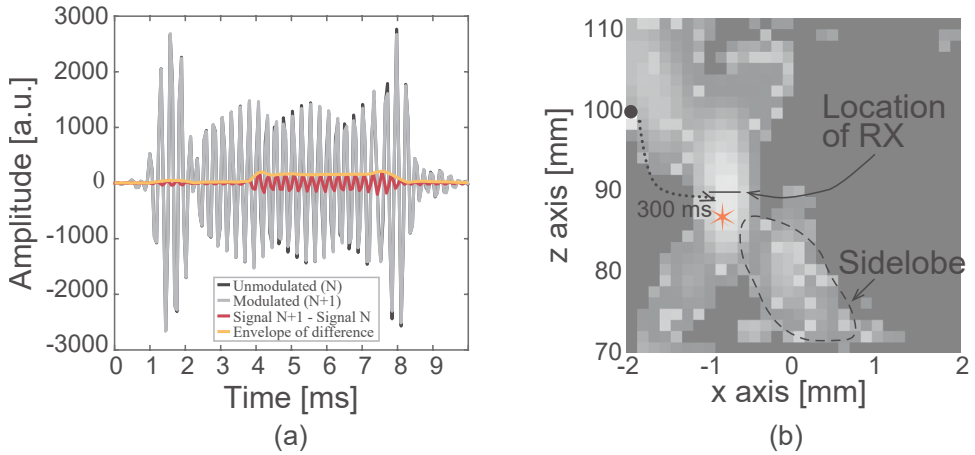
Figure 5.11.: (a) Example of modulated and unmodulated backscattered signals received by the TX, together with the differential signal and its envelope. (b) Reference heatmap obtained with traditional scanning of the ROI. The brightest regions indicate points where modulation of the backscattered signal is detected, and the brightness is proportional to the power at the RX. The RX is placed approximately around coordinate (-1, 90). The black dot is the point of the first modulation and good delays fitting. It takes about 300 ms from this point to focus on the receiver location.

Focusing on the receiver

Figure 5.11(b) shows the heatmap generated by scanning the entire ROI. The ROI is composed of 30×30 pixels and is obtained with traditional scanning, which takes approximately 3 minutes for a region of this size. In this figure, the brighter areas indicate the points in which modulation is observed, and the brightness is proportional to the pulse width of the backscattered signal modulated by the load modulation circuit, and therefore proportional to the received power. The brightest region, approximately at coordinate (-1, 90), corresponds to the location of the RX.

Using the phase reversal tracking algorithm, the location of the RX was found within 300 ms after the first modulation was detected (black dot in Fig. 5.11(b)), and a good fitting of the delays was obtained, independently of the RX location. The overall system's processing delay, including data transfer from the Verasonics hardware sequencer to the Matlab environment on the host computer where the tracking algorithm runs, amounts to about 300 ms. This delay can be reduced by implementing the algorithm on dedicated hardware, such as an FPGA or a GPU-based system.

Furthermore, since the search for the position of the RX is essentially a search for the maximum of the pulse width modulation, it can be assumed

that other maximum search algorithms can be used. A 2-D binary search [24] and a method based on the trailing of the increase in the pulse width were implemented as a comparison. The latter method consists of scanning a small area of the heatmap and, depending on which sub-section of this area has longer pulse widths, therefore a higher received power, the scanning area is shifted towards that direction at the next iteration until reaching the (local) point of maximum received power. However, both these methods failed to find the location of the RX because the heatmap often contains side lobes, as it can be seen in Fig. 5.11(b), which function as local maxima and are therefore identified by the two search methods as the location of the receiver. On the other hand, the phase reversal algorithm was faster and robust enough to correctly locate the receiver.

Ultimately, generating the heatmap for the ROI is not a prerequisite for localising the implant using the phase reversal method. Although it was used here as a reference to validate the algorithm's precision and to compare the speed of the two methods, it is not essential.

TRACKING A MOVING RX

Once the RX has been located, the link between the TX and the RX must be maintained and be able to compensate for small movements. To test this, the RX was mounted on a 3D motorised stage and submerged in a water tank at about 130 mm from the TX (Fig. 5.12). For this experiment, water was used as
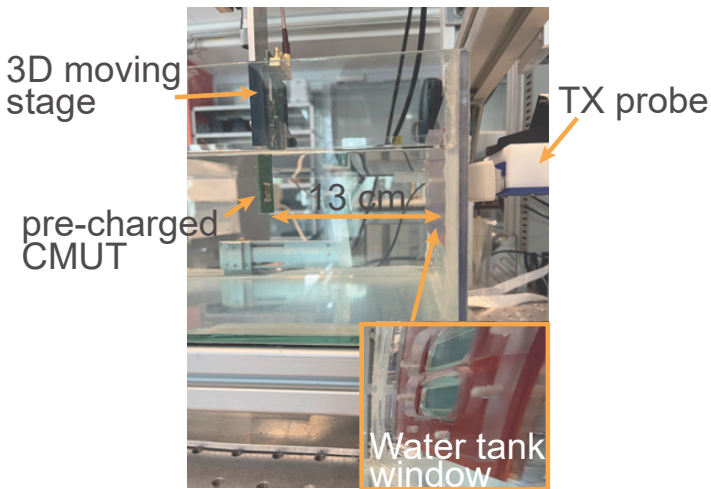
Figure 5.12.: Experimental setup used to track the moving RX.

a medium because the gel phantom does not allow the RX to move in 3D. The
water tank has a window made of a 30 μm thick PET foil to allow interfacing
the TX from outside of the tank. The motorised stage was programmed to
move at a constant speed between −2 mm and 2 mm in the x direction with
respect to the initial position of the RX in space. The initial speed of the RX
was set to 0.2 mm/s and it was increased after successfully tracking the target
(RX). An example video was recorded during one of the experiments and is
available at [25]. The maximum speed at which reliable tracking of the RX
was achieved was 1 mm/s, and also in this case, is limited by the Verasonics
system as explained in the previous paragraphs.

5.5.5. Combining a RX array and a TX array

Seen the benefits of using either a RX array or a TX array demonstrated in
the previous sections, a fourth mitigation strategy consisting of a combination
of the two previous ones was evaluated. The Verasonics P4-2v linear phased
array was used as TX and the performance was evaluated at 1 MHz and
2.5 MHz for a 5×5 mm^2 RX. Phase reversal beamforming was used for these
simulations.
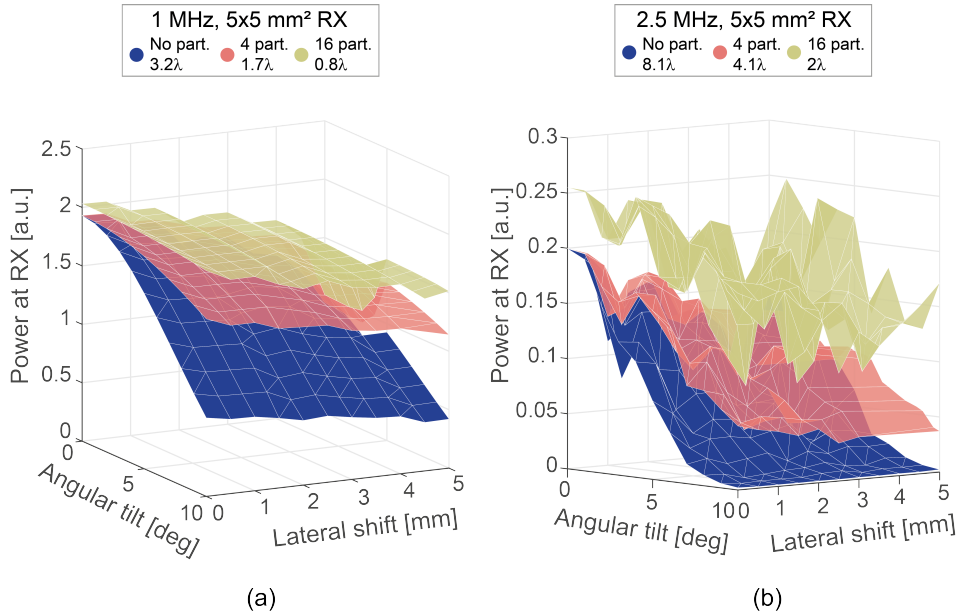
Figure 5.13.: Simulation results of harvestable power obtained by using the P4-2v linear
phased array TX and a 5×5 mm^2 RX subdivided in different number of partitions at (a)
1 MHz and (b) 2.5 MHz.

In Fig. 5.13 the improvement in harvestable power at the RX due to its partitioning is compared to a single element (no partition). It can be observed that RX partitioning has more effects in compensating the angular misalignment compared to lateral misalignments. In fact, looking at the results achieved with 16 partitions, the effect of angular misalignment is almost neutralised. Furthermore, the improvement in harvested power in the presence of lateral shift is mostly compensated by using a TX array with a beamforming algorithm, in this case phase reversal, which can detect the position of the RX and correctly focus the beam to it. In fact, for different lateral shifts, the power at the RX is nearly constant for the same angular tilt. In addition, the irregular surfaces in Fig. 5.13(b) are due to the fact that the ratio RX size to TX lateral dimension is larger than 300λ, as explained earlier in this chapter, suggesting that possibly other methods than phase reversal would better perform in this case.

5.6. CONCLUSION

In this chapter, the feasibility of transferring power to a receiving transducer using ultrasound was presented, addressing the effects of lateral and angular misalignment that are likely to happen in a real case scenario. It was shown that, in case the TX transducer is a single element, the effect of lateral misalignment depends on its diameter, and that angular misalignment can significantly degrade the harvestable power even for small tilts, especially for receivers larger than a few mm^2. Three main solutions have been proposed to address the misalignment effects.

The simplest, and overall valid, is to decrease the frequency. However, the choice of transducers, whether bulk PZT or micromachined transducers, introduces certain challenges. When dealing with a PZT crystal, decreasing the frequency results in an increase in thickness, making the device more bulky. On the other hand, for micromachined transducers like CMUTs, lowering the frequency leads to a larger membrane diameter, bringing challenges in the fabrication process. Additionally, by decreasing the frequency, the focusing ability will decrease, as the wavelength becomes larger, causing loss of power in the medium for small RX and increasing the risk of possible damage to the surrounding tissue. On the other hand, lowering the frequency contributes to a reduction in energy losses in soft tissue, given that these losses are approximately $0.6\,\mathrm{dB/(cm\,MHz)}$ and are inversely proportional to frequency.

The second proposed solution is to partition the RX transducer. It was shown that the size, measured in wavelengths, of each partition determines the improvement in harvestable power. However, it is essential to note

that a higher number of partitions increases the complexity associated with the device's circuitry and packaging. This solution is most beneficial if micromachined transducers are used, as their flexibility in design and fabrication allows for different shapes and partition sizes to be manufactured much more easily compared to PZT elements, for which this solution would be more challenging to implement.

The third solution is to use a linear or matrix array TX transducer and use a beamforming algorithm to focus the beam to the RX. Here the contribution was to use the phase reversal method to track the RX. It was shown that the algorithm's performance is comparable to conventional focusing, although it may not be the optimal choice for larger RX sizes. This suggests that alternative beamforming algorithms might be more suitable in such cases. The phase reversal algorithm was successfully implemented and tested in experiments, demonstrating its capacity to reliably track a RX moving at speeds of up to 1 mm/s. It is important to note, however, that employing an array TX with a beamforming algorithm necessitates a sophisticated driving system with high computational power and speed. This complexity can pose challenges in creating a portable solution, particularly for applications such as at-home use.

Ultimately, the improvement in harvestable power was evaluated by integrating all the proposed solutions. It was shown that the combination of these solutions effectively mitigates the effects of both angular and lateral misalignments in the analysed cases.

In this chapter, several potential scenarios for ultrasonic power transfer were explored and analysed. Nonetheless, different choices in terms of shape and dimensions of the TX and RX transducers are possible and should be evaluated for the desired application. It was shown that a drawback of ultrasonic power transfer lies in its susceptibility to misalignment. However, it was demonstrated that appropriate selections in terms of TX and RX geometry, along with precise driving conditions, can effectively compensate for this sensitivity. This highlights the importance of conducting a thorough optimisation study to identify the optimal trade-offs among factors such as frequency, geometry, number of partitions, system complexity, and acceptable power loss. Such a study becomes essential for achieving the desired performance in ultrasonic power transfer applications.

REFERENCES

[1]   M. Saccher, A. Rashidi, A. S. Savoia, V. Giagka, and R. Dekker. "Phase Distribution Efficiency of cm-Scale Ultrasonically Powered Receivers". In: *2023 IEEE International Ultrasonics Symposium (IUS)*. 2023, pp. 1–4.

[2] M. Saccher, S. S. Lolla, S. Kawasaki, and R. Dekker. "Time-efficient low power time/phase-reversal beamforming for the tracking of ultrasound implantable devices". In: *2022 IEEE International Ultrasonics Symposium (IUS)*. IEEE.

[3] C. Shi, V. Andino-Pavlovsky, S. A. Lee, T. Costa, J. Elloian, E. E. Konofagou, and K. L. Shepard. "Application of a sub–0.1-mm^3 implantable mote for in vivo real-time wireless temperature sensing". In: *Sci Adv* 7.19 (2021).

[4] A. Rashidi, N. Yazdani, and A. M. Sodagar. "Fully implantable, multi-channel microstimulator with tracking supply ribbon, multi-output charge pump and energy recovery". In: *IET Circuits, Devices & Systems* 15.2 (2021), pp. 104–120.

[5] A. Rashidi, M. Zamani, T. Mondal, S. Hosseini, K. Laursen, B. Corbett, and F. Moradi. "Ultrasonically Powered and Controlled Microsystem for Dual-Wavelength Optogenetics With a Multiload Regulation Scheme". In: *IEEE Solid-State Circuits Letters* 6 (2023), pp. 33–36.

[6] J. Charthad *et al.* "A mm-Sized Wireless Implantable Device for Electrical Stimulation of Peripheral Nerves". In: *IEEE Transactions on Biomedical Circuits and Systems* 12.2 (2018), pp. 257–270.

[7] S. Hosseini, K. Laursen, A. Rashidi, T. Mondal, B. Corbett, and F. Moradi. "S-MRUT: Sectored-Multiring Ultrasonic Transducer for Selective Powering of Brain Implants". In: *IEEE Transactions on Ultrasonics, Ferroelectrics, and Frequency Control* 68.1 (2021), pp. 191–200.

[8] H. Rivandi and T. L. Costa. "A 2D Ultrasound Phased-Array Transmitter ASIC for High-Frequency US Stimulation and Powering". In: *IEEE Transactions on Biomedical Circuits and Systems* (2023), pp. 1–12.

[9] L. Tacchetti, W. A. Serdijn, and V. Giagka. "An Ultrasonically Powered and Controlled Ultra-High-Frequency Biphasic Electrical Neurostimulator". In: *2018 IEEE Biomedical Circuits and Systems Conference (BioCAS)*. IEEE, Oct. 2018.

[10] O.-Y. Wong, D. Tabruyn, V. Rochus, and N. Van Helleputte. "An Implantable Power Extraction Circuit with Integrated PMUTs for Wireless Power Delivery". In: *ESSCIRC 2022- IEEE 48th European Solid State Circuits Conference (ESSCIRC)*. 2022, pp. 217–220.

[11] T. Zhang *et al.* "Piezoelectric ultrasound energy-harvesting device for deep brain stimulation and analgesia applications". In: *Science Advances* 8.15 (Apr. 2022).

[12] *FOCUS*. Web Page. URL: https://www.egr.msu.edu/~fultras-web/.

[13] Olympus. *Ultrasonic Transducers Technical Notes*. Tech. rep. Olympus NDT, 2011.

[14] B. Khuri-Yakub and O. Oralkan. "Energy harvesting". US9774277B2. 2017.

[15] G. Shafiq and K. C. Veluvolu. "Surface chest motion decomposition for cardiovascular monitoring". In: *Scientific reports* 4.1 (2014), pp. 1–9.

[16] T. D. Than, G. Alici, H. Zhou, and W. Li. "A Review of Localization Systems for Robotic Endoscopic Capsules". In: *IEEE Transactions on Biomedical Engineering* 59.9 (2012), pp. 2387–2399.

[17] O. T. Von Ramm and S. W. Smith. "Beam Steering with Linear Arrays". In: *IEEE Transactions on Biomedical Engineering* BME-30.8 (1983), pp. 438–452.

[18] D. Garcia. "Make the most of MUST, an open-source Matlab UltraSound Toolbox". In: *2021 IEEE International Ultrasonics Symposium (IUS)*. IEEE, 2021.

5

[19]   *MUST - Matlab Ultrasound Toolbox*. Web Page. URL: https://www.biomecardio.com/MUST/index.html.

[20]   D. Garcia. "SIMUS: An open-source simulator for medical ultrasound imaging. Part I: Theory & examples". In: *Computer Methods and Programs in Biomedicine* 218 (2022), p. 106726.

[21]   *Verasonics transducers*. Web Page. URL: https://verasonics.com/verasonics-transducers/.

[22]   S. Kawasaki, I. Subramaniam, M. Saccher, and R. Dekker. "A microwatt telemetry protocol for targeting deep implants". In: *2021 IEEE International Ultrasonics Symposium (IUS)*. IEEE.

[23]   Y. Westhoek. "Ultrasound Energy Transfer using Charged CMUTs". Manuscript. Delft University of Technology, 2020. URL: http://resolver.tudelft.nl/uuid:74a07486-73c2-4457-8261-7161acb46c60.

[24]   A. Lin. "Binary search algorithm". In: *WikiJournal of Science* 2.1 (2019), pp. 1–13.

[25]   M. Saccher, S. S. Lolla, S. Kawasaki, and R. Dekker. *Video recording associated with the publication: Time-efficient low power time/phase-reversal beamforming for the tracking of ultrasound implantable devices*. 2022. URL: https://data.4tu.nl/articles/dataset/Video_recording_associated_with_the_publication_Time-efficient_low_power_time_phase-reversal_beamforming_for_the_tracking_of_ultrasound_implantable_devices/21081937/1.

5

6

ULTRASONIC POWER TRANSFER WITH PRE-CHARGED CMUTS

This chapter is based on:

- M. Saccher, R. Van Schaijk, S. Kawasaki, J. H. Klootwijk, A. Rashidi, V. Giagka, A. S. Savoia, and R. Dekker. "A Comparative Study of Si_3N_4 and Al_2O_3 as Dielectric Materials for Pre-Charged Collapse-Mode CMUTs". In: *2023 IEEE International Ultrasonics Symposium (IUS)*. 2023, pp. 1–4

6.1. INTRODUCTION

The use of implantable medical devices (IMDs) to monitor human health and treat diseases is rapidly growing, due to the progress in technology for miniaturisation and more efficient electronics. There is, in addition, a growing interest in moving away from battery powered devices towards wirelessly powered sources, reducing or eliminating the need for an intervention for battery replacement over time. IMDs require on average between tens of µW up to few hundreds of mW of power, for the most power-hungry devices [2]. Wireless power methods include inductive coupling, RF power transfer, and ultrasound power transfer [3]. Compared to inductive coupling and RF, ultrasound can deliver high power levels at large implantation depths ($> 5\,\text{cm}$), due to its short wavelength and low attenuation in the body ($0.6\,\text{dB/(cm\,MHz)}$). In addition, the FDA limit for safe use in the body is $720\,\text{mW/cm}^2$, which is more then enough to power an IMD, considering that IMD sizes range from a few mm^2 to a few cm^2.
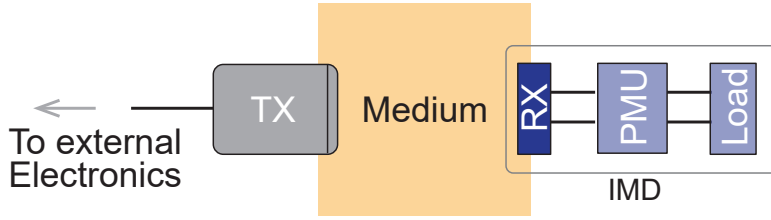
Figure 6.1.: Schematic of an ultrasonically powered implantable medical device.

An ultrasonically powered IMD platform is composed of five main components: the transmitting transducer (TX), the medium, the receiving transducer (RX), the power management unit (PMU), and the load (Fig. 6.1). It goes without saying that one of the key metrics to evaluate the platform performance is its efficiency, and most importantly the efficiency of the IMD itself, which results from the combined efficiencies of RX, PMU and load. In this chapter, the focus is on the efficiency of the RX, and specifically the acoustic-to-electrical power conversion efficiency.

In most of the research on ultrasonically powered IMDs, the ultrasonic receivers are based on PZT (Lead Zirconate Titanate) crystals. They offer moderate acoustic-to-electrical power conversion efficiencies, mainly due to their high electromechanical coupling coefficient [18, 19]. An example is the work of Chartad et al. [11] who built an IMD system including a PZT RX with an efficiency above 60 %. Results achieved by other groups are summarised in Table 6.1, showing RX efficiencies ranging from 2 % to 50 %. Nevertheless, despite their high efficiency, PZT is not biocompatible nor CMOS-compatible,

Ref.	Material	Topology	Dimensions	Thickness	Frequency [MHz]	P_{in}[mW]	Efficiency
[4]	PZT	disk	25 mm diameter	-	0.84	62.5	25 %
[5]	PZT	disk	30 mm diameter	2 mm	1	2.1	20 %
[6]	PZT	rectangular	2×4 mm^2	2 mm	1.15	12	2.7 %
[7]	PZT	disk	6.8 mm diameter	0.75 mm	2.8	-	36.7 %
[8]	PZT	disk	15 mm diameter	3 mm	0.673	1000	27 %
[9]	PZT	disk	41.36 mm^2	-	1.2	-	50.4 %
[10]	PZT	block	1.7 mm^3	-	1	0.065	3.4 %
[11]	PZT	rectangular	1×1 mm^2	1.4 mm	1.3	0.6	63 %
[12]	AlN PMUT	rectangular array	8×8 mm	300 μm	2	0.001	-
[13]	AlN PMUT	disk	200×200 μm^2		1.7	0.085	0.12 %
[14]	AlN PMUT	rectangular array	2.5 mm^2	7.45 μm	3	0.019	0.236 %
[15]	PZT PMUT	rectangular array	2.058 mm^2		0.37	0.059	0.375 %
[16]	PZT PMUT	rectangular	2×2 mm^2	40 μm	0.088	0.7	0.33 %
[17]	AlScN PMUT	disk	12.25 mm^2	0.5 μm	0.7	1	8.1 %

Table 6.1.: Summary of ultrasonic receivers performance achieved by other groups.

and miniaturisation is limited by its intrinsic properties. In fact, the thickness of the crystal is inversely proportional to its resonant frequency. In addition, by increasing the frequency, the energy losses due to absorption in the medium increase.

Alternatively, PMUTs (Piezoelectric Micromachined Ultrasonic Transducers) or CMUTs can be used. They are CMOS compatible, can be miniaturised and made biocompatible. However, regardless of these advantages, only a few studies investigated the use of MUTs as RX, with the majority using PMUTs, as summarised in the bottom half of Table 6.1. This is most probably due to the difficulty in having access to MUT devices compared to off-the-shelf PZT crystals used in most of the studies. The results in Table 6.1 show that they all suffer from low efficiency, which is mainly due to the low electromechanical coupling coefficient [16]. An exception is the work of Herrera et al. [17] in which, by doping the piezoelectric layer with Scandium, the PMUT efficiency reached 8 %. Yet, except from our prior work [20], no study was found using CMUTs. In fact, standard CMUTs require a (high) external DC bias for efficient operation, which makes the standard devices not suitable for in-body applications, making bias-free or pre-charged devices the only suitable candidates.

In Table 6.1, the acoustic power received by the RX is also reported. However, it should be pointed out that the values depend on the output power generated by the TX transducer used in the experiment, which is not the same among the reported studies. The most important metric is therefore the efficiency.

In this chapter, the power conversion efficiency of the pre-charged collapse-mode CMUTs is evaluated through ultrasonic power transfer experiments. The performance was evaluated in water, and standard commercial transducers were used as transmitters (TX). The performance was evaluated at two test frequencies - 1 MHz, and 2.5 MHz - and for two sizes of the receiver: $5 \times 5\,mm^2$ and $20 \times 20\,mm^2$, with the latter evaluated also in its partitioned form.

6.2. CHOICE OF TX TRANSDUCER

For the power transfer experiments, commercial single element circular piston TX transducers were used. FOCUS [21] was used to determine the best TX diameter with respect to the size of the RX, and the distance between TX and RX. For convenience, the power transfer experiment was performed in water, therefore water was also used as a medium for the simulations. In water, the ultrasound attenuation is negligible $(0.002\,dB/(cm\,MHz))$. However, in a real scenario where the RX is in the body, an attenuation of $0.6\,dB/(cm\,MHz)$ must
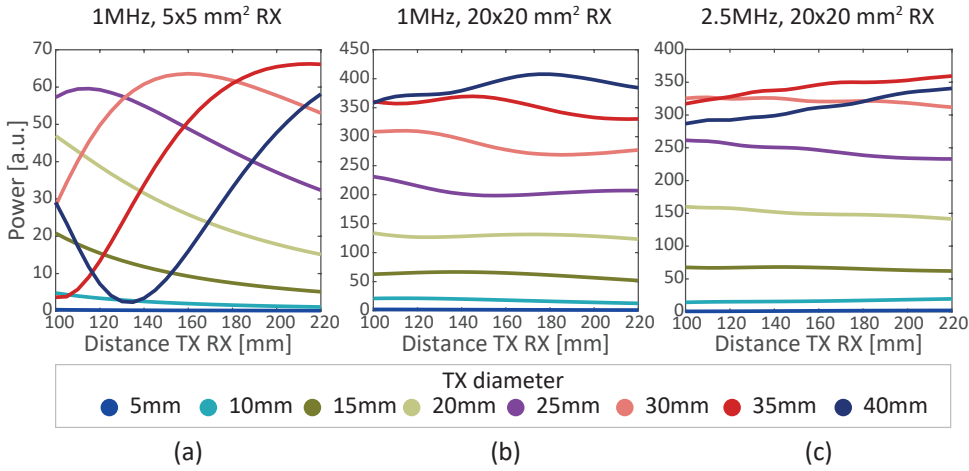
Figure 6.2.: Simulations of power at the RX for different experimental conditions to determine the best TX transducer diameter. (a) $1\,\text{MHz}$ and $5 \times 5\,\text{mm}^2$ RX; (b) same as (a) but for a $20 \times 20\,\text{mm}^2$ RX; (c) $2.5\,\text{MHz}$ and $20 \times 20\,\text{mm}^2$ RX.

be considered, and the best TX to use might be different from the one chosen here.

Three combinations were analysed, namely $5 \times 5\,\text{mm}^2$ RX at $1\,\text{MHz}$, and $20 \times 20\,\text{mm}^2$ RX both at $1\,\text{MHz}$ and $2.5\,\text{MHz}$. Two requirements were considered: distance between TX and RX around $100\,\text{mm}$, as this represent a maximum typical implantation depth of the RX, and maximum power at the RX. The input voltage to the TX was the same for all the simulated combinations, and the simulation results are shown in Fig. 6.2. The closest available commercial option from Olympus|Evident ultrasonic transducers catalogue was chosen, together with the test distances that allow for maximum power at the RX. The choices are summarised in Table 6.2.

For the $1\,\text{MHz}$, $39\,\text{mm}$ diameter, a distance of $180\,\text{mm}$ was chosen, which is almost twice the previously defined target distance between TX and RX, since the maximum power at RX is achieved at this distance (Fig. 6.2(b)) and the

Test combination	Olympus choice: Freq. and diameter	Test distance for max. power
$1\,\text{MHz}$, $5 \times 5\,\text{mm}^2$	$1\,\text{MHz}$, $25\,\text{mm}$	$110\,\text{mm}$
$1\,\text{MHz}$, $20 \times 20\,\text{mm}^2$	$1\,\text{MHz}$, $39\,\text{mm}$	$180\,\text{mm}$
$2.5\,\text{MHz}$, $20 \times 20\,\text{mm}^2$	$2.25\,\text{MHz}$, $39\,\text{mm}$	$210\,\text{mm}$

Table 6.2.: Summary of chosen TX transducers and test distance.

attenuation is negligible in water. In addition, the 2.25 MHz, 39 mm TX was chosen instead of the 35 mm option, as this last diameter was not available at the manufacturer. Similarly to the previous case, the TX was placed at 210 mm from the RX for maximum power, as this was the maximum distance allowed by the power transfer experimental setup.

6.3. ACOUSTIC CHARACTERISATION OF TX TRANSDUCER

The chosen TX transducers were then characterised by measuring their output pressure at the chosen distance for the power transfer experiment. The TX transducer under test was immersed in a tank filled with degassed water, and a needle hydrophone (2762, Precision Acoustics, UK) was used to measure
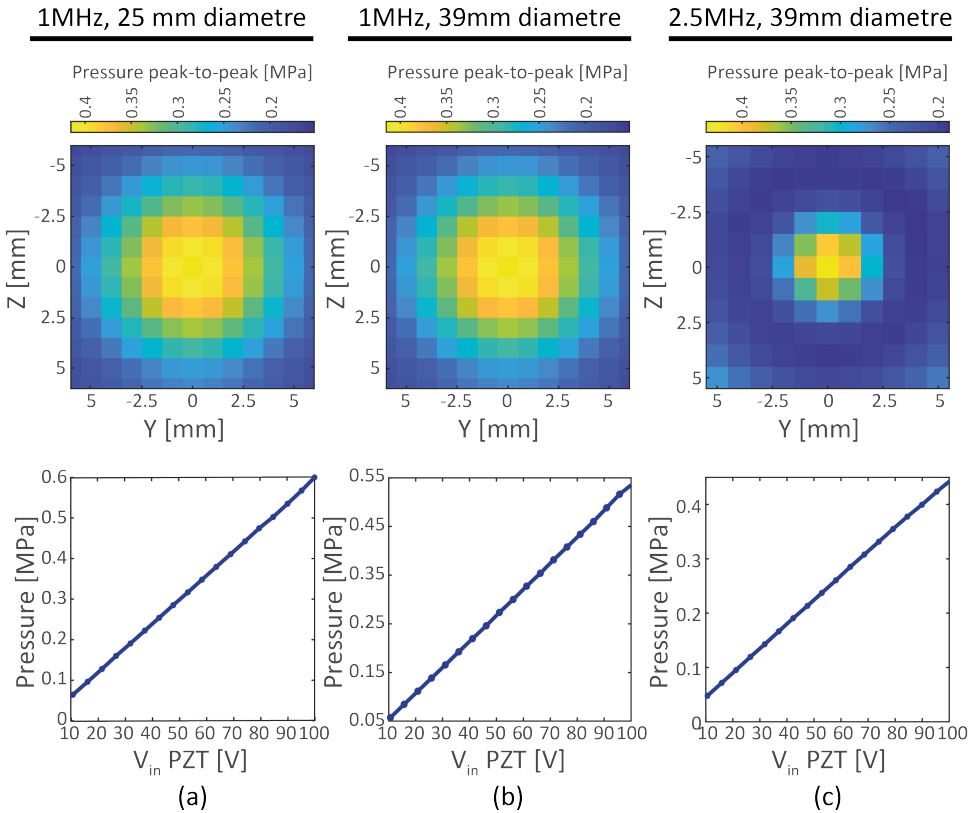
Figure 6.3.: Measured pressure profile (top row) and relationship between applied voltage and output pressure (bottom row) of the selected TX transducers. (a) 1 MHz, 25 mm diameter, measured at 110 mm. (b) 1 MHz, 39 mm diameter, measured at 180 mm. (c) 2.5 MHz, 39 mm diameter, measured at 210 mm.

the output pressure. The hydrophone was mounted on a programmable translational stage, that can be programmed to move in *x-y-z* direction. The TX was fixed on a custom holder. First, the linearity of the relationship between input voltage at the TX vs output pressure was measured at the centre of the TX, at the chosen distance. The input signal at the TX was set as a sine wave of 10 cycles, with a burst period of 10 ms, at either 1 MHz or 2.5 MHz, depending on the TX under test. The amplitude of the sine wave was swept from 10 V to 100 V, and for each voltage step the output pressure was measured by the hydrophone. The results of this measurement are depicted in the bottom row of Fig. 6.3, showing that all the three transducers have a linear relation between input voltage and output pressure in the range 10 − 100V.

Secondly, the pressure profile was mapped at the chosen distance by scanning the needle hydrophone over a plane parallel to the surface of the TX. The pressure profile generated by each of the TX is shown in Fig. 6.3, showing, as expected, a circle symmetric pressure field.

6.4. Ultrasonic power transfer experiment

For the power transfer experiment, the TX and RX were immersed in the water tank, placed at the distance at which the pressure profile was characterised, and centre aligned (Fig. 6.4). For this experiment, the $20 \times 20\,\text{mm}^2$ CMUT die composed of 16 $5 \times 5\,\text{mm}^2$ partitions was used. It was mounted on a PCB that allows accessing each of the partitions, and coated with a thin layer of PBR
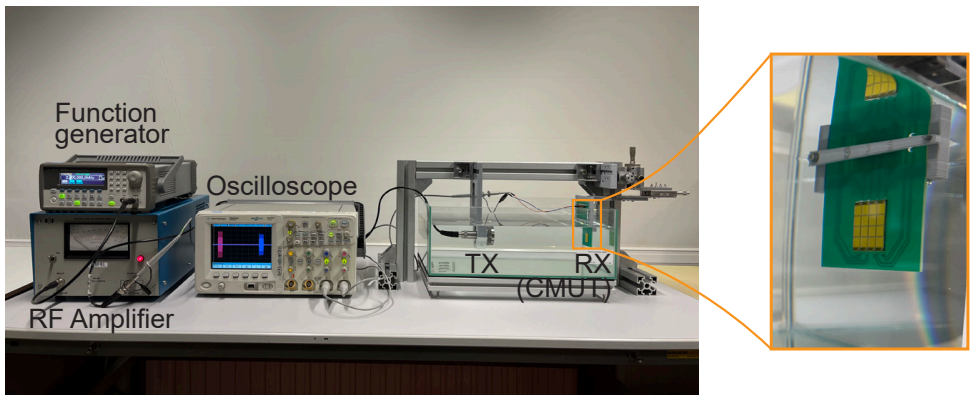
Figure 6.4.: Power transfer setup. The driving signal for the TX transducer is generated by the function generator and amplified by the RF amplifier. The oscilloscope is used to check the input signal to the TX transducer and measure the output voltage from the CMUT under test. The CMUT is attached to a custom made 3D printed holder connected to micromanipulators that allow the adjustment of the position in the *x-y-z* direction, and the angular rotation.

(polybutadiene rubber). Since the sample is symmetric on both directions, the signal received by opposite elements on the die, such as the corners, when centre aligned and parallel to the TX, has the same amplitude and phase. Therefore, the centring and alignment was done by checking the signal from the 4 opposite corner elements for phase and amplitude differences, and the position corrected until such differences were minimised. The power transfer experiment was done for each of the CMUT devices presented in Chapter 4 and the goal was to highlight potential differences in performance between transducers.

6.4.1. MAXIMUM POWER TRANSFER PRINCIPLE

CMUTs represent a two-port system, with an acoustical port (mechanical domain), and an electrical port (electrical domain). This system can be modelled and converted into an equivalent circuit in the electrical domain, which is the Butterworth-Van Dyke (BVD) equivalent circuit model of a CMUT. The model consists of a $R_m - L_m - C_m$ series (resistor-inductor-capacitor), representing respectively the mechanical components damper-mass-spring, in parallel to a capacitor C_e, representing the electrical capacitance (Fig. 6.5(a)). Other components can also be included to model parasitic elements. Here, a resistor R_s is added in series, to model the resistance of the electrical interconnects between the CMUT array and the measurements connector.

At the chosen frequency, the model can be simplified with an equivalent impedance. Here, L_m and C_m are simplified with an equivalent impedance, in series with R_m, and after a transformation between series and parallel equivalent to include the effect of C_e, the equivalent impedance becomes $Z_{eq} = R_{s_{eq}} + X_{s_{eq}}$, therefore composed of a resistor and a capacitor (as C_e dominates in the considered cases). The resistor modelling the interconnects,
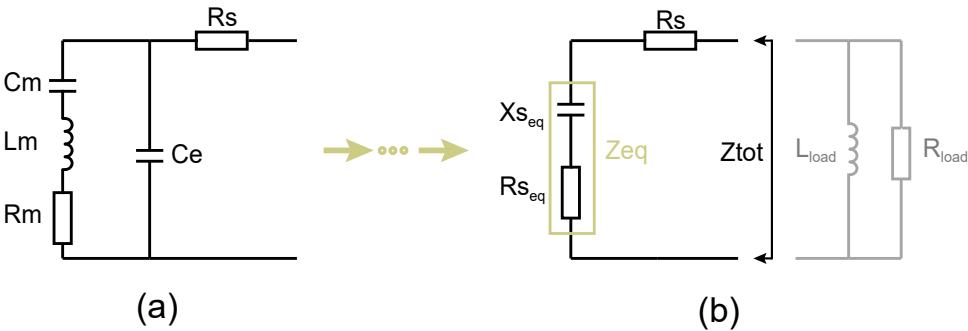
Figure 6.5.: Schematic of load matching for maximum power transfer.

R_s, is then added to the Z_{eq}, to form Z_{tot}. To maximise the power transfer efficiency, a matching network must be connected to the CMUTs. For these experiments, a parallel matching approach was chosen, where the value of the optimal load is the conjugate of the measured impedance at the carrier frequency. Therefore, the optimal load to be connected in parallel to the CMUTs, consists of an inductor (L_{load}) and a resistor (R_{load}).

To compute the values of the matching components, the impedance of the CMUTs to be tested was measured in water and fitted with the BVD model to extract the values of the components (Fig. 6.6). The best value of each matching component was then experimentally determined by testing a range of values close to the computed ones. The power at R_{load} was calculated as $P_{load} = V_{pp}^2/(8 \cdot R_{load})$, where V_{pp} is the peak-to-peak voltage at the load (R_{load}). Eventually, the acoustic-to-electrical power conversion efficiency (η), which is the ratio between the input acoustic power at the CMUT surface, and the maximum power at the load, was calculated.

It should be noted that other matching network configurations are possible, and depending on the application, one can be more suitable than another one. Here, the parallel configuration was chosen as there were no specific requirements on the load, such as a specific current, and it was the easiest to implement in this case. However, any chosen matching configuration will include an inductor to compensate the capacitive part of the CMUT impedance introduced by the large static electrical capacitance. This is because of the CMUT structure that is based on two parallel plates forming the device electrodes.

In addition, considering the potential integration of the CMUT devices into an ASIC, the requirement for a matching inductor poses a significant challenge. Therefore, the power conversion efficiency with a purely resistive load was also evaluated.

6.5. IMPACT OF BUILT-IN BIAS ON POWER CONVERSION EFFICIENCY

For this experiment, the four central partitions of the 16-partitions CMUT die were used. Each of these four partitions was charged with a different electric field, ranging from $-7.5\,\text{MV/cm}$ to $-9\,\text{MV/cm}$, to test the effect of a different built-in bias on the CMUT power conversion efficiency. By using CMUTs partitions from the same die, as in this case, the potential variability between samples taken from different locations on the fabrication wafer is reduced, allowing for a better comparison. For each of the partitions, and for each CMUT layer stack combination, the values of the BVD model components
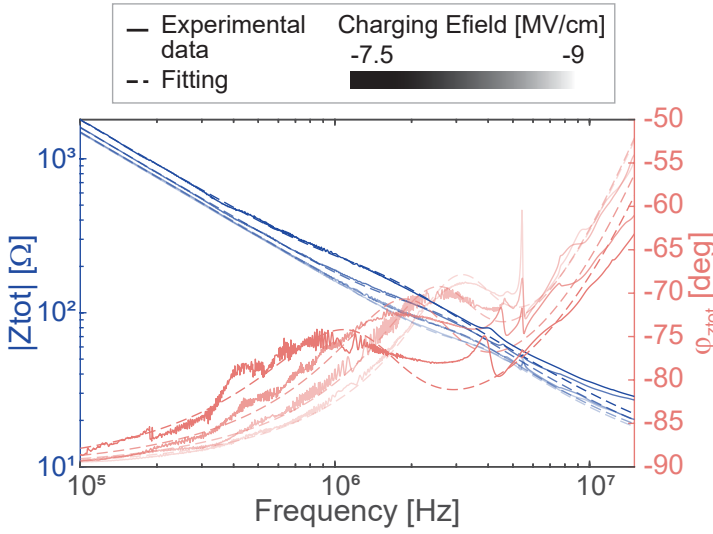
Figure 6.6.: Example of BVD model fitting to the measured impedance data for different charging electric fields.

have been extracted, and are summarised in Appendix C, Table C.1.

The power transfer experiment was done for each of the device types and charging electric fields. The TX was driven with a sine burst signal of 20 cycles and pulse repetition frequency of 10 Hz. The input acoustic pressure at the surface of each RX was 228 kPa and 197 kPa at 1 MHz and 2.5 MHz respectively, corresponding to an intensity of around 420 mW/cm^2 and 300 mW/cm^2, therefore about half of the FDA limit of 720 mW/cm^2. These values have been obtained from the acoustic characterisation of the TX transducers.

6.5.1. Optimally matched load: parallel inductor and resistor

Figure 6.7 presents the power transfer efficiency obtained from the experiments with an optimally matched load consisting of L_{load} parallel to R_{load}. From the figure we can infer that there is no absolute optimal device. However, most of the devices charged with electric fields of -7.5 and -8 MV/cm have a better performance at 1 MHz compared to 2.5 MHz. On the other hand, devices charged at -8.5 and -9 MV/cm have a better performance at 2.5 MHz compared to 1 MHz, with the ones charged at -8.5 MV/cm being the best performing ones.

This can be explained by comparing the equivalent impedance of the CMUTs Z_{eq} (Table 6.3), computed from the BVD model circuit at the test frequency, to the series resistance R_s of the CMUTs (Appendix C, Table C.1),

TEOS 120 nm

	Si$_3$N$_4$ (w223)				**Al$_2$O$_3$** (w225)			
	Charging Efield	−7.5 [MV/cm]	−8 [MV/cm]	−8.5 [MV/cm]	−9 [MV/cm]	−7.5 [MV/cm]	−8 [MV/cm]	−8.5 [MV/cm]	−9 [MV/cm]

1 MHz:

	−7.5 [MV/cm]	−8 [MV/cm]	−8.5 [MV/cm]	−9 [MV/cm]	−7.5 [MV/cm]	−8 [MV/cm]	−8.5 [MV/cm]	−9 [MV/cm]
$\mathbf{Z_{eq}} = \mathbf{Rs_{eq}} + \mathbf{iXs_{eq}}$ [Ω]	$57.2 - i208.9$	$27.7 - i170.4$	$15.8 - i155.5$	$9.3 - i151.3$	$45.4 - i212.3$	$29.6 - i166.9$	$15.6 - i149.3$	$9.9 - i141.1$
$\mathbf{L_{load}}$ **model** [µH]	36.83	28.4	25.5	24.5	36.5	28.26	24.5	22.9
$\mathbf{R_{load}}$ **model** [Ω]	706	806	916	1166	809	705	869	1004
Power [mW]	46.1	39.1	39.1	29.0	40.5	41.3	41.5	35.5
η [%]	42.9%	36.4%	36.4%	27.0%	37.7%	38.4%	38.7%	33.0%
Sensitivity [V/MPa]	44.8	36.3	30.9	22.6	39.4	38.2	31.5	24.5

2.5 MHz:

	−7.5 [MV/cm]	−8 [MV/cm]	−8.5 [MV/cm]	−9 [MV/cm]	−7.5 [MV/cm]	−8 [MV/cm]	−8.5 [MV/cm]	−9 [MV/cm]
$\mathbf{Z_{eq}} = \mathbf{Rs_{eq}} + \mathbf{iXs_{eq}}$ [Ω]	$6.2 - i105.6$	$21.4 - i88.2$	$17.8 - i70.4$	$12.6 - i62.5$	$5.3 - i97.7$	$11.1 - i85.0$	$15.1 - i68.9$	$12.4 - i59.9$
$\mathbf{L_{load}}$ **model** [µH]	6.58	6.1	5.26	4.5	6.27	5.55	5	4.36
$\mathbf{R_{load}}$ **model** [Ω]	414	268	199	191	388	286	208	180
Power [mW]	20.7	28.1	62.5	28.9	21.8	24.3	46	35.2
η [%]	27.2%	36.9%	82.0%	38.0%	28.4%	31.9%	60.4%	46.2%
Sensitivity [V/MPa]	24.3	28	36.9	25.2	19.8	23.2	31.1	26.5

TEOS 200 nm

	Si$_3$N$_4$ (w218)				**Al$_2$O$_3$** (w221)		

1 MHz:

	−7.5 [MV/cm]	−8 [MV/cm]	−8.5 [MV/cm]	−9 [MV/cm]	−7.5 [MV/cm]	−8 [MV/cm]	−8.5 [MV/cm]
Charging Efield	−7.5 [MV/cm]	−8 [MV/cm]	−8.5 [MV/cm]	−9 [MV/cm]	−7.5 [MV/cm]	−8 [MV/cm]	−8.5 [MV/cm]
$\mathbf{Z_{eq}} = \mathbf{Rs_{eq}} + \mathbf{iXs_{eq}}$ [Ω]	$59.8 - i254.7$	$34.7 - i198.6$	$18.7 - i180.7$	$11.9 - i176.8$	$34.4 - i193.6$	$25.7 - i176.7$	$11.1 - i161.8$
$\mathbf{L_{load}}$ **model** [µH]	43.7	33.3	29.59	28.6	32.63	29.2	26.2
$\mathbf{R_{load}}$ **model** [Ω]	978	889	1096	1369	838	907	1194
Power [mW]	41.4	42.7	33.8	28.5	63.1	16.6	19.7
η [%]	38.5%	39.7%	31.4%	26.5%	58.8%	15.5%	18.3%
Sensitivity [V/MPa]	42.9	41	28.9	24	55.1	22	19

2.5 MHz:

	−7.5 [MV/cm]	−8 [MV/cm]	−8.5 [MV/cm]	−9 [MV/cm]	−7.5 [MV/cm]	−8 [MV/cm]	−8.5 [MV/cm]
$\mathbf{Z_{eq}} = \mathbf{Rs_{eq}} + \mathbf{iXs_{eq}}$ [Ω]	$8.1 - i122.7$	$21.0 - i104.1$	$20.0 - i84.23$	$15.9 - i74.9$	$12.4 - i96.9$	$20.5 - i84.9$	$13.3 - i68.7$
$\mathbf{L_{load}}$ **model** [µH]	7.4	6.84	6.13	5.4	6.32	6.13	4.93
$\mathbf{R_{load}}$ **model** [Ω]	438	337	254	233	350	273	216
Power [mW]	19.9	24.6	48.8	25.2	39.6	62.1	66.0
η [%]	26.1%	32.3%	64.0%	33.1%	52.0%	81.6%	86.6%
Sensitivity [V/MPa]	23.9	26.4	35	24.7	30.3	39.2	39.4

Table 6.3.: Summary of results obtained from the ultrasonic power transfer experiments for the tested devices when optimally matched.

which ranges between 10 and 12 Ω for the tested devices. The highest power transfer efficiency is achieved when the real part of Z_{eq} is the largest. The real part of Z_{eq} is in series with the parasitic series resistance R_s, creating a voltage divider. Therefore, the bigger the real part of the equivalent impedance compared to R_s, the smaller the proportional power loss is.

In addition, the highest absolute efficiencies were achieved at 2.5 MHz. At this frequency, the reactive part of the equivalent impedance $X_{s_{eq}}$ is smaller compared to 1 MHz, therefore requiring a smaller reactive compensation. This can also be seen by looking at the phase plots in Fig. 6.6. The highest phase angle is achieved at around 2.5 MHz by devices charged with -8.5 and -9 MV/cm. In fact, in the ideal case, the ratio $X_{s_{eq}}/R_{s_{eq}}$ should tend to zero at the frequency of operation, meaning that no compensation is required for the reactive part.

Moreover, the efficiency of the matching inductor in compensating the reactive part of the equivalent impedance is affected by the presence of the parasitic resistance R_s, which is in between the two components. R_s limits the amount of reactive current flowing from the inductor towards the
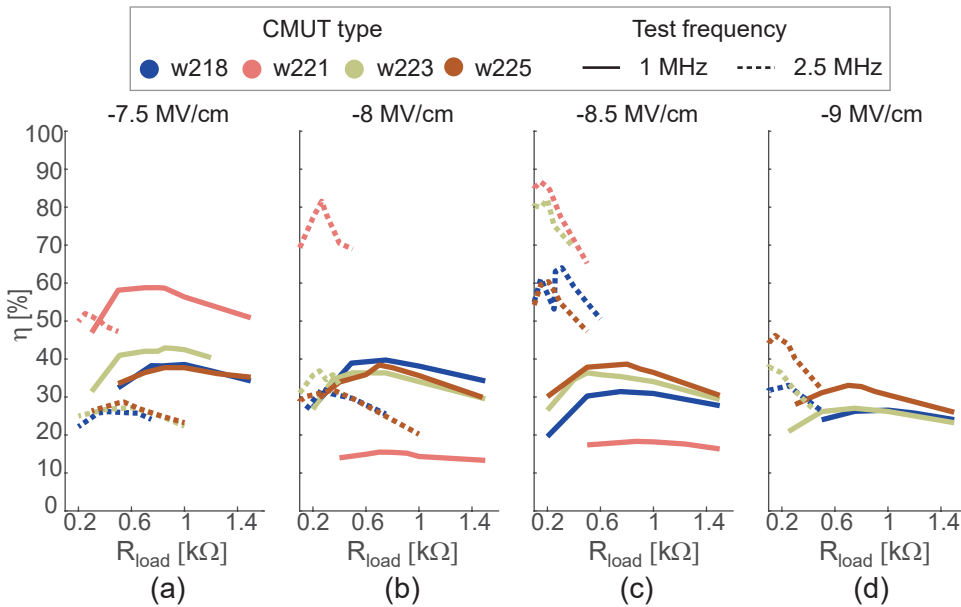
Figure 6.7.: Power transfer efficiency with optimally matched load composed of L_{load} parallel to R_{load}, at 1 MHz and 2.5 MHz. (a) Devices charged with an electric field of -7.5 MV/cm. (b) Devices charged with -8 MV/cm. (c) Devices charged with -8.5 MV/cm. (d) Devices charged with -9 MV/cm. For the meaning of CMUT type number refer to Table 6.3.

equivalent capacitor ($X_{S_{eq}}$), therefore decreasing its efficiency in compensating the capacitive part. Further to this, the matching inductor itself is not an ideal component having its own parasitic series resistance. For this experiment high quality factor inductors ($Q = 60$) were used with a maximum series resistance of $0.22\,\Omega$. However, despite the low series resistance, their compensation ability is still affected.

Ultimately, the efficiency and power at the load achieved in these experiments (Table 6.3) are superior to the performance reported by other groups (Table 6.1), highlighting the great potential of the pre-charged collapse-mode CMUTs for power receiving applications.

6.5.2. Resistive only load

The previous experiment was repeated by connecting a purely resistive load to the CMUT. The results are shown in Fig. 6.8. As for the previous experiments, no absolute optimal device can be identified, and the devices showing the highest efficiency are the same that exhibited the highest efficiency when connected to the optimally matched load. Also in these experiments, the best performance was achieved at 2.5 MHz, which corresponds to frequency
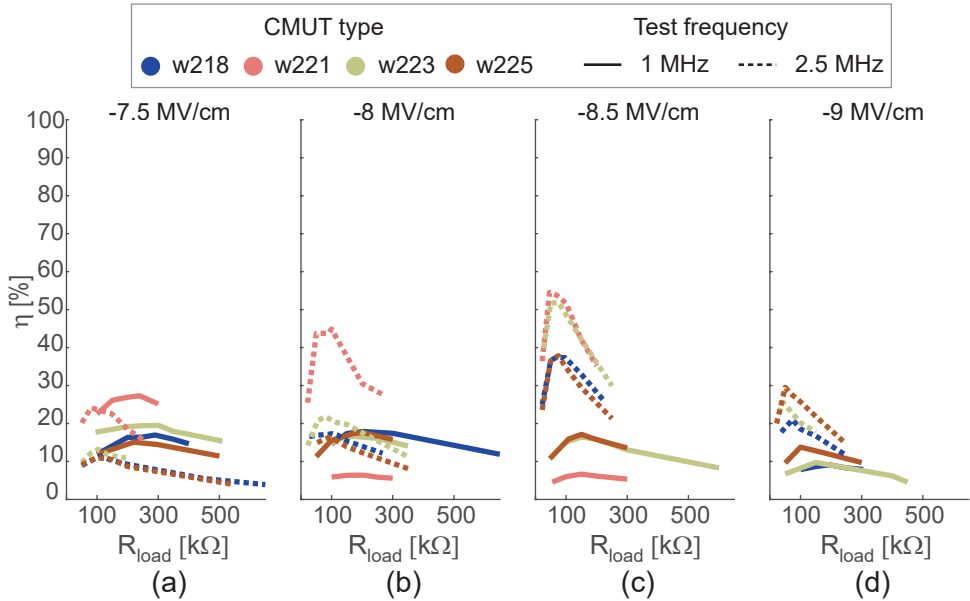
Figure 6.8.: Power transfer efficiency with resistive load, at 1 MHz and 2.5 MHz. (a) Devices charged with an electric field of $-7.5\,MV/cm$. (b) Devices charged with $-8\,MV/cm$. (c) Devices charged with $-8.5\,MV/cm$. (d) Devices charged with $-9\,MV/cm$.

		TEOS 120 nm							
		Si$_3$N$_4$ (w223)				**Al$_2$O$_3$** (w225)			
1 MHz	**Charging Efield** [MV/cm]	−7.5	−8	−8.5	−9	−7.5	−8	−8.5	−9
	Power [mW]	21	17.9	17.6	10.4	16.2	18.9	18.4	14.8
	η[%]	19.5%	16.7%	16.4%	9.7%	15.1%	17.6%	17.1%	13.8%
2.5 MHz	**Power** [mW]	10.1	16.6	39.5	19.5	8.4	12.4	28.8	22.5
	η[%]	13.2%	21.8%	51.9%	25.6%	11.0%	16.2%	37.9%	29.5%

		TEOS 200 nm							
		Si$_3$N$_4$ (w218)				**Al$_2$O$_3$** (w221)			
1 MHz	**Charging Efield** [MV/cm]	−7.5	−8	−8.5	−9	−7.5	−8	−8.5	
	Power [mW]	18.2	19.2		9.8	29.3	6.9	7.2	
	η[%]	16.7%	17.9%		9.1%	27.3%	6.4%	6.7%	
2.5 MHz	**Power** [mW]	8.7	13.2	28.6	16	18.4	34.2	41.5	
	η[%]	11.4%	17.3%	37.5%	21.0%	24.1%	44.9%	54.5%	

Table 6.4.: Summary of results obtained from the ultrasonic power transfer experiments with a resistive load.

at which $X_{s_{eq}}$ is the smallest. By connecting a resistive load, the reactive part of the equivalent impedance is not compensated. Therefore, the lower this is, the smaller the power losses, therefore the higher the efficiency. In addition, by connecting a resistor as load, the parasitic series resistance R_s is of lower influence compared to the optimal matched load, as R_{load} is in series with it and between 10 to 20 times bigger than R_s. Nevertheless, peak efficiencies of 54.5 % were achieved, which are in line with the highest achieved efficiencies using PZT crystals (Table 6.1). Considering the challenges introduced by using an inductor in an IMD or the integration into an ASIC, these results can be considered noteworthy.

6.5.3. COMPARISON WITH EXTERNALLY BIASED CMUTS

To assess the performance of the pre-charged CMUTs, their efficiency was compared to the efficiency of standard CMUT devices externally biased and without the charge trapping layer. The dielectric material of the standard CMUT devices is SiO$_2$ only, with an Equivalent Oxide Thickness of 400 nm, therefore comparable with the one of the pre-charged devices. An external DC bias was applied between the top and the bottom electrode of the CMUT by using a bias-tee circuit. Four different bias voltages were tested, namely 70 V, 80 V, 90 V and 100 V. They were chosen because, at these values, the impedance of externally biased pre-chargeable CMUTs is similar to the impedance when they are pre-charged with electric fields between
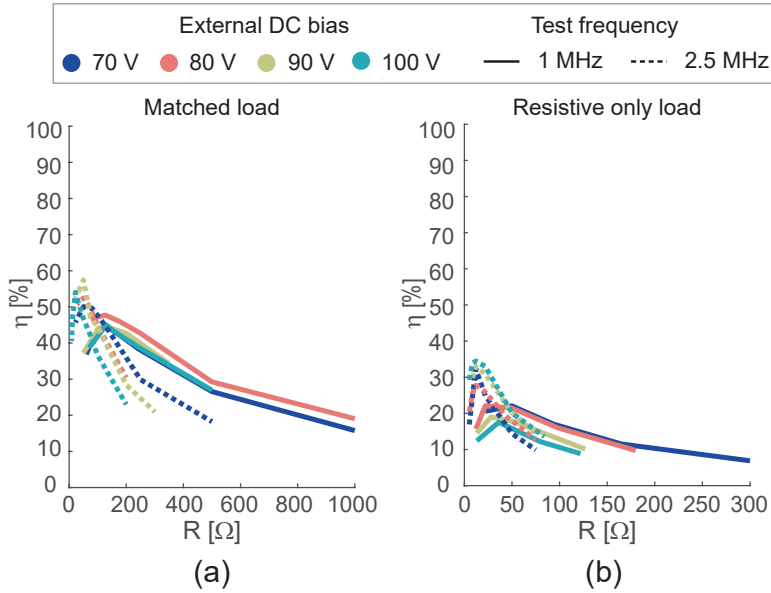
Figure 6.9.: Power transfer efficiency for standard CMUTs when externally biased with voltages ranging from 70 V to 100 V, at 1 MHz and 2.5 MHz. (a) With an optimal load. (b) With a resistive load.

−7.5 MV/cm and −9 MV/cm.

The power transfer experiment was repeated by connecting both an optimally matched load and resistive load, for the two test frequencies of 1 MHz and 2.5 MHz. The results of the experiments are presented in Fig. 6.9. The impedance of the standard CMUTs could not be measured for each of the tested voltages, therefore no comparison between equivalent impedance values can be done. However, at 1 MHz, the best performance is achieved by biasing the CMUTs at 80 V, while at 2.5 MHz by applying 90 V or 100 V. Additionally, it can be seen that the difference in performance at the tested DC bias voltages is minimal compared to the results in Fig. 6.7 and 6.8. Applying an external DC bias voltage ensures that all the CMUT cells are uniformly biased, while by pre-charging the CMUTs, it is possible that the not all the cells are uniformly charged giving rise to larger differences in performance. Nevertheless, the efficiencies achieved with the standard CMUTs are comparable to the ones achieved with the pre-charged ones.

6.6. ULTRASONIC POWER TRANSFER WITH PARTITIONED RECEIVER

A final power transfer experiment was performed to test the RX partitioning concept presented in Chapter 5. Specifically, the objective of this experiment was to demonstrate that the power received by each partition of the RX individually contributes to the total received power, meaning that the sum of the power from each partition individually measured equals the total power when all the partitions are connected together.

This concept was demonstrated for a $20 \times 20\,\text{mm}^2$ pre-charged CMUT RX subdivided into 16 partitions. A PCB that connects a full-bridge rectifier (750-CDBHD240-G, Compchip Technology) to each of the partitions was designed and fabricated for this experiment (Fig. 6.10). The simplified schematic of the PCB is shown in Fig. 6.10(b). A capacitor was added at the output of each rectifier to reduce the ripple, and a pin header to connect each partition, or the desired partitions, separately to the load.

For this experiment, a resistor was used as load, as this simplified the experiment since the goal was to demonstrate the partitioning concept, and not the maximum achievable efficiency. The experiment was performed with a $1\,\text{k}\Omega$ resistor. The CMUT was placed at the test distance and centre aligned following the procedure earlier described in this chapter. Each partition was then individually enabled, by using a jumper connector on the pin header, and the output power calculated by measuring the voltage across the $1\,\text{k}\Omega$ load. The output power for each partition is shown in Fig. 6.11(a), which schematically represents the CMUT partitions with respect to their position in

(a)   (b)
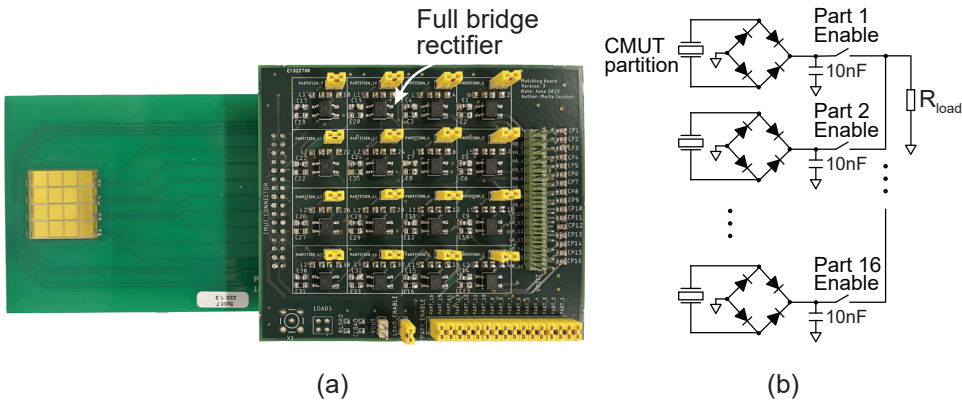
Figure 6.10.: PCB used for the partitioning experiments. (a) Picture of the $20 \times 20\,\text{mm}^2$ CMUT RX connected to the PCB with a rectifier for each partition. (b) Simplified schematic of the PCB in (a).

Experimental data:
power for each partition [mW]

4.37	5.06	4.58	3.96
4.62	6.71	6.86	5.02
4.33	6.61	7.13	4.84
4.28	5.43	5.15	4.24

(a)

Simulation results:
power for each partition [a.u.]

36.99	40.31	40.31	36.99
40.31	86.26	86.26	40.31
40.31	86.26	86.26	40.31
36.99	40.31	40.31	36.99

(b)
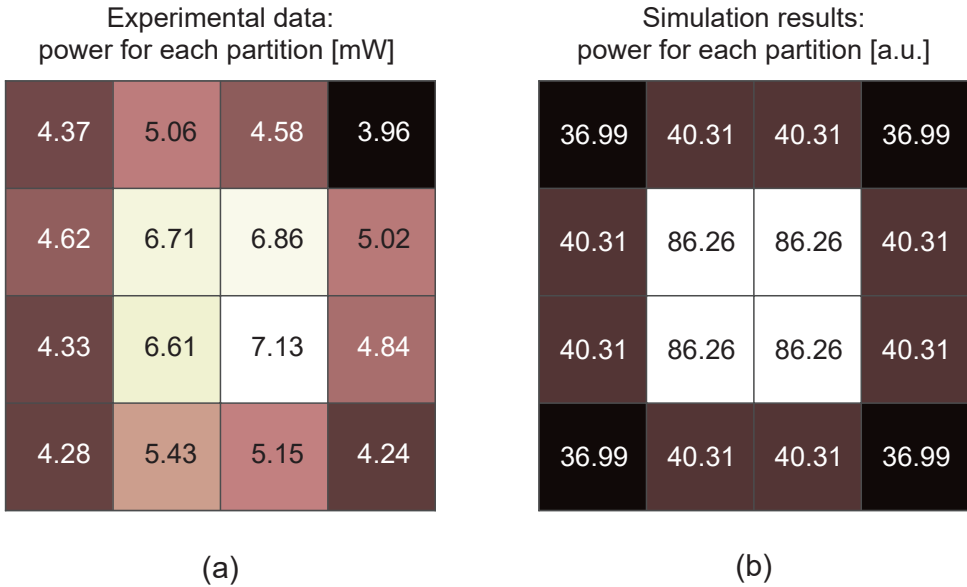
Figure 6.11.: Power received from each of the 16 CMUTs partition. (a) Experimental results. (b) Simulation results. The colour of each square encodes the amount of power from darker (lowest) to lighter (highest).

the array. Figure 6.11(b) shows the theoretical results of the same experiment obtained from a simulation using FOCUS [21], which computed the (acoustic) power in each of the partitions (note that the units are different). Comparing the distribution of the colours across the 16 partitions in Fig 6.11(a) and (b), it can be seen that the experimental results are in agreement with the simulations. Specifically, the four central partitions receive the highest and nearly the same amount of power, while the outer partitions proportionally receive a lower amount of power, with the four corner partitions receiving the least amount. The less pronounced difference in received power between partitions in the experimental results compared to the simulation results can be explained by measurement inaccuracies, and potential differences in CMUT partitions and rectifier performances.

A second experiment was performed to verify that by enabling all the partitions, the power received at the load equals the sum of the power from each partition measured in the previous experiment. This is because the output of each rectifier is connected together at the load, therefore the current at the load is the sum of the currents from each partition. The load resistor was substituted with another resistor 16 times smaller, namely 62.5 Ω, as 16 partitions are now in parallel. The power at the load in this condition was

81.3 W. Summing the power received by each partition (the values reported in Fig. 6.11(a)), the total power is 83.2 W. The difference in these two power values is rather small and mostly due to measurement inaccuracies. Hence, these results, together with the ones presented in Chapter 5 show that the power loss due to angular misalignment can be efficiently mitigated depending on the number of partitions (Fig. 5.6, Chapter 5), demonstrating the potential of this solution.

6.7. CONCLUSION

In this chapter, the power conversion efficiency of the pre-charged collapse-mode CMUTs was evaluated by means of power transfer experiments. When connected to an optimally matched load, efficiencies up to 80 % were achieved, which are significantly higher than what was achieved by other groups. In addition, when connected to a resistive load, the efficiency reached values around 50 %, due to power losses caused by the uncompensated reactive element. These results are in line with the highest performances achieved by other groups using PZT crystals, and they show the great potential of these devices, especially considering that this performance was achieved without the need for an inductor and with CMUT transducers.

The best performance was achieved at 2.5 MHz, as this is close to the centre frequency of the CMUTs by design. The device centre frequency is the most important parameter as, at that frequency, the best performance is achieved. Varying the built-in bias voltage by charging the devices at different electric fields, allows to shift that frequency to slightly higher or lower values. In addition, the four tested devices types did not show significant difference in performance. From the results we can evince that, by carefully tuning the charging parameters, performance can be enhanced at the desired operation point, if this is close to the device centre frequency.

Yet, considering in-body applications, the power loss in the medium at 2.5 MHz at 5 and 10 cm is respectively 0.45 dB and 0.9 dB higher compared to 1 MHz. Therefore, the higher efficiency at 2.5 MHz is over-passed by the larger attenuation. The drawback of operating the CMUTs at a lower frequency is that the matching inductor becomes larger, with higher losses due to increased internal series resistance. This can be mitigated by designing CMUTs with a centre frequency close to the frequency of operation. On the other hand, for applications in lower-attenuating mediums and depending on the maximum usable intensity, operating the devices at 2.5 MHz could be a better choice.

All in all, considering that about half of the maximum allowed intensity was

used in these experiments, the power at the load is in the range of values required by IMDs. Despite the fact that in these experiments a simplified scenario, in which the load is a resistor, was tested, by choosing a different type of matching, that satisfies the current and voltage requirements of a real application load, the performance is not expected to significantly change.

Ultimately, the partitioning concept was successfully demonstrated by verifying that the total power at the load is the result of the sum of the power from each partition. In addition, the results are in agreement with the simulations and, together with the results presented in Chapter 5, demonstrate the potential of this solution to mitigate the power loss due to angular misalignment.

REFERENCES

[1]   M. Saccher, R. Van Schaijk, S. Kawasaki, J. H. Klootwijk, A. Rashidi, V. Giagka, A. S. Savoia, and R. Dekker. "A Comparative Study of Si_3N_4 and Al_2O_3 as Dielectric Materials for Pre-Charged Collapse-Mode CMUTs". In: *2023 IEEE International Ultrasonics Symposium (IUS)*. 2023, pp. 1–4.

[2]   A. Amar, A. Kouki, and H. Cao. "Power Approaches for Implantable Medical Devices". In: *Sensors* 15.11 (2015), pp. 28889–28914.

[3]   R. V. Taalla, M. S. Arefin, A. Kaynak, and A. Z. Kouzani. "A Review on Miniaturized Ultrasonic Wireless Power Transfer to Implantable Medical Devices". In: *IEEE Access* 7 (2019), pp. 2092–2106.

[4]   S. Arra, J. Leskinen, J. Heikkila, and J. Vanhala. "Ultrasonic Power and Data Link for Wireless Implantable Applications". In: *2007 2nd International Symposium on Wireless Pervasive Computing*. 2007, p. 1.

[5]   S.-N. Suzuki, S. Kimura, T. Katane, H. Saotome, O. Saito, and K. Kobayashi. "Power and Interactive Information Transmission to Implanted Medical Device Using Ultrasonic". In: *Japanese Journal of Applied Physics* 41.Part 1, No. 5B (2002), pp. 3600–3603.

[6]   S. H. Song, A. Kim, and B. Ziaie. "Omnidirectional Ultrasonic Powering for Millimeter-Scale Implantable Devices". In: *IEEE Transactions on Biomedical Engineering* 62.11 (2015), pp. 2717–2723.

[7]   H. S. Gougheri, A. Dangi, S.-R. Kothapalli, and M. Kiani. "A Comprehensive Study of Ultrasound Transducer Characteristics in Microscopic Ultrasound Neuromodulation". In: *IEEE Transactions on Biomedical Circuits and Systems* 13.5 (2019), pp. 835–847.

[8]   S. Ozeri, D. Shmilovitz, S. Singer, and C. C. Wang. "Ultrasonic transcutaneous energy transfer using a continuous wave 650 kHz Gaussian shaded transmitter". In: *Ultrasonics* 50.7 (2010), pp. 666–74.

[9]   Y. Shigeta, Y. Hori, K. Fujimori, K. Tsuruta, and S. Nogi. "Development of highly efficient transducer for wireless power transmission system by ultrasonic". In: *2011 IEEE MTT-S International Microwave Workshop Series on Innovative Wireless Power Transmission: Technologies, Systems, and Applications*. 2011, pp. 171–174.

[10]   D. K. Piech *et al.* "A wireless millimetre-scale implantable neural stimulator with ultrasonically powered bidirectional communication". In: *Nature Biomedical Engineering* 4.2 (2020), pp. 207–222.

[11]   J. Charthad, M. J. Weber, T. C. Chang, and A. Arbabian. "A mm-Sized Implantable Medical Device (IMD) With Ultrasonic Power Transfer and a Hybrid Bi-Directional Data Link". In: *IEEE Journal of Solid-State Circuits* 50.8 (2015), pp. 1741–1753.

[12]   B. Herrera, F. Pop, C. Cassella, and M. Rinaldi. "AlN PMUT-based Ultrasonic Power Transfer Links for Implantable Electronics". In: *2019 20th International Conference on Solid-State Sensors, Actuators and Microsystems & Eurosensors XXXIII (TRANSDUCERS & EUROSENSORS XXXIII)*. IEEE, June 2019.

[13]   E. Mehdizadeh and G. Piazza. "AlN on SOI pMUTs for ultrasonic power transfer". In: *2017 IEEE International Ultrasonics Symposium (IUS)*. 2017, pp. 1–4.

[14]   Z. Rong, M. Zhang, Y. Ning, and W. Pang. "An ultrasound-induced wireless power supply based on AlN piezoelectric micromachined ultrasonic transducers". In: *Scientific Reports* 12.1 (Sept. 2022).

[15]   Q. Shi, T. Wang, and C. Lee. "MEMS Based Broadband Piezoelectric Ultrasonic Energy Harvester (PUEH) for Enabling Self-Powered Implantable Biomedical Devices". In: *Scientific Reports* 6.1 (2016), p. 24946.

[16]   H. Basaeri, Y. Yu, D. Young, and S. Roundy. "A MEMS-Scale Ultrasonic Power Receiver for Biomedical Implants". In: *IEEE Sensors Letters* 3.4 (2019), pp. 1–4.

[17]   B. Herrera, P. Simeoni, G. Giribaldi, L. Colombo, and M. Rinaldi. "Scandium-Doped Aluminum Nitride PMUT Arrays for Wireless Ultrasonic Powering of Implantables". In: *IEEE Open Journal of Ultrasonics, Ferroelectrics, and Frequency Control* 2 (2022), pp. 250–260.

[18]   H. Jaffe. "Piezoelectric Ceramics". In: *Journal of the American Ceramic Society* 41.11 (Nov. 1958), pp. 494–498.

[19]   Y. Birjis, S. Swaminathan, H. Nazemi, G. C. A. Raj, P. Munirathinam, A. Abu-Libdeh, and A. Emadi. "Piezoelectric Micromachined Ultrasonic Transducers (PMUTs): Performance Metrics, Advancements, and Applications". In: *Sensors* 22.23 (2022), p. 9151.

[20]   S. Kawasaki, Y. Westhoek, I. Subramaniam, M. Saccher, and R. Dekker. "Pre-charged collapse-mode capacitive micromachined ultrasonic transducer (CMUT) for broadband ultrasound power transfer". In: *2021 IEEE Wireless Power Transfer Conference (WPTC)*. IEEE.

[21]   *FOCUS*. Web Page. URL: https://www.egr.msu.edu/~fultras-web/.

6

7

ULTRASONICALLY POWERED FRACTURE MONITOR

The content of this chapter is the result of the collaboration between different partners in the context of the Moore4Medical project [1]. The author contribution includes the ultrasonic transmitter and the pre-charged CMUTs characterisation, along with the preparation of the experimental setup and testing of the system. The other components of the system have been designed, fabricated and characterised by other partners in the project. While a brief description of these components is provided in this chapter for a comprehensive understanding of the system, the author does not claim credit for their development.

7.1. INTRODUCTION

In this chapter, the pre-charged CMUTs characterised in the previous chapters are used as ultrasonic receiver and integrated into an existing battery powered implantable device. The objective is to demonstrate battery charging by means of ultrasound using the pre-charged CMUTs as receiving transducers. As introduced in Chapter 6, currently there are no ultrasonically powered implantable devices utilising CMUTs as ultrasound receivers. The major obstacle has been the requirement for a high DC bias voltage, which is not feasible for use within the body. However, using pre-charged CMUTs eliminates this obstacle, enabling the development of the first implantable device demonstrator utilising pre-charged CMUTs.
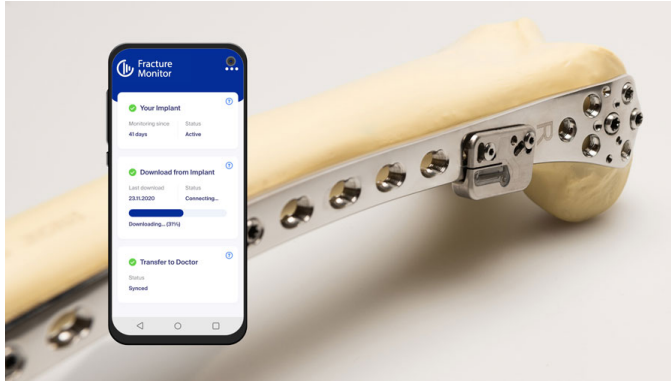
Figure 7.1.: AO fracture monitor system. Image adopted from [2].

The implant used as demonstrator in this chapter is a bone fracture monitoring implant, produced by *AO Foundation* [2]. The system is designed to be attached to a bone plate, as shown in Fig. 7.1. A bone plate is used in case of a displaced fracture, when it is necessary to fix the two disjointed parts together. Conventionally, the bone healing process is assessed using X-ray. However, as with the progressing of the healing process the bone will be able to withstand increasing loads, the share of load that the plate sustains will decrease. By using a strain gauge, the bone fracture monitoring implant measures the load fraction exerted on the plate over the course of the healing process [3]. The collected data is then transmitted via Bluetooth to a smartphone, where healthcare professionals can analyse and interpret the information.

7.2. System overview

A demonstrator device was built to demonstrate the ultrasonic charging. It should be pointed out that the device was not optimised in its form factor, as the primary objective was to demonstrate the functionality. The assembled device and its components are shown in Fig. 7.2.

The system comprises the following elements:

- Encapsulation of the CMUTs, and of the other electronics;

- Pre-charged CMUTs receiver;

- PCB boards: one for power management, and one for data collection from the strain gauge and Bluetooth data communication (BLE);

- Energy storage element.
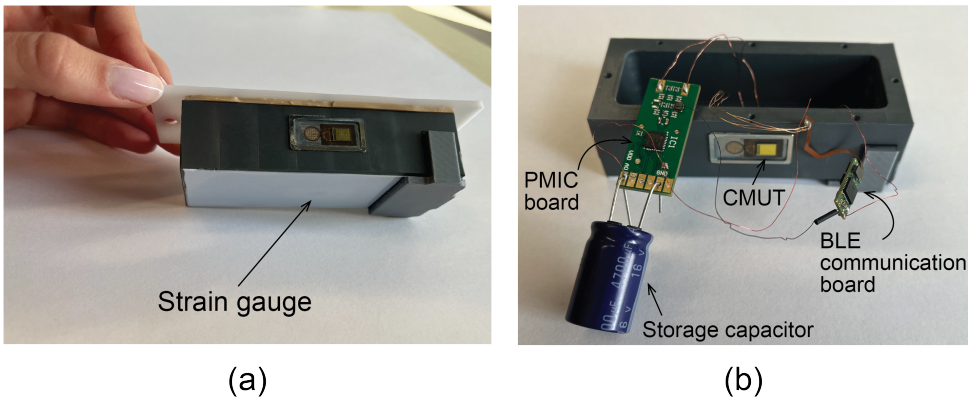
Figure 7.2.: Ultrasonically powered fracture monitor demonstrator. (a) Assembled device. (b) Components constituting the device.

The system consumes $24\,\mu W$ during data collection, and $60\,mW$ during BLE communication. These values are similar to the power values reported in Chapter 6. However, the intensity used in Chapter 6 was almost half of the FDA limit of $720\,mW/cm^2$. Therefore, even considering the power losses in the medium, due to the CMUT encapsulation and in the power management board, the harvestable power will be sufficient to power the fracture monitor demonstrator within the FDA safety limits. In addition, given these power requirements, a small rechargeable battery or a (super)capacitor are sufficient to power the system for several hours or days, requiring less frequent recharging. The operation time depends on the size of the storage element, as well as the frequency of data collection and communication.

The typical implantation depth of this device ranges between 5 and 70 mm. Therefore, considering the average energy losses in the body of $0.6\,dB/(cm\,MHz)$, a frequency of $1\,MHz$ was chosen for the ultrasonic power transfer. By using a low frequency, the power losses due to angular misalignment are also less detrimental, as explained in Chapter 5.

In the upcoming sections, a brief overview of the components comprising the ultrasonically powered fracture monitor will be provided.

7.2.1. CMUTS ENCAPSULATION

The main requirement for the system encapsulation is to prevent the leakage of toxic materials from the implant into the body, while protecting the implant from potentially damaging body fluids. Additionally, it should allow the transmission of acoustic waves to the receiver (CMUTs) with minimal efficiency degradation. Soft encapsulation is commonly used in many of the

(a)   (b)   (c)
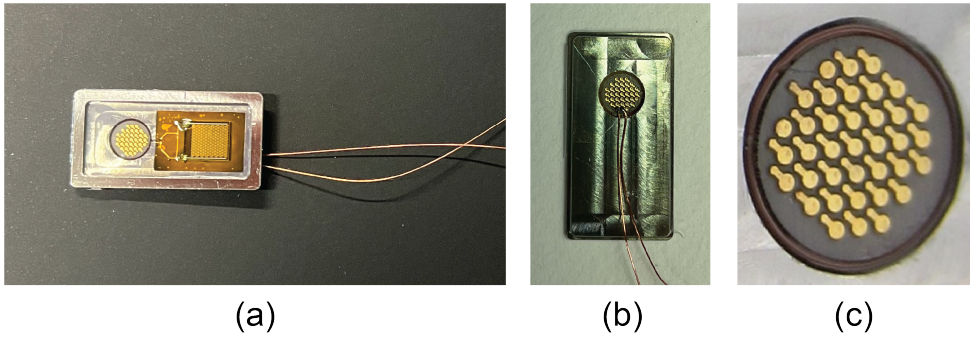
Figure 7.3.: Fabricated lid with encapsulated CMUTs. (a) Front view, (b) back view, and (c) detailed view of the feedthrough.

reported ultrasonically powered implants [4–6]. Nevertheless, this type of encapsulation, being non-hermetic, limits the device's lifespan.

For the fracture monitor demonstrator presented in this chapter, the chosen encapsulation consists of a hermetic box, housing the PCB boards and the storage element, sealed with a lid that incorporates the CMUT die. The CMUTs die is mounted on a PCB and coated with a multilayer encapsulation composed of an ALD layer followed by a layer of medical-grade silicone MED2-4213, and connected via a feedthrough to the electronics contained in the box (Fig. 7.3(b-c)). The materials selected for encapsulation were determined based on the outcomes of previous investigations [7]. For the ALD layer, a HfO_2 based material with a thickness of 50 nm was deposited at $100\,°C$ under a pressure of 3 mbar. The medical-grade silicone was spin-coated at 1000 rpm, and cured at elevated temperatures $(70-100\,°C)$, resulting in a thickness in the range of 65 to 95 µm on top of the CMUT transducer [7].

Figure 7.3 shows the fabricated lid with details of the back side and the feedthrough. In addition, it should be pointed out that, in this prototype, the housing box is not hermetic as this choice was made for ease of fabrication. However, no specific challenges are anticipated for its potential future realisation in an hermetic titanium box. Regarding the CMUT encapsulation in soft material, as the CMUT can be made biocompatible in future generations, any failure in the encapsulation does not pose safety hazards.

7.2.2. PRE-CHARGED CMUTS

The CMUTs characterised in Chapters 4 and 6 were used as ultrasonic receivers. The size of the array is $5 \times 5\,mm^2$, consisting of 173 cells in parallel. The variant with 120 nm TEOS SiO_2 was utilised, and the charge storage layer
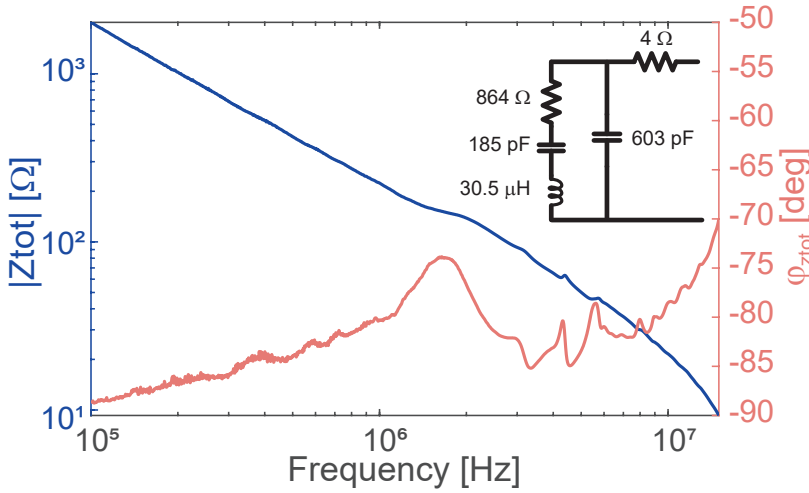
Figure 7.4.: Impedance of the encapsulated pre-charged CMUT measured in water and corresponding BVD model values.

material was Si_3N_4. After fabrication, the CMUT die was mounted on a PCB and encapsulated as described in the previous section. After assembly, the CMUTs were charged with an electric field of $-8\,MV/cm$ for 300 seconds, as in Chapters 4 and 6. Their impedance was then measured in water, and the values of the components of the equivalent BVD model were extracted. The results are shown in Fig. 7.4.

By comparing Fig. 7.4 to Fig. 6.6 in Chapter 6, it can be observed that the encapsulation does not significantly degrade the phase of the pre-charged CMUTs, with only a few degrees difference. The frequency at which the phase is minimum also remains unchanged. Therefore, it can be concluded that overall, the encapsulation did not significantly alter the properties of the CMUTs, and as a result it is not expected to significantly degrade their power conversion efficiency.

7.2.3. PCB BOARDS

The fracture monitor includes two PCB boards: one for power management, and the other one for Bluetooth communication.

The power management PCB includes an application specific Power Management Integrated Circuit (PMIC) that was specifically designed and fabricated to interface with the pre-charged CMUTs [7]. The PMIC has four main functions: a) AC-DC conversion, b) controlled battery charging, c) regulated DC supply rails generation, d) envelope and clock extraction

Figure 7.5.: Power management IC. (a) Simplified block diagram. (b) Micrograph of the fabricated PMIC.

for downlink communication. Figure 7.5(a) illustrates the simplified block diagram of the PMIC.

The AC-DC conversion is implemented using a semi-active rectifier, followed by a matching network to improve the power transfer efficiency, as seen in Chapter 6. A L-type matching network was used in this case, with a series inductor and a parallel capacitor. The values of the matching network components were calculated based on the BVD model values, and the load impedance determined by the PMIC and the storage element, and for a operating frequency of 1 MHz. A 47 µH series inductor, and 820 pF parallel capacitor were used.

The battery charger circuit enables the charging of a battery or a (super)capacitor with a programmable current in the range between 1 and 10 mA, and a programmable voltage up to 4.1 V. The regulated DC supply rails generate two stable output voltages of 3 V and 1.8 V, capable of delivering current to a load. Additionally, the envelope and clock extraction components generate data for communication between the implant and the external world, utilising protocols such as Frequency Shift Keying (FSK).

Figure 7.5(b) shows the fabricated ASIC, which occupies a total silicon area of 2.36 mm^2. The measured power conversion efficiency of the ASIC was 66 %, given by the the rectifier efficiency (72 %), and the remainder of the IC (91 %), which depends on the application requirements.

The Bluetooth communication PCB incorporates a datalogger that samples the data from the strain gauges. The data is then processed with a low-power microprocessor and the derived are values written in a non-volatile memory.

The PCB also includes a Bluetooth module for data transmission to a smartphone app [3]. This PCB is part of the already existing battery powered fracture monitor, and it was provided by AO Foundation.

7.3. ULTRASONIC POWERING AND DATA TRANSMISSION

Figure 7.6 shows the experimental setup used to test the ultrasonically powered fracture monitor. The ultrasound transmitter used for this experiment is a single element circular PZT piston transducer with 1 MHz centre frequency and 25 mm diameter. TX and RX were immersed in a tank filled with de-ionised water and centre aligned. A function generator connected to a 50 dB RF amplifier was used to generate the driving signal for the TX. The distance between the TX and RX was 110 mm, as this was the distance at which maximum power can be received, previously determined by ultrasonic field simulations. The pressure profile at this distance was characterised with an hydrophone (Chapter 6). The CMUT and PMIC output signals were measured with an oscilloscope to determine the power transfer efficiency.

For this experiment, a 4.7 mF capacitor was used as energy storage element, and connected to the PMIC board. The charging current delivered by the PMIC to the storage capacitor was set to 5 mA. The TX driving signal was a burst sine wave at 1 MHz with 12.5 % duty cycle and 0.5 Hz pulse repetition frequency. In these conditions, the peak intensity at the CMUT surface was 420 mW/cm^2, resulting in a time-averaged intensity of 52.5 mW/cm^2, which is
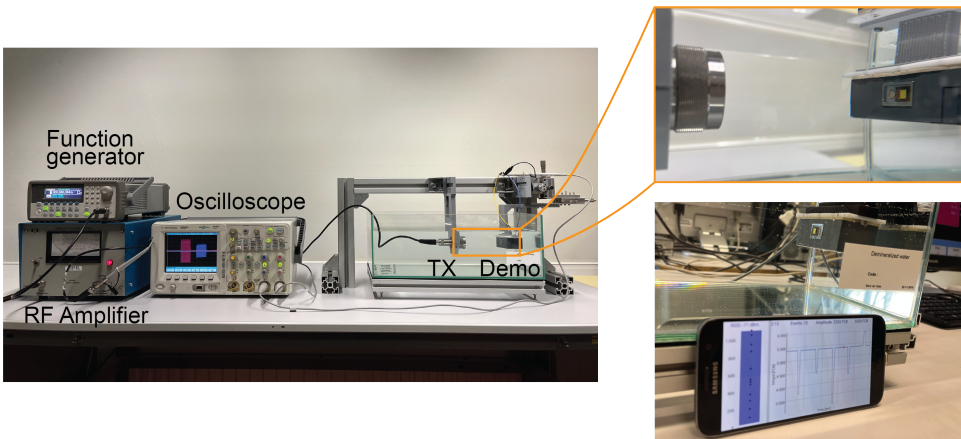

Figure 7.6.: Experimental setup used for testing the ultrasonic powering of the fracture monitor demonstrator. The bottom right picture shows the smartphone app illustrating the real time data measured by the strain gauge.

approximately 7 % of the FDA safety limit. The strain gauge is placed on the bottom side of the demonstrator, as shown in Fig. 7.2. The 4.7 mF capacitor could be charged to the desired value of 4.1 V in less than a minute, and Bluetooth communication could be established with the smartphone app. A video of the experiment showing the ultrasonic charging and Bluetooth data communication is available at [8].

By measuring the voltage at the rectifier with an oscilloscope, the system efficiency, given by the efficiency of the CMUTs, the matching network, and the PMIC, was calculated to be around 21 %. This relatively low value is attributed to imperfect matching due to inaccuracies in the equivalent source (CMUTs) and load impedance (PMIC board and storage element) values used to calculate the values of the matching components. In addition, this matching network configuration requires a significantly higher number of iterations to determine the correct components values, even when starting from the calculated ones.

Nevertheless, comparing these results with those obtained by other groups, as presented in Table 6.1 in Chapter 6, the efficiency achieved here is significantly higher. It is important to note that Table 6.1 reports the efficiency of the receiving transducer element only, while here we are considering the efficiency of the entire receiving system. This further highlights the relevance of these results. Furthermore, this efficiency aligns with that of PZT transducers as reported in the same table. However, while achieving similar efficiency, they are not biocompatible.

7.4. Conclusion

In this chapter, ultrasonic powering of a commercially available implantable fracture monitoring device was demonstrated. This represents the first ultrasonically powered system using pre-charged CMUTs as receiver. Ultrasonic powering was achieved with a system efficiency of 21 %. This efficiency can be further improved by tuning the values of the matching components. Nevertheless, the performance was significantly higher than other devices that employ PMUT or PZT transducers as receivers.

In addition, the objective of this work was primarily to demonstrate the functionality of the system. The components and their assembly were not optimised. Future device improvements include the implementation of a custom-designed small battery, reducing the device housing size, and extending operation time. In addition, the two PCB boards can be incorporated into one, optimising the shape and component distribution aiming at minimising the housing dimensions. The most significant

advancement, however, can be achieved by monolithically integrating the CMUTs directly on top of the PMIC ASIC, making use of the seamless integration advantages of CMUTs compared to PZT devices. This will drastically reduce the device size. Additionally, an hermetic case must be designed and fabricated, similar to the one in Fig. 7.1. Potential future developments also include exploring the replacement of Bluetooth communication with ultrasound, leading to lower power consumption.

REFERENCES

[1] *Moore4Medical*. Web Page. URL: https://moore4medical.eu/.

[2] *AO Fracture Monitor*. Web Page. 2023. URL: https://www.aofoundation.org/what-we-do/innovation-translation/innovation-funding/portfolio/fracture-monitor.

[3] M. Windolf *et al.* "Continuous Implant Load Monitoring to Assess Bone Healing Status—Evidence from Animal Testing". In: *Medicina* 58.7 (2022), p. 858. URL: https://dx.doi.org/10.3390/medicina58070858.

[4] B. C. Johnson *et al.* "StimDust: A 6.5 mm^3, wireless ultrasonic peripheral nerve stimulator with 82% peak chip efficiency". In: IEEE, 2018.

[5] S. Hosseini, K. Laursen, A. Rashidi, T. Mondal, B. Corbett, and F. Moradi. "S-MRUT: Sectored-Multiring Ultrasonic Transducer for Selective Powering of Brain Implants". In: *IEEE Transactions on Ultrasonics, Ferroelectrics, and Frequency Control* 68.1 (2021), pp. 191–200.

[6] M. J. Weber, Y. Yoshihara, A. Sawaby, J. Charthad, T. C. Chang, and A. Arbabian. "A Miniaturized Single-Transducer Implantable Pressure Sensor With Time-Multiplexed Ultrasonic Data and Power Links". In: *IEEE Journal of Solid-State Circuits* 53.4 (2018), pp. 1089–1101.

[7] *Moore4Medical public deliverables*. Web Page. 2024. URL: https://moore4medical.eu/public_deliverables.

[8] M. Saccher. *Video recording showing ultrasonic powering of a fracture monitor demonstrator prototype*. 2024. URL: https://data.4tu.nl/datasets/a666adb6-8351-43a4-9742-d25b33c25510/1.

7

8

CONCLUSIONS AND RECOMMENDATIONS

8.1. CONCLUSIONS

Ultrasound is becoming an important aspect of emerging medical devices such as for bioelectronic medicines, ultrasound patches, and point-of-care solutions thanks to the development of high-volume, cost-effective MEMS ultrasound transducer technologies. Among these, CMUT technology has matured to the level of traditional PZT based devices. However, one main disadvantage remains the need for an external DC bias voltage. This thesis investigated the performance of (bias-free) pre-charged collapse-mode CMUTs. The specific focus of this investigation was their use as ultrasonic power receivers in implantable devices. Furthermore, their potential as substitutes for conventional externally biased CMUTs or other ultrasonic transducers, in applications where such transducers are presently employed, was determined. The main contributions in the field are stated below.

CONTRIBUTION 1: PRE-CHARGED CMUTS CHARACTERISATION

This thesis demonstrated the feasibility of pre-charged collapse-mode CMUTs, by including a charge storage layer in their dielectric. A first generation of CMUTs devices with an ALD Al_2O_3 charge storage layer in the dielectric was pre-charged by applying a high DC bias voltage for a few minutes. The first complete characterisation was made highlighting the potential of these devices.

A second generation of CMUT devices was then designed and fabricated with the aim to compare the performance of ALD Al_2O_3 and PECVD Si_3N_4, and two different thicknesses of the bottom PECVD TEOS SiO_2 layer. Several

MIM capacitors with different dielectric stack combinations were fabricated with the objective to use the results from these experiments as a starting point for the design of the second generation pre-chargeable CMUTs dielectric. The results did not suggest an optimal layer combination indicating that different device types or methods should be used for this purpose.

Four pre-chargeable CMUTs variants were fabricated and the characterisation was repeated, showing a performance in line with the one of standard externally biased devices. In addition, for the first time, static and dynamic lifetime measurements were performed. While recognising the need for further testing with a larger population size for a complete characterisation, the results indicated the potential suitability of these devices for use in implantable applications for acute scenarios, or in disposable instruments such as catheters. In addition, no significant performance difference was found between ALD Al_2O_3 and PECVD Si_3N_4, suggesting that factors such as availability of the materials, ease of deposition, and charging should be evaluated when choosing the material for the charge storage layer. Moreover, the results showed that devices with a thicker TEOS SiO_2 trapped a larger amount of charge, and showed a longer lifetime.

CONTRIBUTION 2: ULTRASONIC POWERING FEASIBILITY AND MITIGATION STRATEGIES

In this thesis, the pre-charged CMUTs were used as ultrasonic power receivers. Depending on the power requirements of implantable devices, cm-scale receivers may be required. The impact of lateral and angular misalignment on the amount of received power was assessed as a function of the RX area by means of simulations, and verified with experimental data. It was demonstrated that angular misalignment is the most detrimental, and it worsens as the frequency increases. Three solutions were proposed:

- **Decrease the frequency**, which will also reduce the energy losses in the body. However, the extent to which the frequency can be lowered is constrained by design challenges associated with CMUT transducers.

- **Partitioning the RX transducer**. It was shown that the larger the number of partitions, the better the improvement in received power in case of angular misalignment. Although this concept is not new, in this thesis it was quantified and experimentally tested with results in line with the simulations. This solution however requires a rectifier (and a matching network) for each partition. Therefore, the number of partitions should be determined as a trade-off between the minimum

acceptable power loss due to misalignment, and the added packaging complexity.

- **Using a linear or matrix array TX transducer** in combination with a beamforming algorithm. This solution is mainly useful for compensating the lateral misalignment. The effectiveness of this method was demonstrated using the phase reversal beamforming algorithm. Using a linear array TX transducer and a simple telemetry circuit at the RX, pre-charged CMUT could be reliably tracked when moving at a speed of 1 mm/s.

In conclusion, it was shown that angular and lateral misalignment can be successfully mitigated by implementing a combination of the three proposed solutions.

CONTRIBUTION 3: EFFICIENCY ESTIMATION OF ULTRASONIC POWERING

The power conversion efficiency of the pre-charged CMUTs was evaluated through ultrasonic power transfer experiments. The impact of different charging electric fields on the pre-charged CMUTs performance as power receivers was tested at 1 MHz and 2.5 MHz.

It was shown that the highest efficiency is achieved at 2.5 MHz, close to the centre frequency for which the devices are designed, achieving peak values of 86 % with an optimally matched load. The achieved efficiencies are higher than previously obtained results. In addition, they highlighted the importance of the minimisation of the parasitic series resistance of the interconnects. The power conversion efficiency was also evaluated for a resistive load, showing promising results with peak efficiencies of around 50 %. Finally, it was shown that by adjusting the charging parameters, the resonance frequency can be shifted around the centre frequency, enhancing the performance at the desired operational frequency.

CONTRIBUTION 4: ULTRASONICALLY POWERED FRACTURE MONITOR

Battery charging by means of ultrasound was demonstrated for a commercial implantable bone fracture monitoring device. This was the first ultrasonically powered system using pre-charged collapse-mode CMUTs as receivers. This achievement was made possible through collaborative efforts within the Moore4Medical project, with partners contributing to the encapsulation of CMUTs and the design of a power management IC. The system successfully attained ultrasonic powering and Bluetooth data communication, exhibiting a system efficiency of 21 % at an average acoustic intensity of about 7 % of the

FDA safety limit. While achieving a higher efficiency is possible by fine-tuning the matching network components, the performance was significantly better than other reported devices that employ PMUT or PZT transducers as receivers.

In summary, the findings presented in this thesis demonstrate the potential of pre-charged collapse-mode CMUT devices. Their acoustic performance is comparable to that of standard externally biased devices, making them viable substitutes in applications where standard devices or PZT transducers are commonly employed, particularly in space-constrained scenarios. Moreover, the absence of a DC bias, other than simplifying and compacting the driving electronics, makes them very attractive for implantable devices and patch applications, where the necessity for an external bias renders standard devices unsuitable. While the focus here has been on utilising pre-charged CMUTs as power receivers, their transmit mode performance is in line with that of standard devices. This extends their possible use to imaging applications, such as in patches or point-of-care devices, or in IVUS or ICE catheters. Finally, in this thesis, several geometries and misalignment scenarios were analysed in the context of power transfer applications. However, to achieve high system efficiency, an overall optimisation including geometry and number of elements (partitions) of both the transmitting and receiving transducer must be performed for each application.

8.2. SUGGESTIONS FOR FUTURE WORK

Despite the promising results achieved in this thesis, further development and improvements are required before a successful commercialisation of pre-charged CMUTs can be considered.

- The results from the static and dynamic lifetime tests, despite showing promising results were performed on a limited number of samples due to time constraints. A larger number of samples should be tested to assess the lifetime and determine the range of applications in which the pre-charged CMUTs can be used. In addition, the tests should be performed at body temperature to evaluate the accelerated performance degradation due to a temperature higher than room temperature. Moreover, the lifetime should be assessed in receiving mode other than in transmitting mode, and with different types of waveform.

- For the first pre-charged CMUTs generation it was demonstrated that charging the devices at higher temperatures led to an increase in their

lifetime. This should be investigated for the devices of the second generation. Exploring this effect could potentially reduce the required charging voltage and improve charge retention.

- The second generation of pre-charged CMUTs showed excellent acoustic and electrical performance and they were successfully used as power receivers for the fracture monitor device. One of the next steps in their development is their fabrication on top of an ASIC. By doing this, assembly will be significantly simplified and size will be reduced.

- The long term effects of ultrasonic power transfer through the body must be investigated.

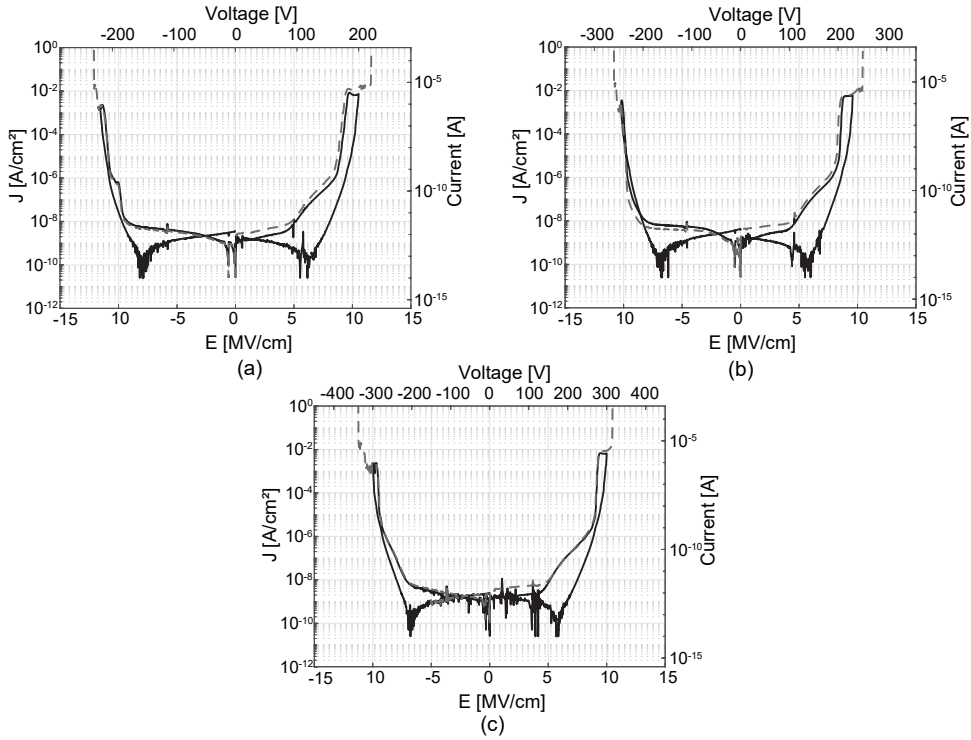**8**

A

APPENDIX: FIRST-GEN PRE-CHARGED CMUTS

Figure A.1.: I-V curves measured on the test capacitors. (a) variant B, (b) variant C, (c) variant D.

A

Symbol	Description
t_m	Thickness of the top membrane
ρ_{tp}	Mass density of the top membrane
t_g	Height of the vacuum gap
a	Membrane radius
r	Radial coordinate
$w(r)$	Displacement of the membrane along the radial direction
D	Flexual rigidity of the top membrane
$V(t)$	External voltage applied to the top membrane
σ_m	Standard deviation of the combined surface roughness
H_{ab}	Indentation hardness
τ	Uniform biaxial residual stress
t_{eff}	Effective gap height
t_i	Dielectric layer thickness, where $i = 1,2,3,4$
$\varepsilon_{Al_2O_3}$	Relative permittivity of Al_2O_3
ε_{SiO_2}	Relative permittivity of SiO_2
$\rho(r)$	Volume charge along the radial direction [C/m^3]
$\sigma(r)$	Surface charge along the radial direction [C/m^2]
$x_1(r)$	Equivalent vacuum height
x_2	Equivalent dielectric thickness
$t_3{}^*$	Equivalent oxide thickness of Al_2O_3 layer
$P_e(r)$	Electrostatic pressure
$V_{eff}(r)$	Effective voltage due to the built-in charge
$s(r)$	Gap height along the radial direction
$\sigma_1(r)$	Combined contribution of surface and volume charge
P_{atmos}	Atmospheric pressure
σ_0	Surface charge density
ρ_0	Volume charge density
r_{charge}	Contact radius during charging
V_{pi}	Pull-in voltage
k	Spring constant
kt^2	Electromechanical coupling coefficient

Table A.1.: Summary of the symbols used in this work
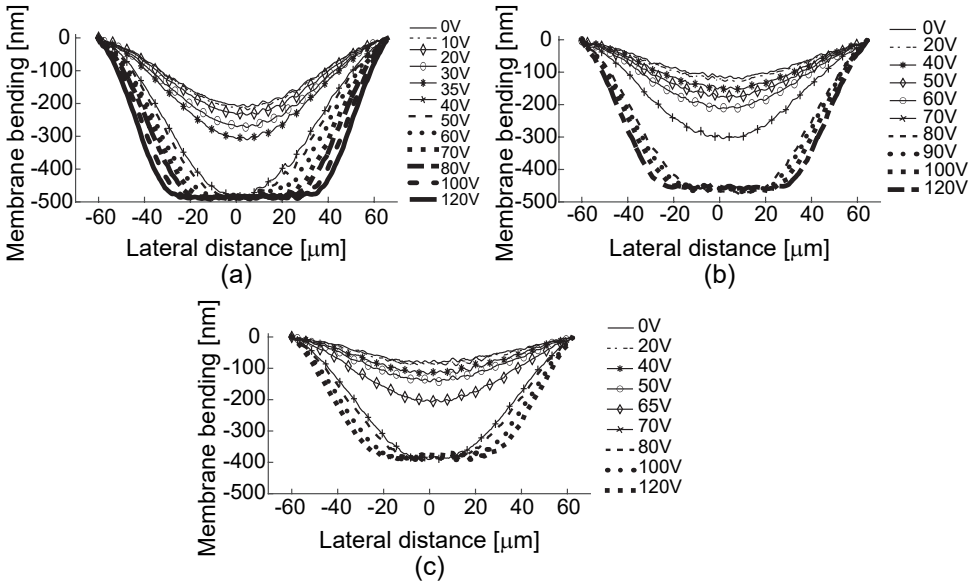
Figure A.2.: Membrane profile shape measured with the DHM for the other CMUT variants. (a) layer stack B, (b) layer stack C, (c) layer stack D.
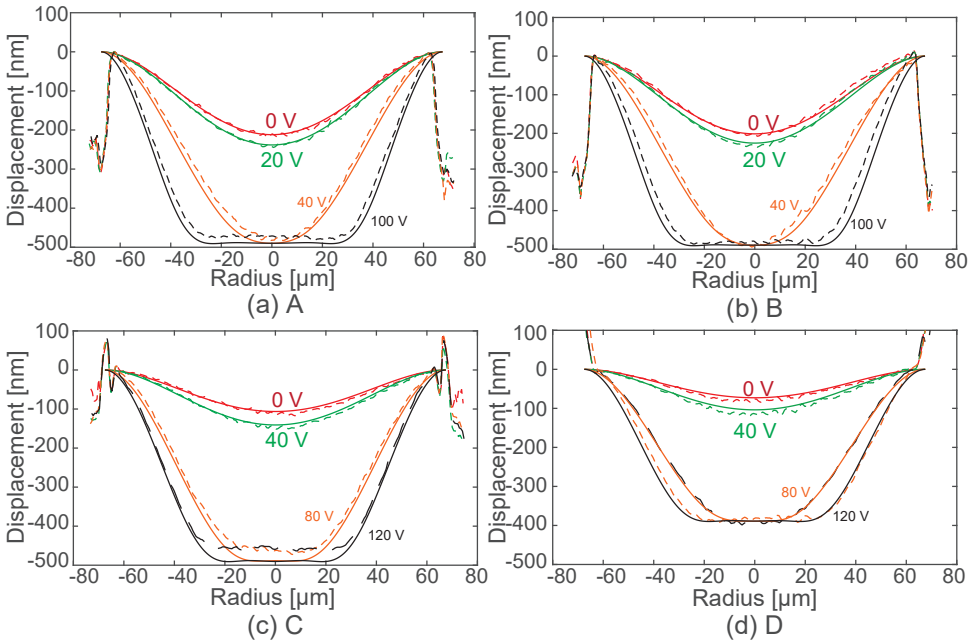
Figure A.3.: Fitted membrane profile (solid line) and the simulated membrane profile (dashed line) is compared at several DC voltages for (a) variant A (b) variant B (c) variant C and (d) variant D.

Figure A.4.: Membrane displacement at the center of the CMUT showing the pull-in behavior; comparison between the simulation and the measurements results. (a) variant B (b) variant C (c) variant D.

Figure A.5.: Transient response and bandwidth of the CMUT for different bias voltages.

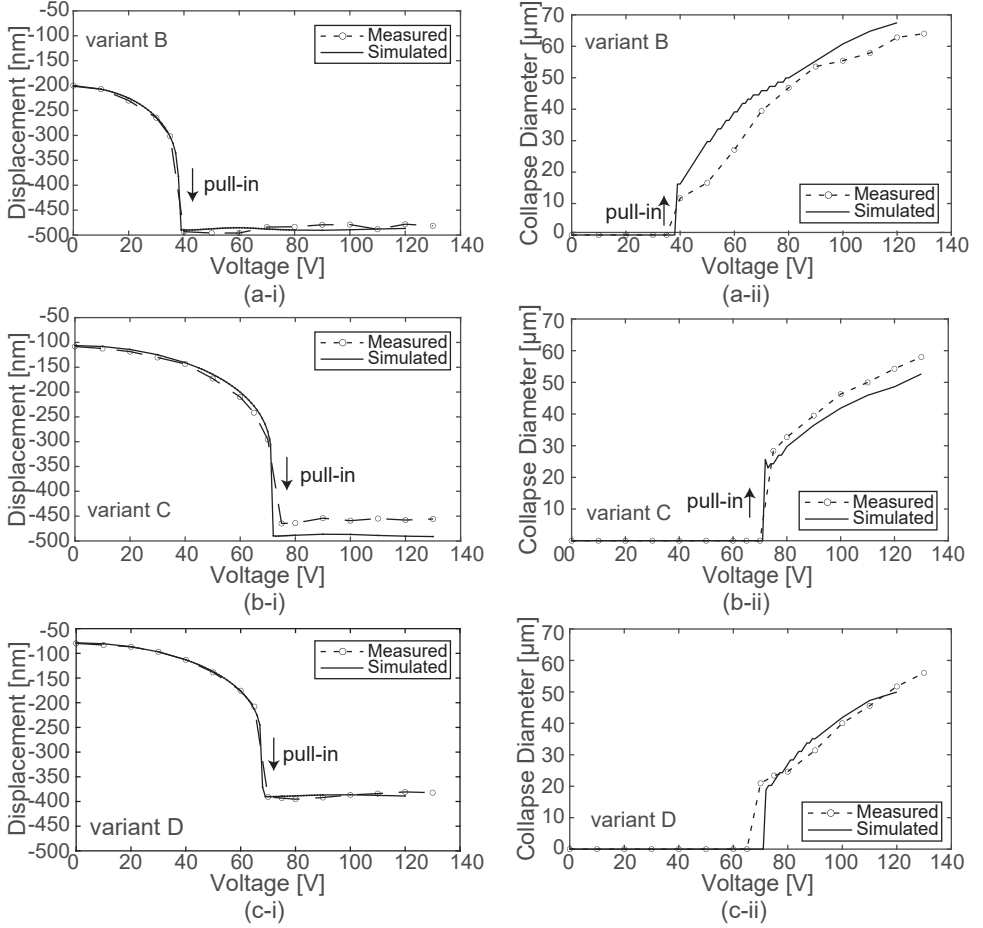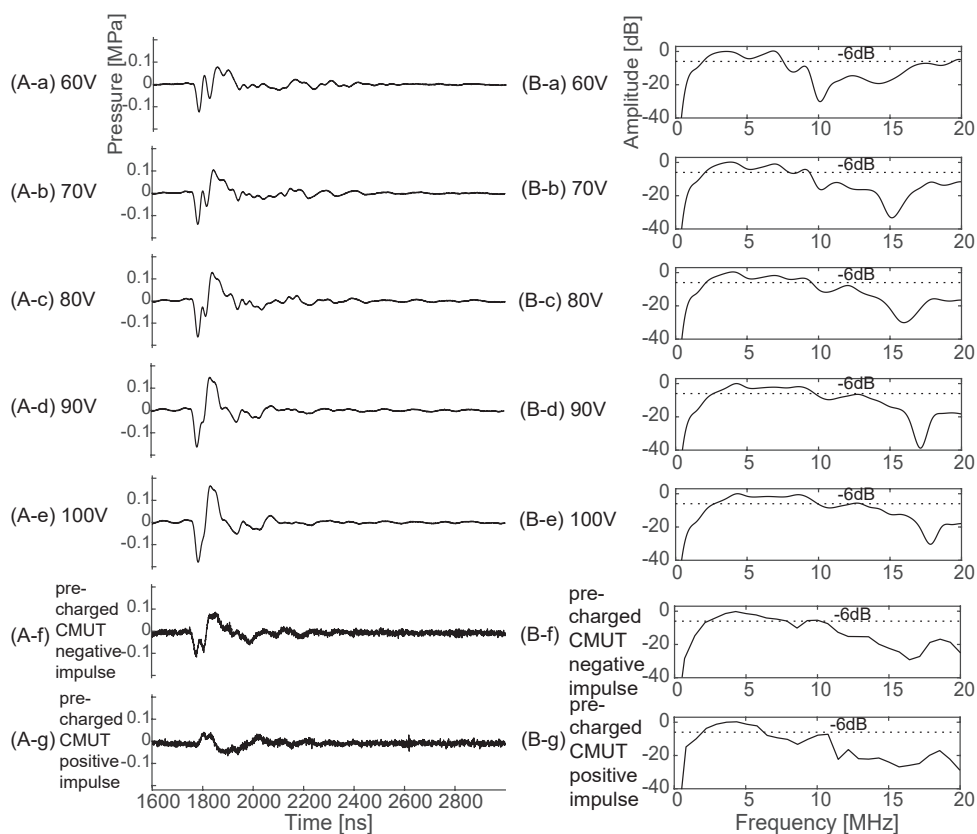|	Transducer type	lead-based?	Dimension	I_{rc} [mW/cm^2]	Freq [MHz]	Power output [mW]	Power density [mW/cm^2]	Efficiency [%]	Depth [mm]	Medium	Rectified?	Source
1	BaTiO$_3$ Plate	No	1.65 x 1.65 x 1.5	290	1.3	NR	110	37.9	105	Castor oil	Yes	[a]
2	AlN diaphragm array	No	8 x 8 x 0.3	77	2	0.001	0.007	0.009	40	Water	No	[b]
3	0-3 BaTiO$_3$ / PLGA composite	No	1 x 1 x 0.012	65	2.3	1	1	1.5	10	Water	No	[c]
4	PZT Plate	Yes	1 x 1 x 1.4	100	1	0.4	40	40	27	Ex-vivo tissue	No	[d]
5	PZT Diaphragm	Yes	4 x 4	74.8	0.088	0.7	17.5	23	20	Water	No	[e]
6	PZT Plate array	Yes	21 x 21 x 2	65	0.35	0.0176	0.004	0.006	23	Water	No	[f]
7	Pre-charged CMUT	No	0.84 x 7.56 x 0.7	15.5	2.15	0.42	6.7	43	70.4	Water	No	[g]
		No	0.84 x 7.56 x 0.7	26.2	5.85	0.78	12.4	47	176	Water	No	
8	Pre-charged CMUT	No	0.91 x 7.56 x 0.7	260	2	9	125	46	60	Water	No	**This work**
		No	0.91 x 7.56 x 0.7	1270	2	26	361	27	60	Water	No	
		No	0.91 x 7.56 x 0.7	3100	2	47	653	20	60	Water	No	

[1] Dimension : Width x Length x Thickness
[2] I_{rc} : Incident intensity on the transducer
[3] Power Output : Power dissipated at the load
[4] Power density : Power Output / receiver area
[5] Efficiency : Power density / I_{rc}

a) J. Charthad, S. Member, T. C. Chang, et al., "A mm-Sized Wireless Implantable Device for Electrical Stimulation of Peripheral Nerves," IEEE Transactions on Biomedical Circuits and Systems, vol. 12, no. 2, pp. 257–270, 2018. DOI: 10.1109/TBCAS.2018.2799623.

b) B. Herrera, F. Pop, C. Cassella, and M. Rinaldi, "AlN PMUT-based Ultrasonic Power Transfer Links for Implantable Electronics," 2019 20th International Conference on Solid-State Sensors, Actuators and Microsystems and Eurosensors XXXIII, TRANSDUCERS 2019 and EUROSENSORS XXXIII, no. June, pp. 861–864, 2019. DOI: 10.1109/TRANSDUCERS.2019.8808320.

c) S. Selvarajan, A. Kim, and S. H. Song, "Biodegradable piezoelectric transducer for powering transient implants," IEEE Access, vol. 8, pp. 68 219–68 225, 2020, ISSN: 21693536. DOI: 10.1109/ACCESS.2020.2985993

d) J. Charthad, M. J. Weber, T. C. Chang, and A. Arbabian, "A mm-Sized Implantable Medical Device (IMD) With Ultrasonic Power Transfer and a Hybrid Bi-Directional Data Link," IEEE Journal of Solid-State Circuits, vol. 50, no. 8, pp. 1741–1753, 2015, ISSN: 00189200. DOI: 10.1109/JSSC.2015.2427336.

e) H. Basaeri, D. B. Christensen, and S. Roundy, "A review of acoustic power transfer for bio-medical implants," Smart Materials and Structures, vol. 25, no. 12, 2016, ISSN: 1361665X. DOI: 10.1088/0964-1726/25/12/123001.

f) L. Jiang, Y. Yang, R. Chen, et al., "Flexible piezoelectric ultrasonic energy harvester array for bio-implantable wireless generator," Nano Energy, vol. 56, pp. 216–224, 2019. DOI: 10.1016/j.nanoen.2018.11.052.Flexible.

g) S. Kawasaki, Y. Westhoek, I. Subramaniam, M. Saccher and R. Dekker, "Pre-charged collapse-mode capacitive micromachined ultrasonic transducer (CMUT) for broadband ultrasound power transfer," 2021 IEEE Wireless Power Transfer Conference (WPTC), 2021, pp. 1-4, doi: 10.1109/WPTC51349.2021.9458104.

Table A.2.: Comparison to other ultrasound power transfer work.

B

APPENDIX: MIM CAPACITORS FLOWCHART

MARKER

- Start with <100> 200 mm wafers 25 Ω/cm p-type
- ASML marker lithography
- Etch markers 140 nm deep in Si
- Dry resistrip

FIRST METAL LAYER

- Deposit 190 nm AlNd/50 nm TiW (PVD) bottom electrode

DIELECTRIC LAYERS DEPOSITION

- Deposit PECVD TEOS at 400 °C (Novellus)
  - Thickness 50 to 400 nm
- Deposit PECVD Si_3N_4 at 400 °C (Novellus)
  - Thickness 200 or 400 nm
- Deposit ALD Al_2O_3 at 300 °C (thermal process, ASMI)
  - Thickness 200 nm
- Deposit PECVD TEOS at 400 °C (Novellus)
  - Thickness 50 to 250 nm
- Open ring electrode at the side of the wafer (approx. 10 mm)
- Ring lithography (sheet mask)
- Dry-etch dielectric layers stop on bottom electrode
- Dry resiststrip

B

SECOND METAL LAYER

- Deposit 50 nm TiW/190 nm AlNd (PVD)
- Sputter-etch deposit 1000 nm AlCu (PVD) top electrode
- Top electrode lithography (contact aligner), outer ring has still resist
- Wet-Etch top electrode AlCu in PES77 at 30 °C
- Dry resiststrip
- Wet-etch TiW in H_2O_2 at room temperature

BACKSIDE CONTACT

- Sputter-etch deposit 1000 nm AlCu (PVD) top electrode
- Top electrode lithography (contact aligner), outer ring has still resist
- Wet-Etch top electrode AlCu in PES77 at 30 °C
- Dry resiststrip
- Wet-etch TiW in H_2O_2 at room temperature

C

APPENDIX: SECOND-GEN PRE-CHARGED CMUTS

	TEOS 120 nm							
	Si$_3$N$_4$ (w223)				**Al$_2$O$_3$** (w225)			
Charging Efield [MV/cm]	7.5	8	8.5	9	7.5	8	8.5	9
Rm [Ω]	735.6	375.8	277.1	215.9	986.1	546.4	318.1	231.2
Lm [µH]	74.4	20.1	12.4	9.6	74.3	33.5	13.8	9.8
Cm [pF]	222.3	248.9	236.6	210.0	230.3	230.1	232.1	226.3
Ce [pF]	642.7	708.5	792.5	840.3	681.6	779.6	847.1	903.0
Rs [Ω]	11.2	10.1	11.5	10.6	14.7	12.4	10.9	10.3

	TEOS 200 nm						
	Si$_3$N$_4$ (w218)				**Al$_2$O$_3$** (w221)		
Charging Efield [MV/cm]	E −7.5	−8	−8.5	−9	−7.5	−8	−8.5
Rm [Ω]	1036.4	499.8	370.2	294.1	664.5	364.0	278.0
Lm [µH]	80.4	27.9	18.5	14.0	36.7	13.0	11.2
Cm [pF]	189.4	210.6	190.7	173.2	202.7	245.8	191.3
Ce [pF]	547.5	619.5	696.2	726.3	678.8	682.9	795.4
Rs [Ω]	11.8	11.5	11.9	11.3	13.1	9.9	11.2

Table C.1.: Summary of components values estimated by fitting the BVD model to the measured impedance of the pre-charged CMUTs.

ACKNOWLEDGEMENTS

This PhD has been quite a journey. I started exactly at the start of the Covid pandemic and thinking about it now it seems almost surreal. It has been a tough journey but I was lucky to be surrounded by many people who supported and encouraged me along the way.

First and foremost I would like to thank my supervisor, Ronald Dekker. Ronald, thank you for all the opportunities you gave me throughout these years. I still remember the first time I came to speak to you for a master project, and you mentioned you were working on vagus nerve stimulation with ultrasound. At that time I still knew almost nothing about ultrasound or CMUTs but I was so excited about the project. Things turned out a bit differently during these years, although the CMUTs remained, but you always encouraged me and helped finding new opportunities to try one more time. Thank you for your support and patience! It has been really nice to work with you and even if I know you are slowly retiring from your commitments, I hope we will stay in touch in the years to come and that you will enjoy your time.

During my PhD I had the great opportunity to be part of the European Project Moore4Medical. I would like to thank all the partners from all Europe that I was fortunate to meet and work with: Vasso, Alessandro, Rob, Amin, Frederic, Frederik, Cyril, Heiko, Andreas. I am very happy we managed to make the fracture monitor demo work just before the final workshop and it is now very convincing and supporting many results of this dissertation. A special thanks goes to Vasso, thank you for supporting me and for your advice throughout these years. You are always very enthusiastic about new ideas, and it has been really nice to work with you. Amin, thank you for all the times you came to Eindhoven for the demo experiments and for sharing your knowledge on the circuit design. It was nice to have discussions and work with you these years. Another big thank goes to Alessandro. We met when I was still a master student, and you were chairing our session at the ICU conference in Brugge. That was the first time we officially presented the first results on the pre-charged CMUTs and I think the best conference I have been to! It has been great to learn from you during these years, so thank you for sharing your knowledge and for your time and patience. It has been a pleasure to work with you and I hope we will keep in touch. Thank you

also to all the PhD students in the project: Mohammad, Lara, Gonzalo, Andra, Agnes, Thomas, Ryan. It was fun to spend time together in the online events and then during the workshops. Finally, a big thank you to Ronald and Sieger to make this project happen, for organising the workshops in such wonderful locations, and creating this great community.

Jian and Shin, it has been great to have you as colleagues. Jian, thank you for always being so optimistic and understanding. I had a great time with you in the office. Thank you for sharing your Chinese culture bringing and cooking special treats for me! Shin, we had so many adventures together trying to stimulate nerves with ultrasound, from Rotterdam to Amsterdam to Germany…unfortunately most of them unsuccessful. It has been great to work with you during these years, with your endless curiosity and always wanting to tinker around in the lab trying to discover new things. I hope we will keep going for beers in the years to come!

I had the great opportunity to work on this thesis at Philips. It has been a great experience; I was surrounded by so many knowledgeable people that were always happy to answer my questions and help me. Eugene and Johan, you have been of great help during these years, you always supported me and helped me finding the right solution. Eugene, thank you for all the coffees in the lab, for helping me making all kind of crazy things, from making the candle gel phantoms in the cake tray, to helping me with the microscopes, translating my requests to the workshop guys, and taking the best CMUTs pictures. You were always available to help, at any time I came to your office, and I always knew that I could find what I was looking for in your labs. Many things would not have happened if it was not for you. Johan, thank you for your insights in the CMUTs and dielectrics world. It was nice to discuss the results with you, and thank you for your advice. Rob, sorry for all the times I dropped into your office asking you if you had five minutes to discuss something, that then most of the time became twenty. I really appreciate your help with discussing the measurements results, and your interests in the performance of the pre-charged CMUTs. It was nice to work in the Moore4Medical project together and I learned a lot from you. I also need to apologise with Wouter for all the times I came into your office asking for advice on something mechanical or to 3D print something. You never sent me away and always helped me with a smile despite you are always busy. It is thanks to you and your advice if I can design better pieces now! Bas, you can assemble and handle the smallest things. Thank you for helping me with the MEA plate, when I was still believing in it. Marcel, even if you left Philips already some time ago, you helped me a lot with the PZT on the guidewire. You gave me all the material, showed me the tricks of holding them with

the spinal needles, etc... unfortunately it didn't work in the end, but I am very grateful for your help and effort. Thank you also to all the people that helped me with the measurements and fabrication of pieces for my setups: Bart and Mark for the acoustic measurements, Chris van Heesh and Micha for helping me with the DHM, Peter Blanken for teaching me the secrets of the impedance analyser when I was still at the beginning of my PhD and for the later discussions on the CMUTs model, Bert op het Veld, Jaap Haartsen, Tiny for the laser cutting of the most strange parts, and all the people from the mechanical workshops that helped me during these years.

A big thank you also to Rameswor for listening to all my complaints and encouraging me especially during the last period of my PhD. It has been really nice to have chats with you in the lab and thank you for making sure I had enough space in the lab to complete my experiments after the reorganisation. Emiel, thank you for your help, your soldering skills and your patience in teaching me how to do it properly. I would have not been able to complete the experiments without your help. Lambert and José, thank you as well for the nice discussions and good advice when I would pass by your office.

Hans Huiberts, thank you for the opportunity to work at Philips during my PhD and for welcoming me into your (former) department. Despite everything, I learned a lot from my time there and it has been great to have easy access to so many facilities and instruments whenever I needed. I think this would have been much harder if I was at the university! In a way, I have been fortunate to experience (luckily mainly indirectly) all the changes that happened at Philips in the last years. I learned a lot from them, especially that change is not always bad, and to be more open to it. So, I am very grateful.

Although I spent most of my time at Philips, I must also thank the people in Delft for their support and the enjoyable times we shared on various occasions. First of all, Prof. Sarro, thank you for your support over these years and for your confidence in me. Thank you also for agreeing to be on my promotion committee. Massimo, Niko, Marta, Marian, and Nikki, thank you for your advice and help. I would also like to thank the other members of the committee for agreeing to be part of it: Prof. French, Dr. Bosch, Dr. Pertijs, Prof. Savoia, and Dr. Vollebregt. Thank you also to the master students I supervised: Laurent and Sai Sandeep. I enjoyed guiding you and learned a lot about empathy through the experience.

Now it is time to thank all the friends behind the scenes that have nothing to do with this thesis but who have enriched my life and brought so much fun. Rishabh, we were both Philips interns when we first met. You have been my best supporter over these years, first when I moved to Denmark and then when I came back here. You are kind and fun, always encouraging me and

offering valuable advice. I hope you will stay in my life to see what the future holds. I am proud to be your friend and to have you as mine. I wish you all the best! Amal and Irene, thank you for putting up with me as your housemate. I still remember our home office on the living room table at the start of Covid, where the three of us used to work together and all the improvised "parties" during the pandemic. We all started our PhDs around the same time, and it was comforting to share our struggles. I have wonderful memories of our time together and wish you great success! Himanshu, Saharsh, Andrea V. and Andrea D. thank you for all the fun times during the past years, especially during Covid. Aya, I met you long before my PhD, and I hope we will continue our weekend brunches. It's always a pleasure to spend time with you! Claudia, I am very happy I met you through volleyball. Every time we meet, I have a great time and enjoy sharing our (mis)adventures and advice. I admire you for navigating the academic world. Adriana and Alex, it's quite amusing that we met in Delft many years ago and then, a couple of years ago, discovered by chance that we were living in the same city, just minutes away from each other. Adriana, you are so sweet, and your cooking is always wonderful. Alex, I love your passion for board games! I always enjoy spending time together and I wish you all the best for your life together! To my friends from Italy — Marti, Paolo, Andrea B., Michele, Lollo, Bosca, Flumi, and Vinish — thank you for all the adventures together and for your unwavering support!

Finally I want to thank my family. Mum and Dad, thank you for giving me the opportunity to come to the Netherlands. Thank you for your sacrifices and all the love you give me every day. I know it is hard for you that I am far away from home and I will be forever grateful for all you have done for me. You taught me a lot and always encouraged my curiosity, raising me as a strong and independent woman. Mauro, my uncle, who I always admired and has been an example for me for many years. To my second family, Frédérique, Peter, Steven, and Kathelijn, thank you for taking care of me and welcoming me into your family. You are very loving and sweet, and I am happy to have you with me.

Mitchell, my loving boyfriend, my best friend, my adventures mate, my coffee expert, and many other wonderful things. You have witnessed this PhD journey from the start and always encouraged me, listened to my frustrations and complaints and gave the perfect advice. You are the best listener and always there for me, and I am so lucky to have you in my life.

BIOGRAPHY

Marta Saccher was born in Trieste, Italy in 1995. She received her BSc degree in Biomedical Engineering, in 2017, from Polytechnic University of Milan. She then moved to Delft to pursue her MSc studies in Biomedical Engineering at the Faculty of Mechanical, Maritime and Materials Engineering. She joined the ECTM group of TU Delft in 2018 and moved to Eindhoven to work on her thesis on MEMS ultrasound for implantable medical devices at Philips Research. In 2019, she obtained her MSc degree cum laude and later joined the department of Biomedical Instrumentation and Signal Processing at Aarhus University as a postgraduate student.

In 2020, she started her PhD at the ECTM group (Department of Microelectronics) of TU Delft in the framework of the European project Moore4Medical, which aimed to create open technology platforms for medical devices. She carried out her research at Philips in Eindhoven and, in the context of the project, she collaborated with multiple other European companies and academic groups such as Fraunhofer IZM, ANSEM, Osypka, Erasmus MC and Amsterdam UMC.

LIST OF PUBLICATIONS

JOURNAL PAPERS

1. **M. Saccher**, A. S. Savoia, R. Van Schaijk, J. H. Klootwijk, and R. Dekker. *Pre-Charged Collapse-Mode Capacitive Micromachined Ultrasonic Transducers (CMUT) for Efficient Power Transfer*. To be submitted to *IEEE Transactions of Ultrasonics, Ferroelectrics, and Frequency Control*

2. **M. Saccher**[*], S. Kawasaki[*], J. H. Klootwijk, R. Van Schaijk, and R. Dekker. "Modeling and Characterization of Pre-Charged Collapse-Mode CMUTs". In: *IEEE Open Journal of Ultrasonics, Ferroelectrics, and Frequency Control* 3 (2023), 14–28. *These authors should be ragarded as joint first author.

3. **M. Saccher**, S. Kawasaki, M. P. Onori, G. M. van Woerden, V. Giagka, and R. Dekker. "Focused ultrasound neuromodulation on a multiwell MEA". in: *Bioelectronic Medicine* 8.1 (2022), p. 2

CONFERENCE PROCEEDINGS PAPERS

1. **M. Saccher**, R. Van Schaijk, S. Kawasaki, J. H. Klootwijk, A. Rashidi, V. Giagka, A. S. Savoia, and R. Dekker. "A Comparative Study of Si_3N_4 and Al_2O_3 as Dielectric Materials for Pre-Charged Collapse-Mode CMUTs". In: *2023 IEEE International Ultrasonics Symposium (IUS)*. 2023, pp. 1–4

2. S. Kawasaki, **M. Saccher**, W.-J. de Wijs, J. van Den Brand, and R. Dekker. "Ultrasound Imaging with Pre-charged Collapse-Mode CMUTs". In: *2023 IEEE International Ultrasonics Symposium (IUS)*. 2023, pp. 1–4

3. A. Rashidi, **M. Saccher**, C. B. Karuthedath, A. T. Sebastian, A. S. Savoia, F. Lavigne, F. Stubbe, R. Dekker, and V. Giagka. "An Ultrasonically Powered System Using an AlN PMUT Receiver for Delivering Instantaneous mW-Range DC Power to Biomedical Implants". In: *2023 IEEE International Ultrasonics Symposium (IUS)*. 2023, pp. 1–4

4. **M. Saccher**, S. S. Lolla, S. Kawasaki, and R. Dekker. "Time-efficient low power time/phase-reversal beamforming for the tracking of ultrasound implantable devices". In: *2022 IEEE International Ultrasonics Symposium (IUS)*. IEEE

5. S. Kawasaki, J.-J. Yeh, **M. Saccher**, J. Li, and R. Dekker. "Bulk Acoustic Wave Based Microfluidic Particle Sorting with Capacitive Micromachined Ultrasonic Transducers". In: *2022 IEEE 35th International Conference on Micro Electro Mechanical Systems Conference (MEMS)*. IEEE

6. **M. Saccher**, S. Kawasaki, and R. Dekker. "The long-term reliability of pre-charged CMUTs for the powering of deep implanted devices". In: *2021 IEEE International Ultrasonics Symposium (IUS)*. IEEE

7. S. Kawasaki, E. Dijkema, **M. Saccher**, V. Giagka, J. J. H. B. Schleipen, and R. Dekker. "Schlieren visualization of focused ultrasound beam steering for spatially specific stimulation of the vagus nerve". In: *2021 10th International IEEE/EMBS Conference on Neural Engineering (NER)*. IEEE

8. S. Kawasaki, Y. Westhoek, I. Subramaniam, **M. Saccher**, and R. Dekker. "Pre-charged collapse-mode capacitive micromachined ultrasonic transducer (CMUT) for broadband ultrasound power transfer". In: *2021 IEEE Wireless Power Transfer Conference (WPTC)*. IEEE

9. S. Kawasaki, I. Subramaniam, **M. Saccher**, and R. Dekker. "A microwatt telemetry protocol for targeting deep implants". In: *2021 IEEE International Ultrasonics Symposium (IUS)*. IEEE

CONFERENCE PRESENTATIONS AND POSTERS

1. **M. Saccher**, A. Rashidi, A. S. Savoia, V. Giagka, and R. Dekker. "Phase Distribution Efficiency of cm-Scale Ultrasonically Powered Receivers". In: *2023 IEEE International Ultrasonics Symposium (IUS)*. 2023, pp. 1–4

2. A. S. Savoia, D. Giusti, C. Prelini, **M. Saccher**, A. Rashidi, A. Leotti, V. Giagka, and M. Ferrera. "Evaluating the Influence of PMUT Mechanical Support Properties on Power Conversion Efficiency in Ultrasonically Powered Implants". In: *2023 IEEE International Ultrasonics Symposium (IUS)*. 2023, pp. 1–4

3. **M. Saccher**, S. S. Lolla, S. Kawasaki, and R. Dekker. "Time-efficient low power time/phase-reversal beamforming for the tracking of ultrasound implantable devices". In: *ProRISC & SAFE conference, Enschede (NL)*. 2022